Escola de Camins
Escola Tècnica Superior d'Enginyeria de Camins, Canals i Ports
UPC BARCELONATECH

PROJECTE O TESINA D'ESPECIALITAT

Títol

CO_2 STORAGE: FLOW IN DAMAGED GEOLOGICAL FORMATIONS

Autor/a

Rubén Riverol Brignardelli

Tutor/a

Eduardo Alonso Pérez de Ágreda

Departament

Enginyeria del Terreny, Cartogràfica i Geofísica

Intensificació

Enginyeria del terreny

Data

Maig de 2014

Title: CO_2 storage: Flow in damaged geological formations
Author: Rubén Riverol Brignardelli
Advisors: Eduardo Alonso Pérez de Ágreda

Abstract

The storage of supercritical CO_2 in reservoirs capped by impervious rock formations (Carbon Capture and Storage, Carbon Sequestration or, simply, CCS) has recently been proposed as an approach to reducing atmospheric emissions of greenhouse gases. Nevertheless, these techniques could lead to the potential damage of the hosting rock as a result of gas overpressure. Thus, forecasting its behaviour is of utmost importance to avoid fluid migration, a situation that would reduce storage efficiency, pollute nearby aquifers and even trigger seismic events due to fault reactivation.

This thesis is aimed at studying several aspects concerning Carbon Sequestration, paying special attention to how the development of such injection projects could affect geological media. The first part of the thesis approaches the topic from a more theoretical perspective, intoducing the concept of CCS and reviewing the most relevant geotechnical theory that rule multiphase flow and fracture behaviour. The work is then focused on the importance of numerical modelling and, in particular, the use of the finite element code CODE_BRIGHT to simulate this type of problems. In a more practical approach, an interesting real case, the In Salah injection project, is selected as an example of how the existence of highly conductive, fractured features can alter the expected behaviour of geological media. In a simplified manner, and in an attemp to understand the particular aspects of this case, some 2-D simulations have been carried out.

Finally, a typical reservoir-caprock environment as found in CO_2 storage schemes is simulated using data provided by several papers (Rutqvist, 2008, 2010 & 2013). Simulations are carried out assuming three different scenarios for a similar geometry under damaged and undamaged conditions. It is concluded that the existence of fractures (although inititally closed) in the sealing caprock could trigger an uncontrollable migration of supercritical CO_2 to upper strata and could also lead to much bigger, and also uncontrolled, vertical displacements (uplifts). The particular case in which a vertical fault (modeled as a damaged area rather than a single discontinuity plane) exists is studied. In this case, the zone where the vertical feature intersects the reservoir is especially critical. It is there where the maximum decrease in effective net stresses is observed and, thus, it is a potential failure point that could also propagate fault inestability by allowing CO_2 to keep moving upwards if the increment of permeability is big enough. The formation of a clearly defined preferential path is observed, and CO_2 is allowed to keep spreading through the fault until it reaches a steady state far from the injection reservoir.

Keywords: Greenhouse effect, supercritical CO_2 , multiphase flow, discontinuities, numerical simulation, finite elements, embedded joint, fault zone.

Título: Almacenamiento de CO_2 : Flujo en formaciones geológicas dañadas
Autor: Rubén Riverol Brignardelli
Tutores: Eduardo Alonso Pérez de Ágreda

Resumen

El almacenamiento de CO_2 supercrítico en estratos limitados por formaciones rocosas impermeables (*Carbon Capture and Storage*, *Carbon Sequestration* o, simplemente CCS) ha sido propuesto como método para reducir la emisiones a la atmósfera de gases de efecto invernadero. Sin embargo, estas técnicas pueden conducir al daño potencial de la roca como resultado de las sobrepresiones de gas. Consecuentemente, prever su comportamiento es de gran importancia para evitar la migración de fluido, una situación que reduciría la eficiencia del almacenamiento, contaminaría los acuíferos cercanos e incluso podría desencadenar eventos sísmicos debido a la reactivación de fallas.

El objeto de esta tesina es estudiar varios aspectos relacionados con el CCS, centrándose en cómo el desarrollo de tales proyectos de inyección puede afectar al medio geológico. En la primera parte, el tema se desarrolla desde una perspectiva más teórica, introduciendo el concepto de CCS y revisando la teoría geotécnica más relevante en relación al flujo multifásico y al comportamiento de fracturas. El trabajo se centra luego en la importancia de la modelación numérica y, en particular, en el uso del código de elementos finitos CODE_BRIGHT para simular este tipo de problemas. En un acercamiento más práctico, un interesante caso real, el proyecto de inyección de In Salah, ha sido seleccionado como ejemplo de cómo la existencia de elementos fracturados puede alterar el comportamiento esperado de un medio geológico. De un modo simplificado, y con el objeto de entender las particularidades de este caso, se han realizado algunas simulaciones bidimensionales.

Finalmente, se simula un típico entorno *reservoir-caprock,* como el que puede encontrarse en esquemas de almacenamiento de CO_2, a partir de datos proporcionados por varios *papers* (Rutqvist, 2008, 2010 & 2013). Las simulaciones se llevan a cabo suponiendo tres escenarios diferentes con geometrías similares y bajo condiciones dañadas y no dañadas de la roca. Se concluye que la existencia de fracturas (aunque inicialmente cerradas) en la roca sello podría desencadenar una migración incontrolable de CO_2 supercrítico hacia estratos superiores y podría conducir, además, a movimiento verticales (levantamientos) mucho mayores e incontrolados. Se estudia el caso particular de la existencia de una falla vertical (modelada como una área dañada en lugar de un plano de discontinuidad). En este caso, la zona donde la falla intersecta al estrato de inyección es especialmente crítica. Es allí donde se observa el mayor decremento de tensiones efectivas netas y, por consiguiente, es un potencial punto de rotura que podría propagar la inestabilidad de la falla, permitiendo al CO_2 migrar si el incremento de permeabilidad es suficientemente grande. Se observa la formación de un camino preferencial claramente definido, y como el CO_2 continúa propagándose a través de la falla hasta alcanzar un estado estacionario ya lejos del estrato de inyección.

Palabras clave: Efecto invernadero, CO_2 supercrítico, flujo multifásico, discontinuidades, simulación numérica, elementos finitos, junta embebida, zona de falla.

TABLE OF CONTENTS

TABLE OF FIGURES AND TABLES

FIGURES

TABLES

INTRODUCTION

Reducing the emissions of CO_2 to the atmosphere is one of the major environmental concerns these days. Several techniques have been proposed, being the storage of supercritical carbon dioxide in deep geological formations (CCS) one of the most promising short-term options. Fluid is injected in porous strata capped by impervious layers which keep it safely stored within the reservoir limits.

Several types of geological formations have been identified as suitable for storing supercritical CO_2. Among them, depleted gas/oil fields and saline formations are the most common ones. The injected fluid then gets trapped due to different mechanisms which, in all cases, involve the presence of low-permeability rocks overlying the reservoir. This impervious sealing avoids the injected fluid (lighter than water) to move upwards by the effect of buoyancy and, thus, a supercritical CO_2 reservoir is created, similarly to how hydrocarbons have been accumulating for thousands of years.

Nevertheless, when exploitation of underground sources is involved, public concern always arises due to the potential risks that such activities entail. Sealing capacity of the caprocks, deformation , fracture reactivation and induced seismicity are some of the issues that could affect public perception and acceptance of projects which involve the injection of fluids in underground rock formations. But this concerns are not only a public acceptance issue, since it has been proven that overpressurized fluids could play an important role in reactivating faults or fractures. Furthermore, literature provides examples of situations in which the presence of fluids was related to notable (i.e. felt) seismic events. Generally, this could happen due to the existence of already damaged formations, which could turn initially impervious materials into highly-conductive ones because of pressure-induced joint opening.

Geomechanics is a key factor to explain the behaviour of the storage site. In recent years, the development of numerical methods has been essential to simulate underground injection processes and understand their effect on the surrounding rocks. In particular, the existence of initially closed fractures (or inactive faults) is especially interesting. Two apparently similar injection sites could act very differently depending on whether fracture opening and the formation of highly-conductive preferential paths takes place or not. In contrast with other processes which could be simulated with less uncertainty, simulating CO_2 storage projects is complex because lots of data are needed and information provided by a particular case might not be applicable to another one. Mechanical and hydraulic properties of materials, constitutive models accurate enough to describe its behaviour, existence of folds or other type of structures and presence of fractures and spacing between them are just model inputs which are relevant to carry out such simulations.

In spite of the numerous uncertainties, the simulation of typical storage environments provides useful information to understand the geomechanics associated to CCS. Indeed, numerical methods have become an essential tool in the forecasting of phenomena associated to underground injections and can help increase the level of safety in which such projects are performed.

Objectives

Carbon Capture and Storage involves a great variey of concepts, not only from a technical perspective but also from an environmental point of view. The present work is aimed at giving a global vision of CCS, which implies that providing clear but also exhaustive information is essential. To do so, this thesis has been structured so as to start from a conceptual approach to keep moving towards a much more technical one, with a whole section devoted to Carbon Storage project simulations using numerical methods. The main objectives are:

- Review of the most relevant papers concerning geological carbon storage.
- Review of the theory that rule fluid flow in geological media and fracture hydro-mechanical behaviour.
- Poblem resolution using numerical methods and, in particular, the use of the finite element program CODE_BRIGHT.
- Description of a real CCS project: review of previous studies and simulation of the 2-D deformational behaviour using CODE_BRIGHT.
- Use of CODE_BRIGHT to study how the injection of supercritical CO_2 may affect a typical reservoir-caprock environment under not damaged and damaged conditions. Presentation and discussion of results.

A correspondence between chapters of the thesis and objectives could be made, since each section is aimed at analysing the topic from a particular perspective. The ultimate scope of this work, this is the simulation of storage problems using data based on real observations provided by several authors, is presented in the last 3 chapters. First, a simplified model based on a real case is presented in order to compare the results with those provided by real observations and previous numerical results (Rutqvist et al., 2012). To end with, a more general case is simulated with the aim of studying the effects of fluid injection on damaged and undamaged formations. In particular, the work is focused on the potential for fault reactivation as well as the integrity of the sealing caprock and, thus, the potential leakage of CO_2 (and also displaced brine) to shallow groundwater aquifers.

CHAPTER 1

THE CONCEPT OF CARBON SEQUESTRATION

1.1. Global warming: An overview

1.1.1. Greenhouse effect

Among all the planets in the Solar System, the Earth is the only one that provides a surface temperature between the boiling and freezing point of water, thus making it suitable for most forms of life. This is partly due to the Earth's orbit radius, but also because of the properties of its atmosphere. Global average temperature is kept at this range because parts of the atmosphere (in fact, a collection of gases known as greenhouse gases) act like a glass cover, similar to those found in greenhouse structures, trapping enough solar energy to keep the planet warm.

The Sun energy is radiated into space in vast quantities and across a wide spectrum of wavelengths. Visible light makes up the 43% of the total energy emitted, but when it comes to wavelength it only represents a narrow band in the spectrum. After being absorbed by land, oceans and vegetation, the visible light is transformed into heat and re-radiated. The key factor in this process is the fact that not all of this energy is radiated back into space, but the Earth's atmosphere contains molecules that absorb the heat and re-radiate it in all directions, thus avoiding temperature to fall far below zero at night. Greenhouse gases molecules are, indeed, responsible for the fact that the Earth enjoys suitable conditions for the existence and development of its complex biosphere.

Carbon dioxide (CO_2), water vapour (HO_2), methane (CH_4), nitrous oxide (N_2O) and a few other gases make up the list of greenhouse gases due to the structure of their molecules. All of these are composed of more than two component atoms, bound loosely enough together to be able to vibrate with the absorption of heat. Other types of gases like oxygen (O_2) and nitrogen (N_2), the two major components of the atmosphere, do not have this particular structure but a two-atom molecule too tightly bound together to vibrate, hence they are not able to contribute to the greenhouse effect. [22]

Nevertheless, in the context of global warming, a distinction between natural and enhanced greenhouse effect must be made. [3] Human activities over the last decades have been altering the concentration of greenhouse gases in the atmosphere and more heat is being trapped by their molecules. As a consequence, Earth's surface temperature is increasing up to unusually high levels.

1.1.2. The role of CO_2

Carbon dioxide is the primary greenhouse gas emmited through human activities and is one of the major factors contributing to global warming. Data collected over the last decades show how important CO_2 presence is in comparison to other types of gases. For example, in 2011 Carbon Dioxide made up about 84% of the total amount of the greenhouse gases emissions in the US, according to the United States Environmental Agency (EPA). The natural presence of CO_2 in the Earth's atmosphere is part of a process known as the Carbon Cycle, which involves the natural circulation of carbon among the atmosphere, oceans, soil, plants, and animals. Human activity, though, is altering this cycle both by adding more CO_2 to the atmosphere and by influencing the ability of natural sinks, like forests, to remove CO_2 from the atmosphere. [7]

About two-third of the total amount of CO_2 emitted is generated by electricity production and by transportation, being (basically) building heating and industry the remaining activities contributing to the emissions. It is indeed the combustion of fossil fuel for energy purposes that constitutes the main source of carbon dioxide emissions since the Industrial Revolution began around 1750. And still the tendency of the last few years show a really strong dependence on fossil fuel, as over 85% of the energy demands is being satisfied by oil, coal and gas burning processes (Benson, 2005). For instance, according to EPA, in the United States CO_2 emissions increased by about 10% between 1990 and 2011, a trend followed by most of the Western countries and, more recently, China and India. In this context, the most pessimistic scenarios (which consider no action being taken to limit emissions) estimate that CO_2 emissions will be doubled by 2050.

Some solutions, either to reduce or offset CO_2 emissions from fossil fuels, have been proposed over the last years. Even though the most effective way to cut down these emissions is, logically, to reduce fossil fuel consumption, carbon capture and storage in deep geological formations is being considered as the most important short-term strategies to contribute to climate change mitigation.

1.2. Carbon sequestration: main ideas

1.2.1. What is it and why is it important?

Carbon sequestration, or rather, carbon capture and storage (CCS), can be defined as the long-term storage of CO_2 (as well as other forms of carbon) to mitigate or defer global warming and avoid dangerous climate change. It has been proposed as a way to slow the atmospheric and marine accumulation of greenhoouse gases, which are released by burning fossil fuels. [5]

The concept of carbon sequestration is related to a set of technologies that involve both capturing the gas and depositing it in a reservoir. Basically, it can be described as a three-step process: [20]

- Capture of CO_2 from the atmosphere or directly from flume gases, such as those emitted by power plants or industrial processes.
- Transport of the captured and compressed carbon dioxide, normally using pipelines.
- Storage, which consists of the underground injection and sequestration of the CO_2 into deep geological formations. These formations are commonly made up by porous rocks that hold the CO_2 , overlaid by non-porous layers of rocks (or caprocks) that trap the carbon dioxide and prevent migration to upper layers.

The importance of CCS lies in its potentiality to reduce greenhouse gases emissions from industrial processes while enabling low-carbon electricity generation from power plants. According to the *US Inventory of Greenhouse Gas Emissions and Sinks*, electric power plants that burn fossil fuels produce more than 40 % of the emitted CO_2 in the United States. However, CCS technologies can reduce by 80 or 90 % the emissions from this production processes. To put this into perspective, if we applied CCS techniques to, for instance, a 500 MW coal-fired power plant, the amount of greenhouse gases emissions avoided in one year would be (according to *EPA'S Carbon Equivalencies Calculator*) equivalent to planting more than 62 million trees and waiting for them to grow, or avoiding annual electricity-related emissions from more than 300 000 homes. [21]

1.2.2. Historical development

Even though the concept of carbon sequestration is rather new, gas injections into deep geological formations (especially for comercial purposes) have already been carried out succesfully in the last decades. Research on carbon sequestration dates back to 1975, but rapid development occurred only in recent years.

The first commercial project of H_2S and CO_2 injection into a saline aquifer was the Acid Gas Deep Injection project in Canada and dates from the early 1990's (Bachu and Gunter, 2004). Then, in 1996 the first commercial-scale project involving the injection of CO_2 gas only into a saline aquifer was carried out in Sleipner, on the Norway continental shelf (Torp and Gale, 2004). But it was not until 2004 that the first project involving the injection of CO_2 from natural gas production started in In Salah, Algeria (Riddiford et al. , 2003), followed by the Snøhvit project, offshore Norway, in 2008. These two projects, along with the Sleipner one, are the largest commercial injection operations today, having the highest injection rates and an estimated life-time injection of 10 years. Additionally, these three operations have given very valuable information, showing how different types of geological formations can act as reservoirs for carbon dioxide storage (Hermanrud et al., 2009 ; Eiken et al., 2011).

Other projects involving CO_2 sequestration have been planned in recent years, for instance the gas injection planned in the Gorgon Field in Australia (Flett et al., 2009). At the same time, pilot projects have been launched in different countries. The Frio & RCSP-phase II project in the USA, Ketzin in Germany, Lacq Rousse in France and Otway I & II in Australia, just to name some, are examples of these demonstration projects carried out in recent years (Michael et al., 2010). [13]

Carbon dioxide is also being injected in some places for other purposes, such as increasing and enhacing oil and gas recovery. This is the case of the Weyburn project, Canada, which is an enhanced oil recovery (EOR) project (Riding, 2006). Other examples are the enhanced gas recovery (EGR) projects in Otway, Australia, (Bouquet et al., 2009) and K12B in the Netherlands (Van der Meer et al., 2005). Figure 1 shows some of the most important projects developed so far.

These are just some examples to illustrate how the number carbon sequestration projects has been increasing since the first studies were carried out more than three decades ago. In the future, CCS will undoubtedly receive increasing attention by Governments in the process of combating climate change based on its expected technical development and cost reduction.

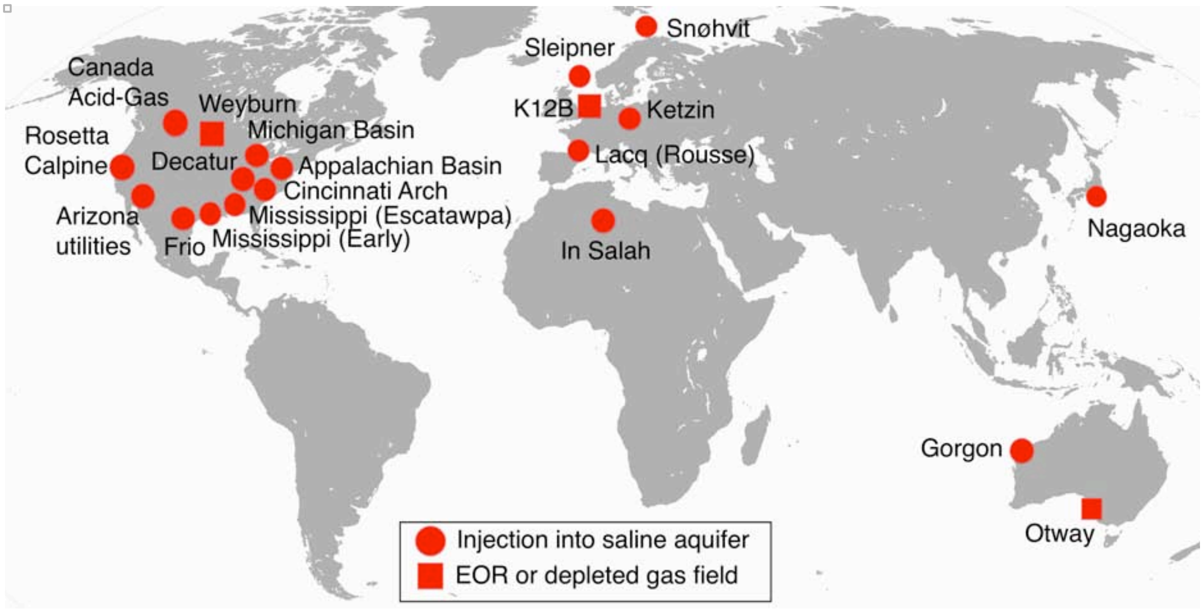

Figure 1 : World map showing active storage projects, both injecting the fluid into saline aquifers and depleted gas/oil fields, as reported by Michael et al. (2010)

1.3. Capture and storage

1.3.1. Sources, capture and transport

Carbon dioxide gas can be biologically fixed by growing vegetation (such as forest trees or biomass crops) and stored in above and below ground plant parts. In a strict sense, this is what we call carbon sequestration (CS) because it does not include any complex capture or storage technique. In other words, this approach focuses on enhancing natural processes to increase the removal of carbon from the atmosphere. Carbon dioxide gas is directly captured from the atmosphere in this case.

On the other hand, CO_2 can be captured directly from large stationary source points. This is the case of the already mentioned capture from petrolium refineries, power plants, gas processing units and other industrial activities. Therefore, carbon dioxide is concentrated into a nearly pure form and, after being captured, it is transported using pipelines and injected into geological storage sites, which can be located on- and off-shore. In any case, the gas is injected far below the ground surface (Bachu, 2000). All this should, in fact, be called carbon dioxide capture and sequestration or carbon capture and storage (CCS) rather than just carbon sequestration, but it is not rare to use both expressions as synonyms. From both approaches, it is the latter that we are focusing on.

There are three main technology types for CO_2 capture in the context of CCS: pre-combustion, post-combustion and oxy-firing. Pre-combustion capture involves partial combustion of carbon dioxide to produce hydrogen and CO_2. In post-combustion capture, on the other hand, CO_2 is removed after combustion of the fossil fuel, and so can be included in both new and existing power plants. Finally, oxy-firing consists on burning fuel in pure oxygen instead of air, which results in the generation of a gas (basically composed by water and CO_2) that is ready to be compressed and stored without further treatment. Over 90 % of the CO_2 produced by fossil fuel combustion can be prevented from reaching the atmosphere using these various techniques. Nevertheless, to guarantee a significant impact of CCS on global emissions, carbon dioxide gas has to be injected on a large scale, of the order of Gt per year. [14]

The captured gas can be transported by ship, truck or pipeline, but the latter seems to be the only practical solution when large amounts of CO_2 coming from power plant emissions are involved. As pipelines have been used since the 1970s in the context of fluid injection for enhanced oil recovery, this type of transportation is nowadays well understood and enjoys reputation for being safe and reliable.

1.3.2. Potential storage sites and storage capacity

When storing carbon dioxide in subsurface geological formations, an important criterion is that CO_2 has to be injected in supercritical state. Supercritical CO_2 has different properties, such as a higher density and a fluid-like behaviour. Notwithstanding, it is still lighter than water and therefore buoyancy makes it move upwards when injected in a saline aquifer. Actually, its behaviour can be compared to that of hydrocarbons in the sense that it has a tendecy to acummulate in some specific subsurface zones that act as traps. In other aspects (such as phase properties and solubility in water) supercritical CO_2 and hydrocarbons are quite different. Despite this fact, the wide experience in oil and gas projects can be applied to CO_2 storage by adjusting some factors. More information about carbon dioxide phases and properties is given in subsection 2.2.

Formations suitable for CO_2 storage are located in sedimentary basins where thick sediments have accumulated over millions of years (Benson, 2005). More specifically, carbon dioxide can be injected in deep saline aquifers overlaid by caprocks, oil and gas reservoirs and deep unmineable coal beds.

The case of carbon dioxide injected in oil reservoirs is quite interesting. On the one hand, CO_2 can be injected to enhance oil and gas recovery by maintaining reservoir pressure. The new fluid dissolves into the oil, reduces its density, and makes it more mobile. On the other hand, CO_2 can also be injected into a **depleted reservoir** just to be stored, replacing the oil and gas which have already been removed and avoiding abrupt pressure changes. According to some sources (Freund et al., 2003) depleted gas and oil reservoirs are able to store up to 800 Gt of carbon dioxide gas, as well as other buoyant fluids, which may remain trapped for millions of years.

Saline aquifers are another type of potential storage sites. These are deep underground formations containing brine and have a global storage capacity estimated to be between 400 and 10,000 Gt of CO_2 (Freund et al., 2003). Finally, **unmineable coal beds** can also be used as injection sites. These formations are too deep beneath the ground to be explored without making the whole process uneconomical. In this case, carbon dioxide is absorbed onto the coal, with a total estimated storage capacity of around 148 Gt of CO_2 (Freund et al., 2003).

Carbon dioxide can be stored in the same types of traps as hydrocarbon accumulations (Biddle and Wielchowsky, 1994). Basically, these traps can be structural or stratigraphical depending on how the fluid gets captured. These concepts are commonly used in petroleum geology.

A **structural trap** is formed as a result of changes in the structure of the subsurface due to tectonic, diapiric, gravitational and compactional processes. All these changes prevents the fluid from moving upwards, hence a reservoir is usually created. They are the most common type of traps and represent the majority of the discovered petroleum resources. The most important categories of structural traps include the following types (Biddle and Wielchowsky, 1994):

- Anticlinal trap or fold (figure 2.A), which is an area of the subsurface where the strata have been pushed into forming a domed shape. Buoyant fluids can accumulate in the crest of the anticline as long as the domed shape is caped by impervious rocks. It is by far the most common type of trap. [15]
- Fault (figure 2.B), formed by the movement of permeable and impermeable layers of rock along a line or, rather, a plane. The offset due to this movement has made the permeable reservoir be now adjacent to an impervious rock, thus preventing the fluid from further migration. [19]
- Piercement (figure 2.C), which is in fact an anticlinal fold in which a mobile core like salt or gypsum has pierced through the overlying rock.
- Combination of fault and fold (figure 2.D)
- Subunconformities (figure 2.E) and above unconformities (figure 2.H). The concept of unconformity is used to describe any breaks in the sedimentary geologic record. In other words, it is a buried erosional surface separating strata from different ages.

Stratigraphical traps, on the other hand, allow fluid accumulation due to the variation of rock properties rather than faulting, folding or other stress-related geological phenomena. Indeed, rock character can change even within the same layer and, in some cases, over short distances. [18] The two following types can be distinguished:

- Lateral depositional changes, either due to lateral variation of the lithological properties (figure 2.G.1) or because of reservoir termination when being pinched out against a non-porous sealing rock (figure 2.G.2).
- Buried depositional relief (figure 2.H), in which the trap is formed when a younger impervious section buries the older one. As a result, the required top seal that avoids fluid migration is created (Biddle and Wielchowsky, 1994).

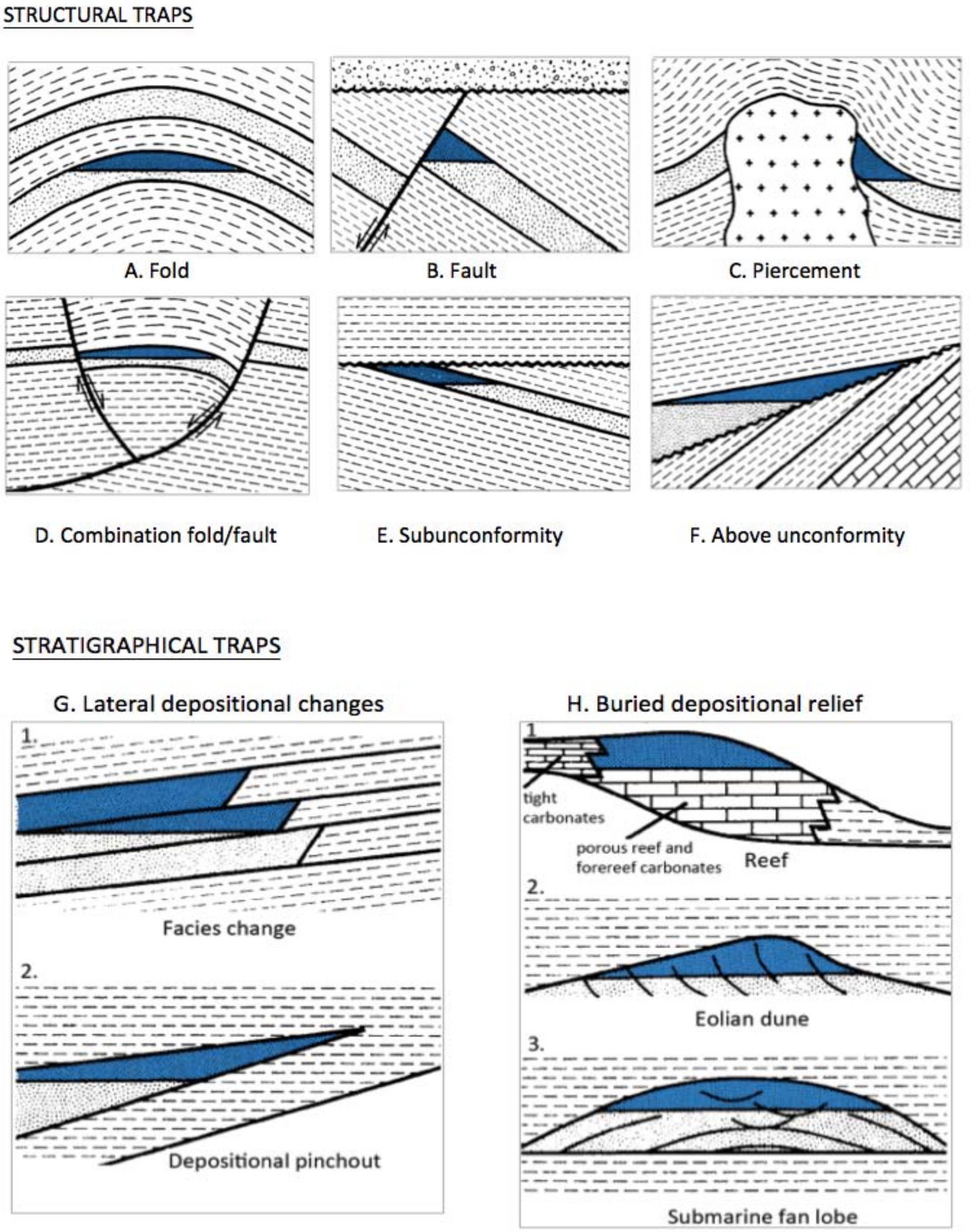

Figure 2 : Major categories of structural and stratigraphical traps (Biddle and Wielchowsky 1994).

Finally, CO_2 can be stored in a reservoir without a closed structure avoiding fluid migration. This happens when the volume injected is small in comparison to the storage area. In this case, CO_2 starts migrating laterally beneath the caprock, but it never reaches its edge limit, so the fluid is in fact sequestrated without being trapped like in the aforementioned cases. The typical CO_2 plume shape is showed in figure 3.

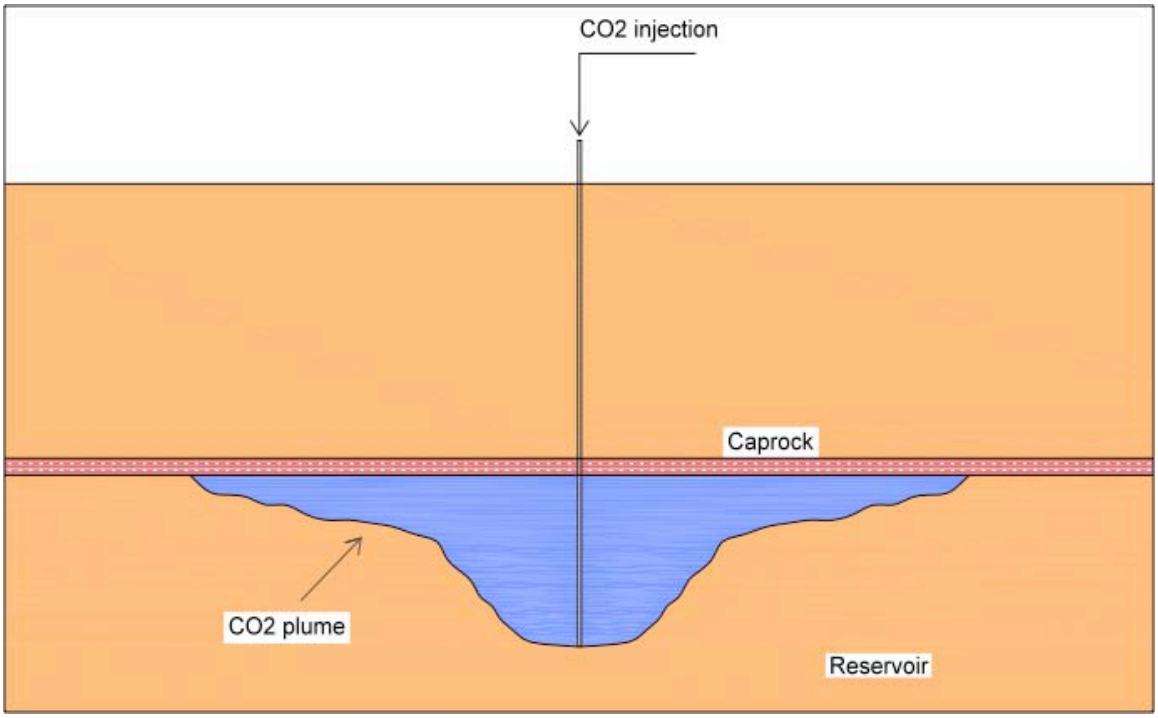

Figure 3 : Scheme depicting how CO_2 gets trapped in a large storage area and the typical plume shape.

1.3.3. Injection and trapping mechanisms

As it has been mentioned, carbon sequestration in deep geological formations involves many techniques that have already been used for years by the oil and gas industry. This is extremely positive in the sense that it provides broad experience in the field of drilling and injecting buoyant fluids underground. Over the years, the industry has been forced to develope more precise drilling practices as oil and gas have become less accessible, and all this improved technology is being deployed in carbon sequestration projects so as to ensure that CO_2 injection and storage is carried out safely.

Once the supercritical CO_2 has been injected, a variety of mechanisms are responsible for keeping it securely stored. Basically, four types of mechanisms are considered: the aforementioned structural and stratigraphic trapping, residual trapping, solubility trapping and mineral trapping. [17]

Structural and stratigraphical trapping is the most dominant of all. The injected fluid, which is more buoyant than water, percolates up through the porous rocks until it meets an impermeable layer. It then gets trapped due to the reservoir geometry or because its extension, as it has already been explained in 1.3.2. Figure 4.A shows how this mechanism works.

Residual trapping, on the other hand, happens because of the reservoir rock porosity, which makes it act like a rigid sponge, thus keeping part of the CO_2 immobile inside the voids. As the supercritical gas is injected, water (or brine) is displaced and the new fluid gradually fills the pores and keeps moving until water again replaces it. Nevertheless, not all the CO_2 is removed from voids: some residual and disconnected droplets are left behind and fill part of the pore space, just like water in a sponge. This mechanism is responsible for the fact that oil has been held in some reservoir for millions of years. Figure 4.B schematically depicts this mechanism.

The third type of mechanism is **solubility trapping**. Carbon dioxide, both in its gaseous and supercritical state, dissolves in other fluids, such as water or brine already present in the porous rock. This phenomena induces carbon dioxide to be trapped in the reservoir, as depicted in figure 4.C. The amount of dissolved CO_2 will depend on the CO_2 phase pressure, contact area between carbon dioxide fluid and water, the time of exposure and also the possible reactions between water and reservoir minerals.

Finally, **mineral trapping** could take place (figure 4.D). Being the process following CO_2 dissolution, this mechanism is in fact intimitely connected to the previous one. Once carbon dioxide dissolves in water, it forms a weak carbonic acid which, over a long time, may react with the minerals in the reservoir and hence solid carbonate minerals can be formed. As a result, this mechanism binds CO_2 to the rock as it gets trapped in this authigenic minerals. All this is similar to some other natural processes which have lead to the formation of large geological structures, such as the White Cliffs of Dover. Normally, carbon dioxide becomes more securely trapped with time, but the mentioned binding process can be slower or more rapid depending on the chemistry of rock and water.

While structural, stratigraphic and residual mechanism might be the most relevant during the initial storage period, after some time, solubility and mineral trapping start to gain more importance to the point that they become really dominant in long-term storage sites. Mineral trapping is considered the safest of all four mechanisms.

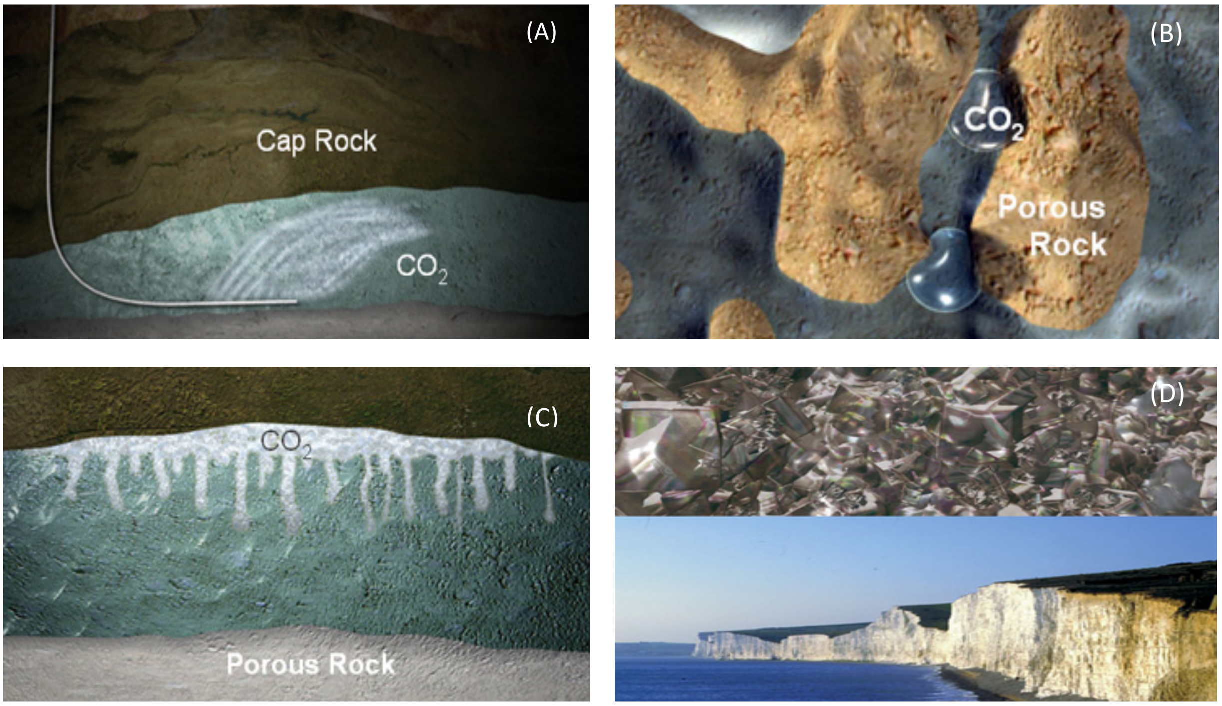

Figure 4 : A. Structural/stratigraphic trapping ; B. Residual trapping ; C. Solubility trapping ; D. Mineral trapping [17]

1.4. Potential risks and failures

Geological formations selected for carbon dioxide injection in the context of CCS techniques are located at a minimum depth of 800 m. Thus, since CO_2 gas is stored at supercritical state, it is possible to trap large amounts of fluid in a relatively small volume. Injections implemented on large scale, though, may cause big impact if the potential risks are not assessed properly. It is absolutely essential to provide evidence to inform goverments and the public that potential risks are well understood, as well as studying impact assessments for long-term safety and control measure (Wei et al., 2011).

1.4.1. Geotechnical risks

Apart from CO_2 surface leakage caused by pipeline failure, the most noticeable risks of these storage techniques are associated to the injection process. Indeed, Carbon Capture and Storage induces changes in the geological formation that may have non-negligible consequences. This is of major importance in damaged formations, for instance fault zones, in which the interaction between mechanical behaviour and fluid flow could trigger **fault reactivation** and inestability, **induced seismicity**, and associated **fluid migration**.

In the Earth's upper crust, fault reactivation may occur due to different factors, but it is known that mechanical and hydraulic interactions play a really important (and critical) role in this process (Scholz, 1990). On the one hand, tectonic processes may trigger fault reactivation and slip as they are associated to stretching, thinning, shortening, thicking and relative lateral movement of parts of the crust or lithosphere. On the other hand, slip may be induced by changes in the hydraulic pressuritation which is, indeed, a direct consequence of injecting a fluid in an already saturated (or non-saturated) geological media. Whilst shear stress accumulations may induce rupture, fluid pressure build-up is also a key factor in the process as it is capable of reducing fault strength. For more details, see Chapter 2: Scientific background.

Fault reactivation (and slip) induced by stress and fluid pressure conditions at various depths in the upper portion of the crust can, in some cases, trigger seismic activity. Indeed, these hydro-mechanical conditions may control the nucleation, propagation, arrest, and recurrence of moderate to large earthquakes (Wibberley and Shimamoto, 2005). Evidence of a pressurized CO_2 source being the main cause of earthquakes has been found in some seismic episodes such as the 1965-1967 Matsushiro earthquake swarm in Central Japan (Cappa et al., 2009) or the 1997 Umbria-Marche series of seismic events in nothern Italy (Miller et al., 2004). [4]

All these phenomena and subsequent effects make us wonder how sealed the reservoir really is once the CO_2 has been injected. Even without considering the hydromechanical effects, the fact that geological systems are heterogeneous and discontinuous media may trigger fluid migration through already existing fractures and fault zones. Once the pressure build-up effect due to fluid injection is taken into account, fracture opening and potential fault reactivation make the caprock impermeability an even more dubious assumption. Preferential paths for CO_2 migration might be opened, allowing the fluid to reach other strata or even be released to the ocean or the atmosphere depending on where the supercritical gas is stored. As well as affecting storage eficicency, fluid migration may threaten the environment and human health if the supercritical gas reaches an aquifer or any other source of potable water.

CHAPTER 2

SCIENTIFIC BACKGROUND

2.1. Introduction

Describing the mechanisms that govern fluid migration is one of the most important tasks when studying CO_2 injection. In this context, various mechanisms, some of them more dominant than others depending on the case, have been indentified: difussion, two-phase flow and two-phase flow coupled with mechanichal effects. [8] In the latter, which is the most interesting from the CCS point of view, the dominant mechanism is in fact fluid migration through high permeability fractures due to advection. Thus, fracture opening and its effect on permeability change is a really important aspect of the process.

In the first section of Chapter two, some interesting properties of carbon dioxide are going to be shown and discussed. Then, equations governing fluid flow in porous media will be presented and briefly discussed. Finally, since CO_2 injection involves hydro-mechanical coupling, in which the presence of discontinuities may play a key role in explaining hydraulic behaviour, some basic ideas concerning fractures should be introduced.

2.2. CO_2: phases and properties

2.2.1. Supercritical fluids

Carbon dioxide has three clearly defined physical states which depend on temperature and pressure: solid, gas and liquid. Additionally, a fourth state in which the fluid behaves like a substance between a gas and a liquid exists. Figure 5 shows the so-called phase diagram for CO_2 , in which the variety of states of the fluid for different pressures and temperatures is shown.

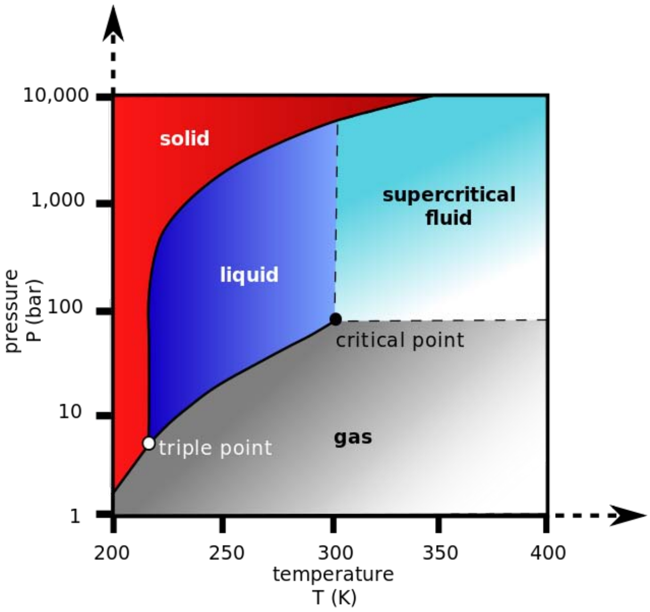

Figures 5 : Carbon dioxide pressure-temperature phase diagram. Note: 1 bar = 0.1 MPa ; 1 K = -272.15 ºC

Carbon dioxide can only appear in its gaseous and solid state below the triple point (which corresponds to 0.52 MPa and -56.6 ºC). At atmospheric pressure and within the range of temperatures historically registered on the Earth's surface, gas is the only possible state in which carbon dioxide can appear. At a temperature of 31 ºC and a pressure of 7.4 MPa (approximately) lies the critical point of carbon dioxide, above which CO_2 starts to behave like a supercritical fluid and distinct liquid and gas phases do not exist. This substance is miscible with other supercritical fluids, is able to effuse through solids (i.e. escape through small holes) like a gas and also dissolve materials like a liquid, hence it has properties between those of a gas and a liquid. Table 1 shows some approximated values of density, viscosity and diffusivity for typical gases, liquids and supercritical fluids. Properties of supercritical fluids can be closer to those of a liquid or to those of a gas by changing the pressure and temperature conditions. [27]

	Density $(\mathrm{kg/m^3})$	Viscosity $(\mathrm{\mu Pa \cdot s})$	Diffusivity $(\mathrm{mm^2/s})$
Gases	1	10	1 - 10
Supercritical fluids	100 - 1000	50 - 100	0.01 - 0.1
Liquids	1000	500 - 1000	0.001

Table 1: Some values of density, viscosity and diffusivity for typical fluids in different state (gas, liquid and supercritical) [16]

2.2.2. CO_2 density and viscosity

CCS projects often imply injection of carbon dioxide in supercritical state so as to obtain a relatively high density that minimizes the volume occupied by the greenhouse gas. In this context, knowing how density and viscosity evolve in such conditions is of major interest, since they mostly control fluid migration and the evolution of the CO_2 plume. Both properties depend essentially on temperature and pressure, the latter being especially relevant because of its variability when the fluid injection is performed. Because of its high compressibility, carbon dioxide density is highly dependent on temperature and pressure (Vilarrasa *et al.*, 2010). At supercritical conditions, density can adopt a wide range of values (450-800 $\mathrm{kg/m^3}$), which means that, in any case, supercritical CO_2 is lighter than water or brine. Consequently, flow is affected by buoyancy.

In the following two subsections, expressions describing the evolution of both density and viscosity with the aforementioned variables are going to be shown. Among other possible expressions, these two functions have been chosen on purpose, since they are the ones which have been implemented in recent versions of the software CODE_BRIGHT (see Chapter 3) to simulate CO_2 injection.

2.2.2.1. Redlich-Kwong equation for CO_2 density

One equation of state describing how CO_2 density evolves with pressure and temperature is the Redlich-Kwong equation (valid regardless of the temperature and pressure conditions) with the parameters proposed by Spycher *et al.* (2003): [23]

$$\rho_{CO_2} = \frac{M_{CO_2}}{\nu} \qquad (1.a)$$

where ν depends on temperature, pressure and other properties of the fluid as well as model parameters. It can be obtained by solving the following equation:

$$\nu^3 - \left(\frac{RT}{P}\right)\nu^2 - \left(\frac{RTb}{P} - \frac{a}{P\sqrt{T}} + b^2\right)\nu - \left(\frac{ab}{P\sqrt{T}}\right) = 0 \qquad (1.b)$$

where *a* and *b* are paramaters associated to the model and $R = 8.314\ J/mol\ K$

2.2.2.2. Altunin & Sakhabetdinov function for CO_2 viscosity

This function (Altunin & Sakhabetdinov, 1972) is also valid regardless of the temperature and pressure conditions, and can be written as follows: [23]

$$\mu_g = \mu_0 \exp\left(\sum_{i=1}^{4} \sum_{j=0}^{1} \frac{a_{ij}\ \rho_R^{i}}{T_R^{j}} \right)\ ;\ \mu_0 = T_R^{0.5}\left(27.2246461 - \frac{16.6346068}{T_R} + \frac{4.66920556}{T_R^{2}} \right) \qquad (2)$$

where a_{ij} ; $i = 1:4$, $j = 0,1$ are model parameters and:

$$T_R = \frac{T}{T_c}\ ,\ T_c = 304\mathrm{K} \quad ; \quad \rho_R = \frac{\rho_{CO_2}}{\rho_c}\ ,\ \rho_c = 468\ \mathrm{kg/m^3}$$

Figures 6.a and 6.b show the shape of these two functions in a pressure-density (or viscosity) plane for different temperatures.

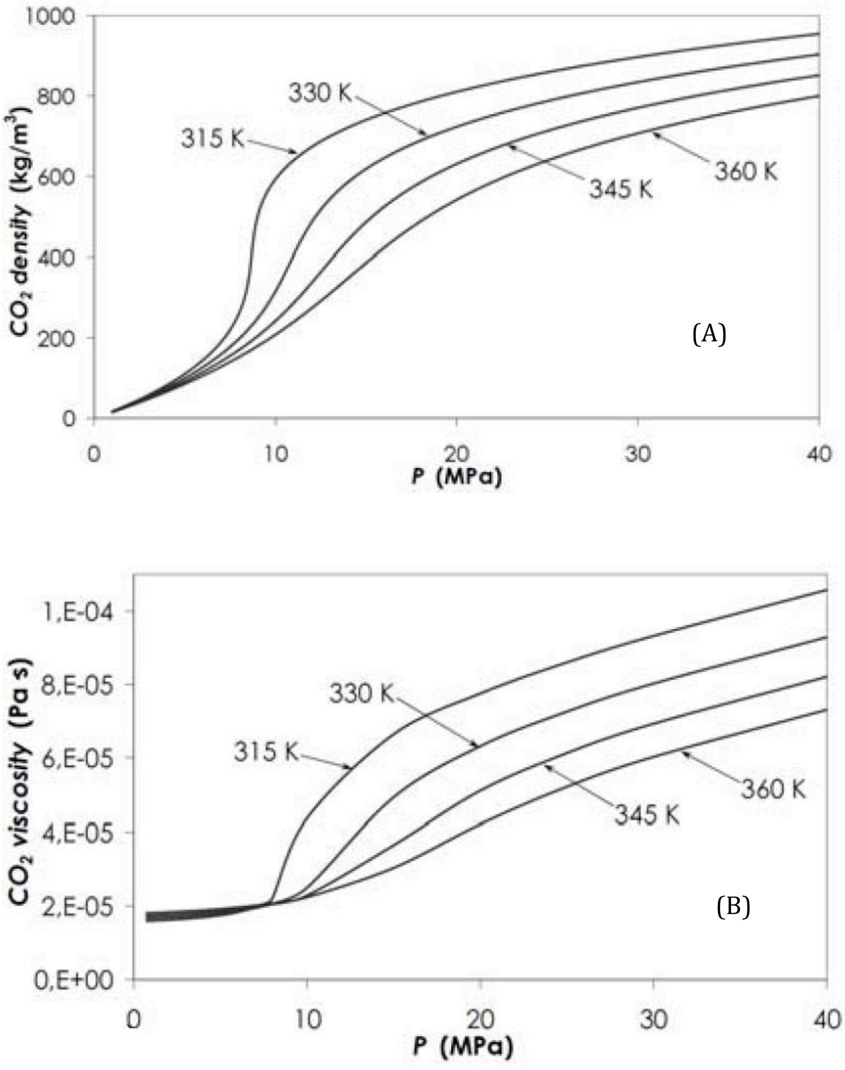

Figure 6: Functions describing the evolution of some CO_2 properties with pressure and temperature [26]
(A) Evolution of density with pressure build-up for different values of temperature
(B) Evolution of viscosity with pressure build-up for different values of temperature

2.3. Introduction to multiphase flow in porous media

2.3.1. Basic equations

The objective of this first section is to give some general ideas concerning multiphase flow in geological media. This basic infomation is presented now due to its importance and because it is necessary to understand the following chapters. For a more detailed description of mechanisms and equations that rule multiphase flow in geological media, see chapter 3 and Appendix B.

2.3.1.1. Darcy's law

When considering injection in a deep confined saline aquifer (a very common type of reservoir in CCS projects), two phases have to be taken into account: CO_2 and brine (solution of salt in water). In this context, Darcy's law expresses the momentum conservation of each phase (α) as follows:

$$\mathbf{q}_\alpha = -\frac{\mathbf{k}\,\mathrm{k}_{r\alpha}}{\mu_\alpha}\left(\nabla \mathrm{P}_\alpha + \rho_\alpha\, \mathrm{g}\, \nabla \mathrm{z}\right) \tag{3}$$

where $\boldsymbol{q}_\alpha$ is a vector quantity representing volumetric flux of each phase (expressed in units of velocity $L\,T^{-1}$), $\boldsymbol{k}$ is the intrinsic permeability tensor (expressed in units of L^2), $k_{r\alpha}$ is the relative permeability associated to the α-phase (a dimensionless value that accounts for the influence of saturation on fluid mobility), μ_α is its viscosity, P_α its pressure, ρ_α its density, g is gravity and z is the vertical coordinate. [25] See 2.3.2 for more information concerning permeability.

2.3.1.2. Continuity equation

Mass conservation of the two considered fluids (CO_2 and brine) can be expressed as (Bear 1972):

$$\frac{\partial(\rho_\alpha \mathrm{S}_\alpha \phi)}{\partial \mathrm{t}} = -\nabla \cdot (\rho_\alpha \mathbf{q}_\alpha) \tag{4}$$

where S_α is the degree of saturation of the α-phase, ϕ the porosity of the porous medium and t is time. Note that the the term on the left-hand side of equation (4) represents the time variation of the mass of the α-phase per unit of volume of porous medium. [25]

It is important to note that equation (4) is a rather simplified version of the more general mass conservation equations that will be presented later. On the one hand, this expression establishes balance in terms of phases and not components, which means that it does not account for the different species that can be present in each phase. For instance, using (4) we would consider water as liquid or CO_2 as gas, but we would be ignoring the fact that water can be present in the gas phase as vapour and that CO_2 can appear within the liquid phase as dissolved gas. On the other hand, by using this simplified equation we would be considering the advective Darcy flux only, and would be ignoring all the other mechanisms that take part in the process. Again, the more complete version of balance equations can be found in Appendix B.

2.3.2. Permeability

2.3.2.1. Intrinsic permeability and conductivity

Intrinsic permeability is a property of the medium regardless of the type of fluid. It means that this value represents the ability of the medium to allow fluid mobility, but it does not take into account how fluids with various properties behave differently when moving through media with the same characteristics.

This is why in equation (3) intrinsic permeability is affected by phase viscosity and density, so as to account for their influence on fluid mobility. In this line, it is common to introduce the concept of conductivity $\boldsymbol{K}$:

$$\mathbf{K}_\alpha = \frac{\rho_\alpha\, g}{\mu_\alpha}\mathbf{k} \tag{5}$$

Note the diferent type of letter used to distinguish intrinsic permeability from conductivity. The latter has the same structure as the former (a tensor of second order which can be represented by a 2 x 2 or 3 x 3 matrix) but it has dimensions of velocity ($L\,T^{-1}$), unlike intrinsic permeability (L^2).

Intrinsic permeability accounts for the porous matrix intrinsic permeability as well as the effect of fracture geometry, so it is not a constant value as fractures can be created, opened or closed due to mechanical effects. If we consider that the intrinsic permeability of the matrix doesn't change, which is true for quite rigid materials in which porosity is almost a constant value, then $\boldsymbol{k}$ is basically a function of joint aperture and the number of fractures. See section 3.1.2 for more details. Additionally, the fact that $\boldsymbol{k}$ is a tensor of second order and not a scalar must not be forgotten. Indeed, the tensorial structure allows it to include the properties in different directions:

- General intrinsic permeability matrix: $$[\mathbf{k}]_{xyz} = \begin{bmatrix} k_{xx} & k_{xy} & k_{xz} \\ k_{yx} & k_{yy} & k_{yz} \\ k_{zx} & k_{zy} & k_{zz} \end{bmatrix} \tag{6.a}$$

- Permeability in principal directions (1,2,3): $$[\mathbf{k}]_{123} = \begin{bmatrix} k_1 & 0 & 0 \\ 0 & k_2 & 0 \\ 0 & 0 & k_3 \end{bmatrix} \tag{6.b}$$

2.3.2.2. Relative permeability

The partial saturation of soil for each phase is introduced through the coefficient $k_{r\alpha}$ which, in the case of CO_2 flow, varies between 0 (when the degree of saturation S_r is 1) and 1 (when the degree of saturation S_r is 0). Indeed, these values account for the fact that regardless of the intrinsic permeability of the medium, injected CO_2 will not be allowed to move unless the medium starts to desaturate. Once the soil is completely desaturated ($S_r = 0$), CO_2 becomes perfectly mobile, so $k_{rg} = 1$ (i.e. no permeability reduction is considered). Between these values, relative permeability is a function of saturation. Values of $k_{r\alpha}(S_\alpha)$ have been reported by some authors. Even though multiple options exist, adopting a power law to consider the effect of desaturation on permeability is quite common:

$$k_{rl} = A_l S_l^{n_l} \quad ; \quad k_{rg} = A_g S_g^{n_g} \quad ; \quad S_g = 1 - S_l \tag{7}$$

where k_{rl} is liquid (brine) relative permeability, k_{rg} is gas (CO_2) relative permeability, S_l is the (liquid) degree of saturation and A_l , A_g , n_l , n_g are model parameters.

2.4. Discontinuities

2.4.1. Generalitites

Geological formations are heterogeneous and discontinuous media in which the presence of joints is of major importance. The collective term "joint" or "discontinuity" usually refers to any kind of weakness plane or cut that has very low (or nule) tensile strength. Some examples of this are fractures of all types, faults, fissures, bedding planes, zones of contact between different formations and zones where shear stresses are concentrated. Discontinuities usually have flat and parallel surfaces (which represent what is called a discontinuity set or family) and are separated by distances than vary from few centimetres to a few tens of metres. Joints are characterized by different properties such as orientation, separation, aperture, continuity (or persistance) and surface conditions.

In the next three subsections, some information regarding mechanical and hydraulic behaviour of joints is going to be given. Both hydraulic and mechanical effects have to be taken into account because fluid migration in CCS projects depends critically on fracture opening, a phenomenon basically dependent on mechanical interactions. Remember that the intrinsic permeability of a geological medium depends on the porous matrix intrinsic permeability but is also affected by the presence of joints. What's more, in many situations it is the presence of discontinuities that is decisive, because fractures are comparatively much more pervious than matrices. Fracture aperture controls its permeability and consequently has an important effect on the intrinsic permeability of the medium, allowing the fluid to migrate more easily through newly created preferential paths. Fracture interconnection and scale effect are also important aspects when evaluating the global intrinsic permeability, since a single isolated joint does not allow fluid to move freely through the medium.

2.4.2. Discontinuities: mechanical behaviour

2.4.2.1. Stress-strain variables

In continuum mechanics, stresses and strains are normally expressed using the stress and strain tensors. These tensors of second order, written as 3 x 3 matrices, represent the stress or strain state of the medium at any point. In the *xyz*, base (i.e. in the cartesian coordinate system), they can be written as follows:

$$[\boldsymbol{\sigma}]_{xyz} = \begin{bmatrix} \sigma_{xx} & \tau_{xy} & \tau_{xz} \\ \tau_{yx} & \sigma_{yy} & \tau_{yz} \\ \tau_{zx} & \tau_{zy} & \sigma_{zz} \end{bmatrix} \quad ; \quad [\boldsymbol{\varepsilon}]_{xyz} = \begin{bmatrix} \varepsilon_{x} & \varepsilon_{xy} & \varepsilon_{xz} \\ \varepsilon_{yx} & \varepsilon_{yy} & \varepsilon_{yz} \\ \varepsilon_{zx} & \varepsilon_{zy} & \varepsilon_{zz} \end{bmatrix} \qquad (8.\mathrm{a})$$

where σ_i and $\tau_{ij} = \tau_{ji}$, $i, j = x, y, z$ are, respectively, the normal stress in the *i* direction and the shear stress acting on the *ij* plane (see figure 7). In the same line, the components of the strain tensor can be defined. Expression (8.a) can be diagonalized when the tensor is expressed in the base of the principal directions *1,2,3*:

$$[\boldsymbol{\sigma}]_{123} = \begin{bmatrix} \sigma_1 & 0 & 0 \\ 0 & \sigma_2 & 0 \\ 0 & 0 & \sigma_3 \end{bmatrix} \quad ; \quad [\boldsymbol{\varepsilon}]_{123} = \begin{bmatrix} \varepsilon_1 & 0 & 0 \\ 0 & \varepsilon_2 & 0 \\ 0 & 0 & \varepsilon_3 \end{bmatrix} \qquad (8.\mathrm{b})$$

where σ_i , $i = 1,2,3$ are, respectively, the principal (normal) stresses in the *1, 2* and *3* principal directions. The same can be said of the strain tensor.

All these variables are commonly used in geotechnics, especially when describing stress-strain laws in soils and rock matrices. For discontinuities, though, other variables are considered. The most important idea is that stresses and strains are not referred to a point of the medium anymore, but to the discontinuity or joint plane. Thus, these variables are not tensors of second order but vectors (called traction vectors), which end up being scalar values once the decomposition of the vector into components parallel and perpendicular to the joint is carried out.

In a three-dimensional space, a discontinuity can be represented by a plane. Then, the traction vector acting on this plane can be decomposed into a normal stress perpendicular to this plane and two shear stresses included in the plane. To simplify this, a two-dimensional space (in which a dicontinuity is represented by a line) can be considered. Thus, the traction vector decomposition leads to two scalar values: the normal component, perpendicular to the line and usually written as σ, and the shear stress, in the same direction of the line and commonly written as τ (see figure 7). The same can be said of deformation, now written as displacements v and u (units of L) instead of strains (dimensionless). A relationship between the stress tensor and the traction vector acting on a discontinuity plane can be obtained from the following expression:

$$\mathbf{t} = \boldsymbol{\sigma} \cdot \mathbf{n} \tag{9}$$

where ***t*** is the traction vector and ***n*** is the unitary normal vector, this is, perpendicular to the joint surface and of length one.

Finally, if a discontinuity making an angle θ with the horizontal direction is considered, the normal and shear stresses acting on the joint can be written as a function of the components of the stress tensor in the cartesian coordinate system as follows:

$$\begin{gathered}\sigma = \frac{1}{2}\left(\sigma_x + \sigma_y\right) + \frac{1}{2}\left(\sigma_x - \sigma_y\right)\cos(2\theta) - \tau_{xy}\ \sin(2\theta) \\ \tau = \frac{1}{2}\left(\sigma_x - \sigma_y\right)\sin(2\theta) + \tau_{xy}\ \sin(2\theta)\end{gathered} \tag{10}$$

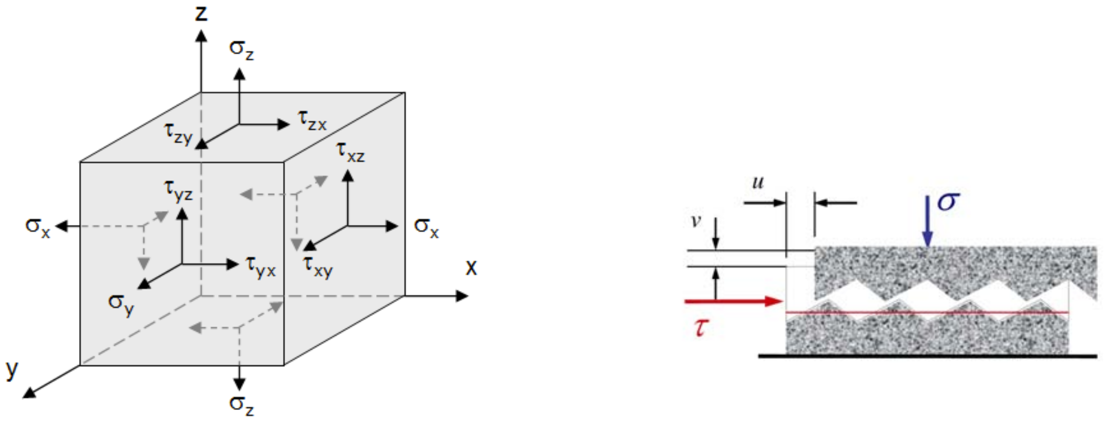

Figure 7: Series of stresses acting on the three coordinate planes (left) ; stresses / displacements acting on a single joint / discontinuity plane (right).

The relationship between stresses and displacements depends on the type of constitutive model chosen to define the behaviour of the joint. This is In the simplest case, if an elastic constitutive model is considered, the following equation relates stresses (σ and τ) to displacements (v and u):

$$\begin{Bmatrix} \mathrm{v} \\ \mathrm{u} \end{Bmatrix} = \begin{bmatrix} 1/\mathrm{K_n} & 0 \\ 0 & 1/\mathrm{K_s} \end{bmatrix} \begin{Bmatrix} \sigma \\ \tau \end{Bmatrix} \qquad (11.\mathrm{a})$$

where $\mathrm{K_n}$, $\mathrm{K_s}$ are the normal and shear stiffness, respectively. The former depends on the aperture of the joint, as indicated in the following expression:

$$\mathrm{K_n} = \frac{\mathrm{m}}{\mathrm{v_{mc}} - \Delta v} \qquad (11.\mathrm{b})$$

where *m* is a model parameter, Δv is the closure of the element and v_{mc} is the maximum closure or minimum aperture. Note how, as the discontinuity closure increases, the material becomes stiffer in the joint normal direction. See the following section for more information about joint closure.

2.4.2.2. Behaviour of joints under compression

Although compression stresses alone are able to generate displacements, the presence of discontinuities have an important influence on them due to aperture changes. Laboratory tests show that the presence of a joint accentuates the initial displacement in the normal direction because of the closure effect. Once the discontinuity aperture is small enough, displacement evolves at a lower rate, until it becomes almost nule.

The relationship between normal stress and joint closure can be described by some relatively simple mathematical models, like the following one:

$$\sigma = c\left[\frac{\Delta v}{v_{mc} - \Delta v}\right]^{t} \qquad t < 1 \qquad (12)$$

where *c* and *t* are model parameters. Note how, for *t=1*, expression 11 is obtained again.

2.4.2.3. Behaviour of joints under shear stress

Shear stresses acting on planes of discontinuity generate not only displacement along the direction of the joint (*u* in figure 7) but also perpendicular displacement (*v*) due to the effect of dilatancy. Numerous test data show, indeed, how parallel displacement evolves with shear stress and, simultaneously, the increment of perpendicular displacement during this process.

The existence of a peak and a residual strength is also quite noticeable and is associated to the evolution of the joint plane as shear stress increases. In a first stage, shear stress keeps increasing until it reaches the maximum value that can be resisted by the discontinuity in its initial state (i.e the peak shear strength τ_p), which has an associated shear displacement value u_p (or peak shear displacement). However, once shear stresses reach high values, alteration of resistant properties occurs, thus triggering a decrease in the joint shear strength until it reaches a constant value (i.e the residual shear strength τ_r). The evolution of shear strength is of the utmost importance in joints, especially when working with damaged geological media, in which fault reactivation may be triggered if failure conditions are met.

2.4.2.4. Shear stength

Shear strength of joints depends on various factors, which control the resistant properties of the discontinuity plane as well as its behaviour and the presence of more or less pronounced peak and residual values. In the following lines, some of the most important aspects are presented:

- Normal stresses. The existence of a normal stress lead to an increase in shear strength of discontinuities by making it more difficult for both faces to slip. This effect can be described by numerous mathematical models describing linear and non-linear $\sigma - \tau$ relationships which will be briefly discussed in Appendix A. In the $\sigma - \tau$ coordinate plane, two functions relating both stresses are usually defined, one for peak strength and another for residual strength, the latter showing a decrease in the aforementioned strength.

- Roughness. When subjected to shear stresses, a joint behaves differently depending on wether its faces are plane or rough. First, while in a plane smooth discontinuity shear stresses only induce displacements in the direction on the joint, in rough discontinuities normal displacements also exist. Additionally, the existence of rough planes translates into a higher initial friction angle. This means that, initially, the joint behaves as if its "effective" friction angle was higher than the actual friction angle of the constitutive minerals. For higher stress values and joint alteration, friction decreases and the mineral friction angle is again applicable.

- Imbrication. The higher roughness and imbrication in the joint, the more noticeable the aforementioned "peak effect" is. This means that in a joint with very rough surfaces and imbricate faces the decrease in shear strength once the discontinuity starts to be degraded is much more pronounced than in an already altered joint, in which the "peak effect" is almost negligible (i.e peak shear strength is the same as residual shear strength).

- Filling material. Generally, more thickness of filling material implies lower peak shear strength. However, this material can also contribute to increase cohesion, and so the effects of filling depend enormously on the type of material and joint properties.

- Water pressure influence. The presence of fluids (normally water) reduce effective stresses (see section 2.4.4), may alter the properties of filling materials and also trigger permeability changes due to joint aperture (see section 2.4.3). Additionally, in non-saturated soils or rock masses, saturation eliminates suction forces, which may end up having a similar effect to friction angle decrease.

2.4.3. Discontinuities: hydraulic behaviour

2.4.3.1. Cubic law

To start with, let's consider a single fracture in 2D. Liquid and gas flow can be computed using Darcy's law, in which an adequate expression to calculate the fracture intrinsic permeability must be used. From an hydraulic point of view, an analogy between one-dimensional laminar flow between two plates (separated by a distance *b*) and flow through a single fracture of aperture *b* (when no filling material is considered) can be made. Then, imposing fluid equilibrium and using basic hydraulic laws, the so-called cubic law is obtained:

$$\mathrm{Q}_{\alpha} = -\frac{\rho_{\alpha} g b^{3}}{12\mu_{\alpha}} \nabla \mathrm{h}_{\alpha} \tag{13}$$

where Q_α is the total flow rate (discharge, in units of $L^3\ T^{-1}$), *h* is the head (units of length) and *b* is fracture aperture (or distance between plates in the analogy). Note the importance of *b* in the cubic law and how it affects the total flow rate of the α-phase.

Different flow regimes would lead to different expressions, but non-laminar flow is rarely considered in these type of media. If a fracture is filled with a porous material, Darcy's law (3) is recuperated, using the porous medium intrinsic permeability or conductivity and computing total flow rate as *b* times q_α. Note the linear relationship between total flow rate and *b*, which indicates that joint aperture is not so critical in this case (b vs. b^3).

2.4.3.2. Intrinsic permeability of a single fracture

From equation (13), and accounting for the relationship between total flow rate and volumetric flux, the intrinsic permeability and conductivity associated to the fracture can be obtained quite easily. The concept of fracture transmissivity (expressed in units of $L^2\ T^{-1}$) is also introduced.

- Fracture intrinsic permeability $\mathrm{k} = \frac{\mathrm{b}^2}{12}$ (14.a)
- Fracture conductivity $\mathrm{K}_\alpha = \frac{\rho_\alpha \mathrm{g} \mathrm{b}^2}{12\mu_\alpha} = \frac{\rho_\alpha \mathrm{g}}{\mu_\alpha}\mathrm{k}$ (14.b)
- Fracture transmissivity $\mathrm{T}_\alpha = \frac{\rho_\alpha \mathrm{g} \mathrm{b}^3}{12\mu_\alpha} = \mathrm{K}_\alpha \mathrm{b}$ (14.c)

Now, a Darcy-like expression for joint flow can be obtained:

$$\mathrm{q}_\alpha = -\frac{\mathrm{Q}_\alpha}{\mathrm{b}} = -\frac{\rho_\alpha \mathrm{g} \mathrm{b}^2}{12\mu_\alpha}\nabla \mathrm{h}_\alpha \tag{15}$$

It is important to point out the scalar character of all these magnitudes, in contrast with equation (3), as the focus is on the fracture direction only.

2.4.3.3. Equivalent intrinsic permeability of a set of fractures

Let's consider parallel joints of aperture *b* and separated by a distance *s*. If we assimilate the flow rate through one fracture to a thickness *s* of porous medium (see figure 8), we obtain the following expression for the volumetric flux *q*:

$$\mathrm{q}_\alpha = -\frac{\mathrm{Q}_\alpha}{\mathrm{s}} = -\frac{\rho_\alpha \mathrm{g} \mathrm{b}^3}{12\mu_\alpha \mathrm{s}}\nabla \mathrm{h}_\alpha \tag{16}$$

Then, from equations (14), the equivalent intrinsic permeability and conductivity can be obtained:

- Intrinsic permeability of the homogeneous equivalent medium $\mathrm{k} = \frac{\mathrm{b}^3}{12\mathrm{s}}$ (17.a)
- Conductivity of the equivalent medium $\mathrm{K}_\alpha = \frac{\rho_\alpha \mathrm{g} \mathrm{b}^3}{12\mu_\alpha s}$ (17.b)

Note the physical meaning of expressions (17.a) and (17.b). The cubic law (13) which expresses the total flow rate through a fracture has been used and divided by a porous medium thickness equal to *s* (i.e. the space between parallel fractures), not the fracture aperture b. By so doing, a flux and an intrinsic permeability referred to the whole equivalent homogeneous medium is obtained, unlike the previously obtained expressions (14) and (15) that were valid for a single joint only.

It is now possible to add the contribution of fractures to the intrinsic permeability of the porous matrix, both expressed as scalar values. Then, the equivalent intrinsic permeability in the direction parallel to the fracture can be calculated as:

$$\mathrm{k} = \mathrm{k}_{\mathrm{matrix}} + \frac{\mathrm{b}^3}{12\mathrm{s}} \tag{18}$$

where $\mathrm{k}_{\mathrm{matrix}}$ is the reference intrinsic permeability of the matrix of porous material, that is, the material without fractures. The rest of parameters have already been described in (16). Note that the permeability of the matrix will be relevant only for very low apertures; otherwise, the second term will dominate.

For k to have its true physical meaning, it should be written as a permeability tensor. According to Darcy's law (3) and expression (18), the intrinsic permeability tensor and the α-phase flux in the direction of the discontinuity (principal directions 1, 2) are written as:

$$[\mathbf{k}]_{12} = \mathbf{I}\mathrm{k}_{\mathrm{matrix}} + \mathbf{n}\mathbf{n}^{\mathrm{T}}\frac{\mathrm{b}^3}{12\mathrm{s}} \tag{19.a}$$

$$[\mathbf{q}_{\alpha}]_{12} = -\frac{[\mathbf{k}]_{12}\,\mathrm{k}_{\mathrm{r}\alpha}}{\mu_{\boldsymbol{\alpha}}}\,\boldsymbol{\nabla}\mathrm{h}_{\alpha} = -\frac{\mathrm{k}_{\mathrm{r}\alpha}}{\mu_{\boldsymbol{\alpha}}}\left(\mathbf{I}\mathrm{k}_{\mathrm{matrix}} + \mathbf{n}\mathbf{n}^{\mathrm{T}}\frac{\mathrm{b}^3}{12\mathrm{s}}\right)(\boldsymbol{\nabla}\mathrm{P}_{\alpha} + \rho_{\alpha}\,\mathrm{g}\,\boldsymbol{\nabla}\mathrm{z}) \tag{19.b}$$

where the vector ***n*** gives the direction parallel to the discontinuity, $\boldsymbol{n}^T$ is the transposed vector and ***I*** is the 2 x 2 or 3 x 3 identity matrix. Subindex 1,2 indicate the matrix base or the orientation of axes.

Note that the expansion of expression (19.a) leads to the following matrix, which is actually the intrinsic permeability tensor expressed in the principal directions 1,2 (set parallel and perpendicular to the fracture direction):

$$[\mathbf{k}]_{13} = \begin{bmatrix} \mathrm{k}_1 & 0 \\ 0 & \mathrm{k}_2 \end{bmatrix} = \begin{bmatrix} \mathrm{k}_{\mathrm{matrix}} + \frac{\mathrm{b}^3}{12\mathrm{s}} & 0 \\ 0 & \mathrm{k}_{\mathrm{matrix}} \end{bmatrix} \tag{20}$$

The orientation of discontinuities is assumed to be known and it can correspond to different situations: (a) bedding planes induced by rock sedimentation or buffer material compaction; (b) contact between different materials; (c) cracks which have been induced by thermal desiccation; (d) discontinuities determined by an appropriate mechanical constitutive model. [8]

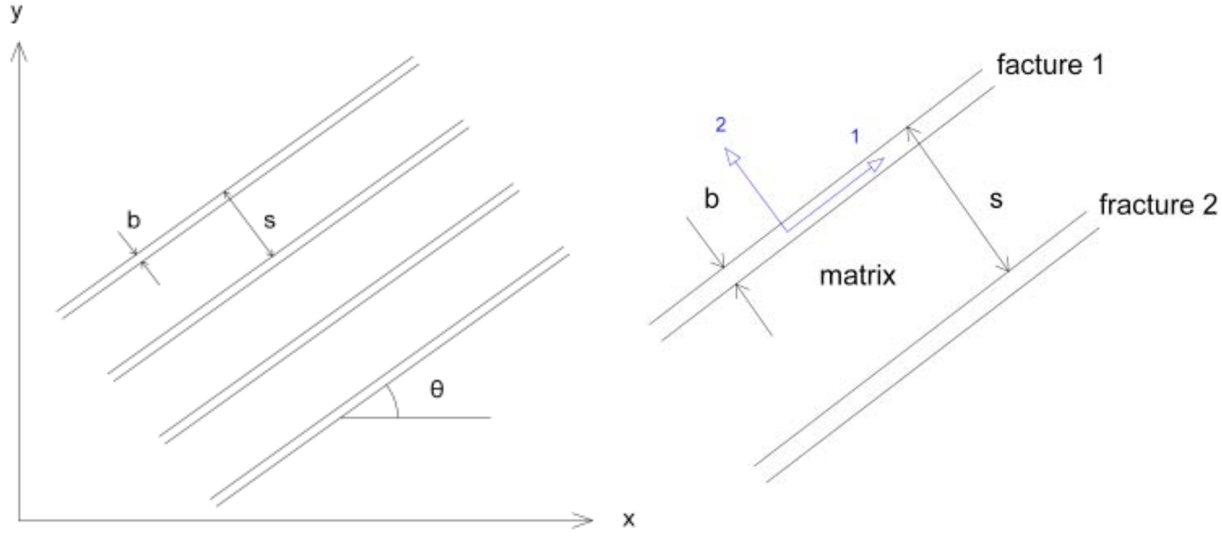

Figures 8 : Scheme depicting a family of discontinuities, aperture and spacing of fractures as well as reference axes

If a discontinuity family making an angle θ with the horizontal axis is considered (see figure 8), and expressions (19.a) and (20) are referred to the oriented axes 1 and 2, then the intrinsic permeability matrix in the *x*,y axes can be obtained by multiplying expression (20) by the corresponding rotation matrix $\boldsymbol{P}$:

$$[\mathbf{k}]_{\mathrm{xy}} = \mathbf{P}^{\mathrm{T}}\,[\mathbf{k}]_{12}\ \mathbf{P} = \begin{bmatrix} \cos\theta & \sin\theta \\ -\sin\theta & \cos\theta \end{bmatrix} \begin{bmatrix} k_1 & 0 \\ 0 & k_2 \end{bmatrix} \begin{bmatrix} \cos\theta & -\sin\theta \\ \sin\theta & \cos\theta \end{bmatrix}$$

$$[\mathbf{k}]_{\mathrm{xy}} = \begin{bmatrix} k_1\cos^2\theta + k_2\sin^2\theta & (k_2 - k_1)\sin\theta\cos\theta \\ (k_2 - k_1)\sin\theta\cos\theta & k_1\sin^2\theta + k_2\cos^2\theta \end{bmatrix} \qquad (21.\mathrm{a})$$

As a result, the mean 2D flux of the α-phase generated by this family of discontinuities (written in the matrix form) is:

$$[\mathbf{q}_\alpha]_{\mathrm{xy}} = \begin{pmatrix} q_x \\ q_z \end{pmatrix} = -\frac{k_{r\alpha}}{\mu_\alpha} \begin{bmatrix} k_{xx} & k_{xy} \\ k_{yx} & k_{yy} \end{bmatrix} \begin{pmatrix} \partial_x h \\ \partial_y h \end{pmatrix}$$

$$[\mathbf{q}_\alpha]_{\mathrm{xy}} = \begin{pmatrix} q_x \\ q_y \end{pmatrix} = -\frac{k_{r\alpha}}{\mu_\alpha} \begin{bmatrix} k_1\cos^2\theta + k_2\sin^2\theta & (k_2 - k_1)\sin\theta\cos\theta \\ (k_2 - k_1)\sin\theta\cos\theta & k_1\sin^2\theta + k_2\cos^2\theta \end{bmatrix} \begin{pmatrix} \partial_x h \\ \partial_y h \end{pmatrix} \qquad (21.\mathrm{b})$$

where $\partial_x h$ and $\partial_y h$ are the partial derivatives of *h* with respect to *x* and *y*.

2.4.3.4. Equivalent intrinsic permeability when two or more families of joints exist

Finally, if more than one set or family exists ($i = 1 : N$) the total generated flux can be calculated as the following sum:

$$[\mathbf{q}_\alpha]_{xy}^{tot} = \begin{pmatrix} q_x^1 \\ q_y^1 \end{pmatrix} + \begin{pmatrix} q_x^2 \\ q_y^2 \end{pmatrix} + \ldots = -\frac{k_{r\alpha}}{\mu_\alpha} \begin{bmatrix} k_{xx}^1 + k_{xx}^2 + \ldots & k_{xy}^1 + k_{xy}^2 + \ldots \\ k_{yx}^1 + k_{yx}^2 + \ldots & k_{yy}^1 + k_{yy}^2 + \ldots \end{bmatrix} \begin{pmatrix} \partial_x h \\ \partial_y h \end{pmatrix}$$

$$[\mathbf{q}_\alpha]_{xy}^{tot} = -\frac{k_{r\alpha}}{\mu_\alpha} \sum_{i=1}^{N} [\mathbf{q}_\alpha]_{xy}^{i} = -\frac{k_{r\alpha}}{\mu_\alpha} \left(\sum_{i=1}^{N} \mathbf{P}^{iT} [\mathbf{k}]_{12}^{i} \mathbf{P}^{i}\right) \boldsymbol{\nabla} h_\alpha \tag{22}$$

where the superindex *i* refers to each family and subindex 1,2 to the principal directions, which obviously depend on the orientation of the family.

With (19.a), (19.b), (21.b) and (21.c) we have already obtained expressions for permeability and flux in 2D which take into account the effects of both rock matrix and fractures. While expressions (19.a) and (19.b) are written in the oriented axes (principal directions), (21.b) and (21.c) are written in the horizontal and vertical x,y axes. Additionally, an expression to compute the total flux accounting for the different families of discontinuities has also been obtained, as written in (22).

2.4.3.3. Variation of capillary pressure with joint aperture

As it has been shown, fracture aperture has a big effect on intrinsic permeability. Nevertheless, it is not the only hydraulic process that is included in the fracture, since aperture changes also induce variation of capillary pressure. According to Laplace's law,the pressure difference between the inside and outside of a curved surface that separates two inmiscible fluids can be related to the surface tension as follows:

$$\Delta P = \sigma\left(\frac{1}{r_1} + \frac{1}{r_2}\right) \tag{23.a}$$

where ΔP is the change of pressure (or Laplace's pressure), σ the surface tension and r_1 and r_2 are two perpendicular radii of curvature. Note that, for an spherical shape, both radii are the same and expression (23.a) is simplified. [8]

Now let's assume, again, a fracture of aperture *b*. Imposing $(1/r_1) = 0$ and $r_2 = b/2$ (assuming that the wetting angle is equal to zero), the capillary pessure necessary to desaturate the fracture (P_0) is obtained:

$$P_0 = \frac{2\sigma}{b} \tag{23.b}$$

It is clear, indeed, how P_0 depends on fracture aperture *b*. Since permeability variation with aperture has already been discussed, expression (18) can be combined with (23.a) to obtain the capillary pressure to start desaturation as a function of permeability:

$$P = P_0 \frac{\sqrt[3]{k_0}}{\sqrt[3]{k}} \tag{24.a}$$

where P_0 is the capillary pressure for a reference permeability k_0, which can be assumed to be the initial permeability of the fracture. Note that *P* decreases when the fracture opening occurs and permeability increases. Surface tension does not appear in this expression as we have considered that temperature remains constant. If not, *P* has to be scaled with this tension calculated at different temperatures:

$$\mathrm{P} = \mathrm{P}_0 \frac{\sqrt[3]{\mathrm{k}_0}}{\sqrt[3]{\mathrm{k}}} \ \frac{\sigma}{\sigma_0} \tag{24.b}$$

where σ_0 is the corresponding surface tension at temperature T_o, this is, $\sigma_0 = \sigma(T_0)$. Note that *P* will decrease with temperature because surface tension also does.

2.4.3.4. Retention curve

As a first aproximation, all these joint aperture (and permeability) changes can now be related to the degree of saturation by introducing the capillary pressure associated with the discontinuity in the standard retention curve of Van Genuchten (Van Genuchten, 1980):

$$\mathrm{S_l} = \left[1 + \left(\frac{\psi}{\mathrm{P}}\right)^{\frac{1}{1-\lambda}}\right]^{-\lambda} \tag{25}$$

where S_l is the (liquid) degree of saturation, ψ is the current suction (defined as the difference between the gas and liquid pressure), and λ and *P* (given by expression 24.a or 24.b) are model parameters. [8]

Finally, combining expressions (24.a) or (24.b) and the Van Genuchten retention curve (25) both capillary pressure and degree of saturation variaton due to fracture opening can be obtained.

2.4.4. Hydro-mechanical coupling

2.4.4.1. Effective stressess law

To start with, it is important to make reference to the effective stresses law, first proposed by Terzaghi in 1925 for saturated media and originally applicable to soils. For rock matrix, the concept is similar, but now a new parameter called Biot's coefficient has to be considered. This coefficient appears as a correction for water pressure. Actually, the effective stresses law for soils is a particular case of the more general expression, in which Biot's coefficient is equal to 1.

All in all, the following expressions should be mentioned:

- Original Terzaghi equation $$\boldsymbol{\sigma}' = \boldsymbol{\sigma} - \mathbf{I}\,\mathrm{u} \tag{26.a}$$
- Effective stress law for rock matrix $$\boldsymbol{\sigma}' = \boldsymbol{\sigma} - \mathbf{I}\,\mathrm{u}\,\eta \tag{26.b}$$

where **σ** is the stress tensor in 3D, *u* is the water pressure, ***I*** the 3 x 3 identity matrix and η is the Biot's coefficient.

For discontinuities the idea is, again, the same, but instead of writing the law in terms of the stress tensor in one point, normal stresses between opposite faces of the fracture are considered. In other words, fracture orientation is now a key aspect of the problem, so stresses and strains are no longer referred to a point but to the discontinuity plane itself. Since water pressure in the context of effective stresses law has influence in the normal direction only, (26.a) can be written as:

$$\sigma'_{\mathrm{N}} = \sigma_{\mathrm{N}} - \mathrm{u} \tag{27}$$

where the subindex *N* has been included to point out that the focus is now on the direction perpendicular to the fracture (normal stress).

Nevertheless, in general, geological media are not saturated of water, but voids contain air or gas too. Thus, gas pressure is also relevant, and the concept of effective net stress is defined:

$$\boldsymbol{\sigma}'_{\mathrm{net}} = \boldsymbol{\sigma} - \mathbf{I}\ \max\left\{\mathrm{P_g}\,,\mathrm{P_l}\right\} \tag{28}$$

where $\boldsymbol{\sigma}$ is the total stress tensor and P_g , P_l are, respectively, the gas and liquid pressures. Note that here Biot's coefficient has been assumed to be equal to one to simplify the expression. It is straightforward to see that expression (28) is equivalent to Terzaghi's law when the medium becomes saturated.

The effective net stress law can also be defined in terms of the joint as:

$$\sigma'_{N,net} = \sigma - \max\left\{\mathrm{P_g}\,,\mathrm{P_l}\right\} \tag{29}$$

where, again, *N* indicates direction perpendicular to the joint.

2.4.4.2. HM behaviour of joints

It is now interesting to comment some experimental results regarding how mechanical aspects of joints affect their hydraulic behaviour. Only a brief summary is presented here, basically regarding how compression and shearing affect joint permeability as reported by some authors after analysing several experimental data.

The behaviour of joints under different normal stresses has been extensively studied. Experimental results obtained by Hans (2002) show that the higher the normal stress, the lower the intrinsic transmissivity of the joint. This is due to the reduction of the void space between the joint walls, the increase in the contact area and the changes in tortuosity. Even when normal stresses are no longer being applied, an irreversible behaviour can be observed. [1]

As for HM coupling under shearing, the joint behaviour in this case is slightly more complex. When a shear stress is applied (before the peak conditions are attained) transmissivity decreases at first, but then increases again. This happens when peak conditions are met, and the changes in transmissivity are not minor whatsoever, since an increase of approximately two orders of magnitude can be observed. Joint dilatancy plays the most relevant role in this context (Lee and Cho, 2002) and is the main reason for transmissivity increase. An interesting observation is that, even if dilatancy increases continuously due to the evolution of relative shear displacements, joint permeability reaches a constant value. The generation of gouge material caused by the breakage of asperities is responsible for this behaviour. The roughness degradation depends on the strength of the asperities, the applied normal load and shear stiffness. [1]

CHAPTER 3

NUMERICAL METHODS IN CCS SIMULATIONS

3.1. Multiphase flow simulators: an overview

All simulaton models are based on a set of governing equations which have to be solved using all the available tools that computational engineering provides. It is indeed the type of numerical method used to translate these governing equations into a finite form (this is, appropriate for computational analysis) that distinguishes one simulator from the other. In terms of the physical models considered and the numerical methods used, a wide range available of carbon storage simulators exists. The main characteristics of some available packages/simulators are shown in table 2. The complexity of each simulator depends on the number of fluid phases and components considered, as well as the discretization methods used (Jiang, 2011).

Table 2: Overview of the most relevant simulators for carbon storage purposes (Jiang, 2011) [13]

Simulators	Main applications	Discretization/integration methods
ATHENA/ ACCRETE	Thermal multiphase 3D-reactive-transport numerical mode	FInite volume method, reaction and flow iteratively coupled
CHILLER (companion to SOLVEQ)	Multi-component multi-phase equilibrium geochemical calculation software based on minumum free-energy	Newton-Raphson method for solving a system of mass balance and mass action equations
CODE_BRIGHT	Solution of the flow, heat and geo-mechanical model equations. Module for simulating carbon dioxide properties recently implemented.	Finite element method for spatial discretisation; implicit finite-difference for temporal discretisation
COORES	Multi-component three-phase and 3D fluid flow in heterongeneous porous media	Finite volume method for spacial discretisation; implcit temporal discretisation
DUMUX	Multi-component three-phase and 3D fluid flow in heterogeneous porous media	Vertex-centered finite volume method for spatial discretisation; implicit temporal discretisation
ECLIPSE 100/300	Three-phase and 3D fluid flow in porous media with cubic EOS, pressure dependent permeability values, etc.	Integrated finite difference method (IFDM) with irregular spatial discretisation; implicit temporal discretisation
ELSA	Semi-analytical tool to estimate fluid distributions and leakage rates involving vertically integrated sharp-interface equations and local 3D well models	Spatial discretisation is essentially grid free; several schemes for temporal discretisation including implicit pressure, explicit saturation, etc.
FEFLOW	Solving the groundwater flow equation with mass and heat transfer, including multi-component chemical kinetics	Finite element method for spatial discretisation; implicit/explicit/Crank-Nicolson temporal discretisation
FEHM	Fully coupled heat, mass and stress balance equations for 3D, non.isothermal, multiphase fluid flow in porous media	Control volume finite element method for spatial discretisation; implicit tmeporal discretisation
GEM	EOS compositional reservoir simulator	IFDM for spatial discretisation; imlicit temporal discretisation

Geochemist's workbench	Interactice aqueous geochemistry tools	Equilibrium modeling, reaction path modeling calculations, etc.
IPARS-CO_2	Parallel multi-block, multi-physics approach for multiphase flow in porous media	Mixed finite element method for space discretisation; implicit pressure, explicit concentration sequential algorithm for temporal discretisation
MIN3P	Multi-component reactive transport modelling in variably saturated porous media	Finite volume method for spatial discretisation; implicit temporal discretisation
MODFLOW	Solving the groundwater flow equation to simulate the flow through aquifers	Finite difference method for spatial discretisation; implicit or Crank-Nicolson for temporal discretisation
MT3DMS	Modular 3D transport model simulating convection, dispersion, and chemical reactions of dissolved constituents	Finite difference/particle-tracking based Eulerian-Lagrangian/finite-volumemethod for spatial discretisation; implicit/explicit temporal discretisation
MUFTE	Isothermal and non.isothermal multi-phase flow problems including compositional effects	Vertex-centered finite volume method for spatial discretisation; implicit temporal discretisation
PFLOTRAN	Parallel 3D reservoir simulator for subsurface multi-phase, multi-component reactive flow and transport based on a continuum scale mass and energy conservation	Finite element method for spatial discretisation; implicit/semi-implicit time integration
PHAST	Simulating groundwater flow, solute transport and multi-component geochemical reactions	Finite difference method for spatial discretisation; implicit or Crank-Nicholson for temporal discretisation
PHREEQC	Low-temperature aqueous geochemical simulator	Based on an ion-association aqueous model; chemical equilibrium, kinetic, transport, and inverse-modeling calculations
RETRASO CODE_BRIGHT	Reactive transport of dissolved and gaseous species in non-isothermal saturated or unsaturated problems, geomechanics	Direct substitution approach for solving the reactive transport equations
ROCKFLOW	Multi-phase flow and solute transport processes in porous and fractured media	Finite element method for spatial discretisation; implicit temporal discretisation
RTAFF2	2D/3D non-isothermal multi-phase and multi-component flow	Finite element method for spatial discretisation; implicit temporal discretisation
SUTRA	Fluid movement and transport of either energy or dissolved substances in a subsurface environment	Hybrid finite element and integrated finite difference method for spatial discretisation; implicit temporal discretisation
TOUGHREACT+ TOUGH2	Chemically reactive multi-component, multi-phase, non-isothermal flows in porous and fractured media	IFDM for spatial discretisation; implicit temporal discretisation

3.2. About CODE_BRIGHT

3.2.1. Basic information

CODE_BRIGHT (Coupled Deformation Brine, Gas and Heat Transport) is a program designed to handle coupled problems in geological media. Although the computer code was originally developed on the basis of a new general theory for saline media, the program has been generalised for modelling thermo-hydro-mechanical (THM) processes in a coupled way in geological media. It consists of a Finite Element program developed at the Department of the Geotechnical Engineering and Geosciences of the Technical University of Catalonia (UPC) combined with the pre/post-processor GiD developed by the International Centre for Numerical Methods in Engineering (CIMNE). A set of governing and constitutive equations, as well as a special computational approach, constitute the program. The code is written in FORTRAN and is composed by several subroutines. [23]

3.2.2. Theoretical aspects

The aim of this secis to summarize the most important concepts regarding how CODE_BRIGHT approaches multiphase flow problems and, more specifically, its application to carbon storage poblems. First, the most important equations are mentioned, although the detailed list of mathematical expressions is not shown here but in Appendix B. Then, the numerical approach used by the program to solve these equations is commented and briefly explained.

3.2.2.1. Governing equations

In CODE_BRIGHT, problems are formulated in a multiphase and multispecies approach. The three phases considered are solid phase (mineral), liquid phase (water + dissolved air) and gas phase (dry air + water vapour) while the three esistent phases are mineral, water (either as liquid or evaporated in the gas phase) and air (as dry air or dissolved in the liquid phase). A clear distinction between phases and species must then be made. The volumetric mass of one species in a phase can be obtained as the product of the mass fraction of the species and the bulk density of the phase. For instance, the volumetric mass of water in gas phase can be obtained multiplying the mass fraction of water in the gas phase by the bulk density of the gas phase.

Governing equations are, in some cases, referred to each species or phase separately and, in other cases, to the medium as a whole. The equations used by CODE_BRIGHT (*Olivella et al. , 1994*) are applicable to non-isothermal multiphase flow problems, where flow of water and gas through porous deformable saline media is considered. They can be categorised into four groups: balance equations (for mass, momentum and energy), constitutive equations, equilibrium relationships and definition constraints. [23]

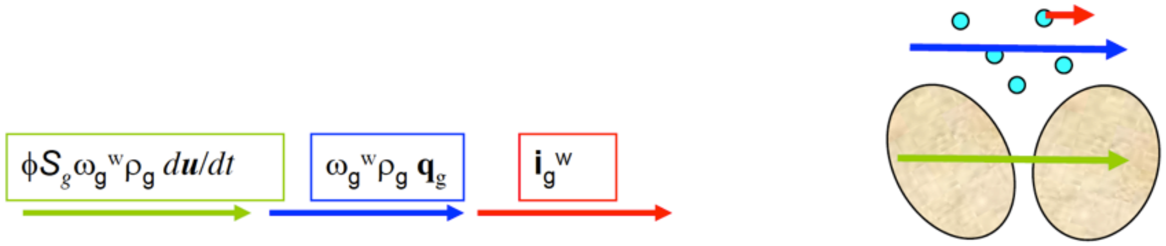

Figure 9: Scheme depicting the different types of fluxes when computing the total mass flux of water in the gas phase [24]

Mass balance equations are established by adopting the so-called compositional approach, which means that the balance is performed for water, air and mineral species instead of using liquid, gas and solid phases. The total mass flux of a species in a phase is, generally, the sum of the three following terms: (1) non-advective flux, this is, difussive and/or dispersive flux; (2) advective flux caused by fluid motion (where the aforementioned Darcy's flux plays the most relevant role); (3) advective flux caused by solid motion, and thus affected by solid velocity, porosity and the fraction of these pores occupied by the species in the corresponding phase. The relative contribution of each flux term is not always the same (for instance, the third term can be considered to be equal to zero when solid deformation is negligible). [23] Figure 9 depicts each term for water in gas phase with the corresponding expression for the generated flux: non-advective flux in red, advective flux caused by fluid motion in blue and advective flux due to solid motion in green. The mass balance is performed for each species, so to obtain:

- **Mass balance of solid** (see equations 1 to 3 in Appendix B):

$$\frac{\partial}{\partial \mathrm{t}}(\text{mass of solid})+\text{divergence}\begin{pmatrix}\text{total fluxes}\\\text{of salt}\end{pmatrix}=\begin{pmatrix}\text{external supply}\\\text{of salt}\end{pmatrix}$$

- **Mass balance of water** (see equations 4 to 5 in Appendix B):

$$\frac{\partial}{\partial \mathrm{t}}\begin{pmatrix}\text{mass of water in}\\\text{liquid and gas phase}\end{pmatrix}+\text{divergence}\begin{pmatrix}\text{total fluxes}\\\text{of water}\end{pmatrix}=\begin{pmatrix}\text{external supply}\\\text{of water}\end{pmatrix}$$

- **Mass balance of air** (see equation 6 in Appendix B)

$$\frac{\partial}{\partial \mathrm{t}}\begin{pmatrix}\text{mass of air in}\\\text{liquid and gas phase}\end{pmatrix}+\text{divergence}\begin{pmatrix}\text{total fluxes}\\\text{of air}\end{pmatrix}=\begin{pmatrix}\text{external supply}\\\text{of air}\end{pmatrix}$$

Momentum balance is referred to the medium as a whole and reduces to the equilibrium of stresses if the inertial terms are neglected. [23] Its expressions depends on the stress tensor and the vector of body forces (see equation 7 in Appendix B):

$$\text{divergence}\begin{pmatrix}\text{tensor of}\\\text{total stresses}\end{pmatrix}+\begin{pmatrix}\text{vector of}\\\text{body forces}\end{pmatrix}=\begin{pmatrix}0\\0\end{pmatrix}$$

Internal energy balance for the porous medium is established by considering the internal energy in each phase (solid, liquid and gas). In this case, both energy fluxes due to conduction through the porous medium and caused by mass motion are considered, but the difussive term for heat transport (i.e. conduction of heat) is much larger than the term concerning non-advective flux caused by velocity of fluids. Additionally, an external energy supply can also be taken into account.

The balance of internal energy in the porous medium as a whole is reduced to the balance of enthalpy because, in geological media, enthalpy variations produced by changes in temperature are very large in comparison to energy variations due to deformation work. [23] For the detailed formulation, see equation 8 in Appendix B.

$$\frac{\partial}{\partial \mathrm{t}}\begin{pmatrix}\text{internal energy in solid,}\\ \text{liquid and gas phase}\end{pmatrix} + \text{divergence}\begin{pmatrix}\text{tensor fluxes}\\ \text{of energy}\end{pmatrix} = \begin{pmatrix}\text{external supply}\\ \text{of heat}\end{pmatrix}$$

3.2.2.2. Constitutive and equilibrium laws

All the aforementioned equations must be associated to a set of necessary constitutives and equilibrium laws. Constitutive equations link independent variables (or unknowns) to dependent variables. Hence, once constitutive equations are substituted in the balance equations, these are finally written in terms of the unknowns. On the other hand, equilibrium laws relate variables assuming chemical equilibrium of the different species (air and vapour) in phases (liquid gas), which is a valid assumption in this case since chemical processes are fast compared to transport processes. [23]

The constitutives equations that should be incorporated in the general formulation, as well the the dependent variables computed using these laws are:

- Darcy's law: used to compute liquid and gas advective fluxes
- Fick's law: used to compute vapour and air non-advective fluxes
- Fourier's law: used to compute conductive heat flux
- Retention curve: used to compute the liquid phase degree of saturation
- Mechanical constitutive model: used to compute the stress/strain variables
- Phase density: used to compute liquid density
- Gases law: used to compute gas density

As for the equilibrium restrictions and associated variables, the following expressions are included in CODE_BRIGHT:

- Henry's law: used to computed air dissolved mass fraction
- Psychrometric law: used to compute the vapour mass fraction

After properly combining all the aforementioned expressions, balance equations are finally written in terms of the unknowns only, as listed in table 3.

EQUATION	VARIABLE NAME	VARIABLE
equilibrium of stresses	displacements	$\boldsymbol{u}$
balance of water mass	liquid pressure	P_l
balance of air mass	gas pressure	P_g
balance of internal energy	temperature	T

Table 3: Equation and variable summary [23]

3.2.2.3. Boundary conditions

Both in the balance and equilibrium of stresses equation, a divergence term appears, following a structure that is quite typical in this kind of differential equations. Application of Green's theorem (which gives the relationship between a line integral around a simple closed curve and a double integral over the surface bounded by it) produces new terms that represents fluxes or stresses over or on the boundaries. In the actual numerical calculation, these terms are substituted by nodal flow rates or stresses, this is, the corresponding conditions set for each boundary of the domain, properly discretised. We can have:

- Mechanical problems: forces and displacement rates in any direction and at any node.
- Hydraulic problem: mass flow rate of water and air prescribed and liquid/gas pressure prescribed at any node.
- Thermal problem: heat flow rate prescribed and temperature prescribed at any node.

3.2.3. Numerical approach

3.2.3.1. General ideas

The set of PDE's (Partial Differential Equations) which made up the expressions used to describe the thermo-hydro-mechanical processes is solved numerically. To start with, both space and time have to be discretized using the following numerical techniques:

- Discretization in space: application of the **finite element method**. Linear interpolation functions on the mesh elements are used, as well as analytical or numerical integration depending on the type of element considered. For the mechanical problem, selective integration for quadrilateral (or quadrilateral prisms) elements is used. As for the flow equations, they are solved using element-wise and cell-wise approximations, which are independent of the type of integration performed.

- Discretization in time: **finite differences** and implicit scheme are used. Two intermediate points are defined between the initial t^k and final t^{k+1} times of an interval. One represents the point where the equation will be accomplished ($t^{k+\theta}$) and the other is the point where the non-linear functions are computed ($t^{k+\varepsilon}$).

Once the space and time discretization are applied, a non-linear system of algebraic equations results. To find an iterative scheme, the **Newton-Raphson method** is adopted. If ***r*** are the residuals (or errors) obtained after application of the FEM and ***X*** is the vector of unknowns in every node *i*, *i=1:n*, of the finite element mesh, the iterative scheme after time discretization can be written as:

$$\mathbf{X}^{\mathrm{k}+1,l+1} = \mathbf{X}^{\mathrm{k}+1,l} - \mathbf{r}\,(\mathbf{X}^{\mathrm{k}+1,l}) \cdot \frac{\partial\,\mathbf{X}^{k+1}}{\partial\mathbf{r}\,(\mathbf{X}^{k+1})} \tag{30.a}$$

$$\frac{\partial\mathbf{r}\,(\mathbf{X}^{k+1})}{\partial\,\mathbf{X}^{k+1}}\,(\mathbf{X}^{k+1,l+1} - \mathbf{X}^{k+1,l}) = -\mathbf{r}\,(\mathbf{X}^{\mathrm{k}+1,l}) \tag{30.b}$$

where l indicates interation and *k+1* the time step in question. [23]

Finally, a system of linear equations results. This system can be solved applying either LU decomposition along with back-substitution (non-symetric matrix) or conjugate gradients squared method.

The following scheme shows (in a very simplified way) the whole process:

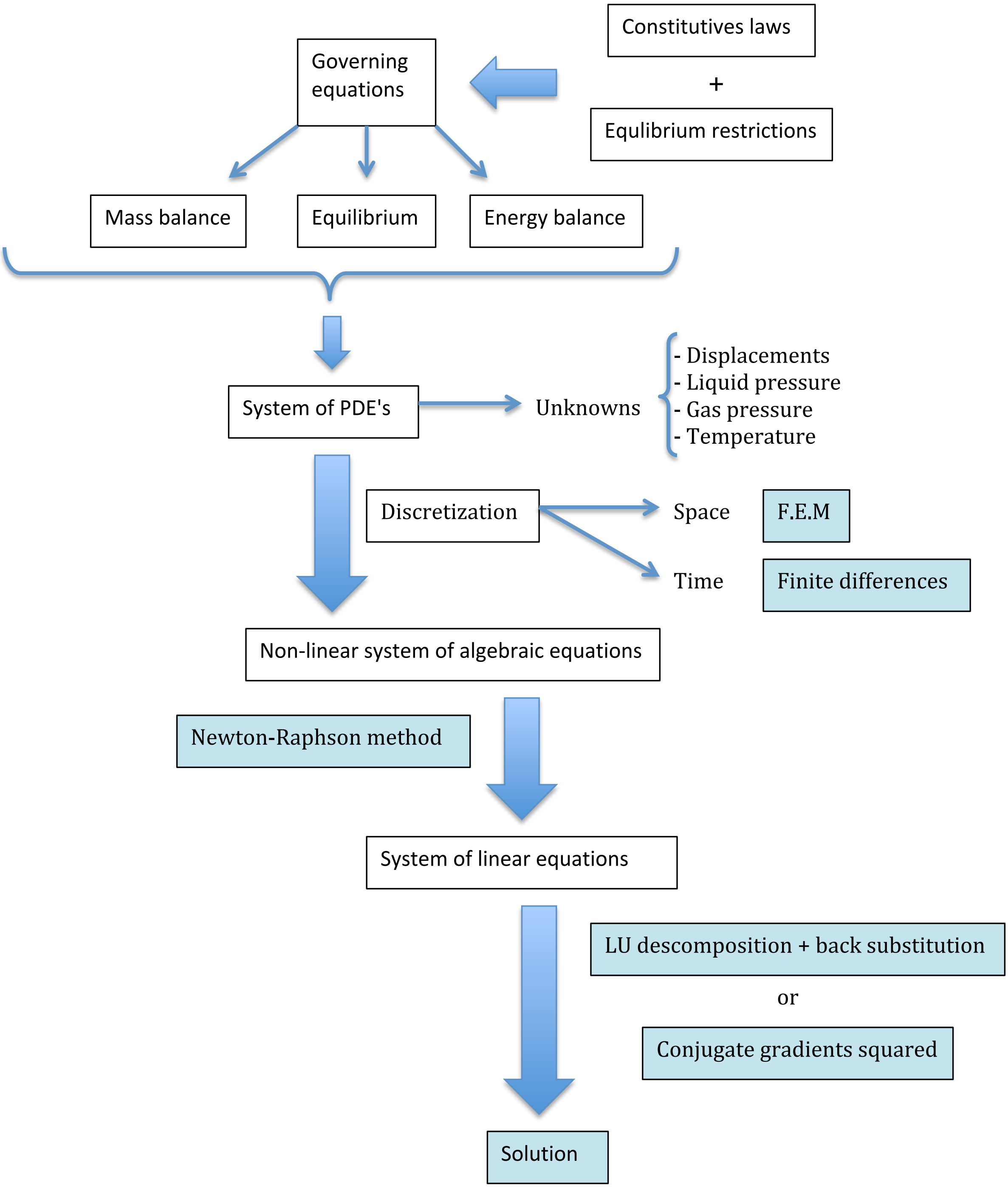

3.2.3.2. FEM discretization and summary of different terms

CODE_BRIGHT approaches the numerical discretization of the problem using the standard Galerkin method with some variations in order to facilitate computation. The Galerkin methods are a class of methods for converting a continuous operator (in this case, partial differential equations) to a discrete problem, working with the concept of weak formulation. Details about numerical solution of hydrogeological problems are not going to be given here, but general aspects related to this solutions can be found in Huyakorn and Pinder (1983). Since the differential partial equations involved in this type of hydrogeological problems involve various terms with different structures, each of them requires specific treatment, described in detail in *Olivella et al. , 1996*. [23]

The terms that can be distinguished in both the mass and energy balance equations are:

- Storage terms, which represent the variation of mass or energy content (not related to volumetric strain or porosity variation). It is calculated by means of variables such as degree of saturation, denstity, porosity, mass fraction and specific energy.

- Advective fluxes caused by motion of fluids are computed using Darcy's law. Except for the coefficients, these advective fluxes are implicit in terms of pressure gradients.

- Non-advective fluxes, computed through Fick's law, which are proportional to gradients of mass fractions. Note that these gradients of mass fractions do not belong to the set of unknowns, as it has been noted in table 3. As for the conductive heat flux, Fourier's law, which expresses proportionality to temperature gradients, is used.

- Volumetric strain terms which are, in fact, storage terms too. They are proportional to $\nabla \cdot \frac{d\boldsymbol{u}}{dt}$ which is equivalent to the volumetric strain rate.

- Sink/source terms.

For further information about how each of the aforementioned terms is treated in CODE_BRIGHT, as well as other numerical aspects which could be of interest but not essential to understand how the program works, see Appendix B.

3.3. Modelling discontinuities in coupled problems

3.3.1. Different approaches

Generally speaking, at the moment CODE_BRIGHT offers two already implemented possibilities for simulating the behaviour of faults and fault zones: zero thickness joints and joints embedded in finite elements (see figure 10). While in the first approach joint behaviour is defined by an interface which includes all the involved thermo-hydro-mechanical models and properties, the second allows to mantain continuity within the whole geological media and depends on the behaviour of the chosen continuum model. In addition, the concept of strong discontinuity has recently been applied to CODE_BRIGHT, although its full implementetion is still in process.

An interface or single fracture represented as a zero thickness element is an appropriate approach in those cases where the thickness of the fault is neglegible compared to the size of the problem. The mechanical behaviour of the interface can be simulated using different fracture models (such as those mentioned in Chapter 2) but also adding more complexity by considering a viscoplastic behaviour of the joint. These interfaces have the properties of tensile strength, normal and shear stiffnesses, dilation, cohesion and friction, among others. As for the hydraulic behaviour, these interfaces also include properties such as permeability in the direction of the plane of discontinuity as well as joint aperture so as to compute its variation. Fluid pressure within the joint is also taken into account, affecting the effective normal stress accordingly and, thus, affecting the shear strength too. A more detailed explanation of this model is given in section 3.3.2.

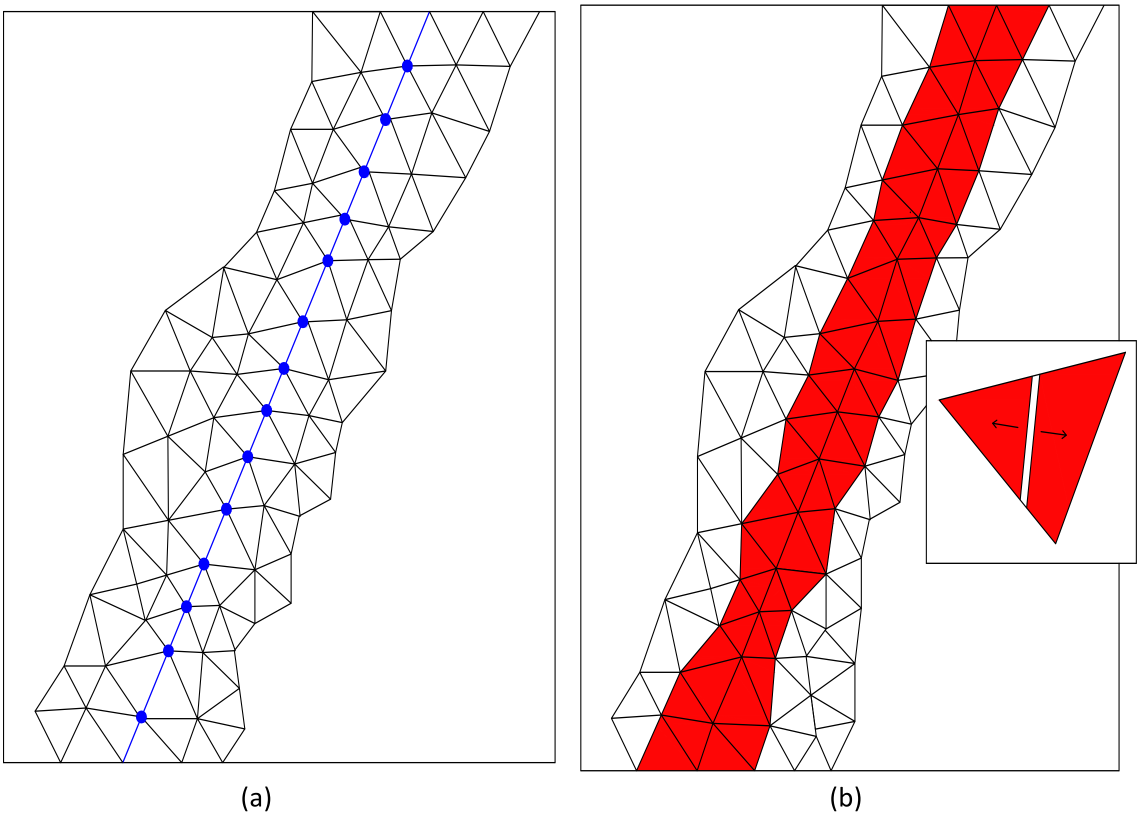
(a) (b)

Figure 10: Pictures depicting fractures or fault zones using (a) a zero thickness or joint element and (b) the concept of joints embedded in finite elements.

On the other hand, approaching the problem from the perspective of embedded joints implies a completely different concept. In this case, the hypothesis of continuity is maintained all the time, and the mechanical behaviour of the media is represented by continuum constitutive models of various sophistication, from the simplest isotropic linear elastic to the more complex elasto-plastic or visco-plastic models. It is in the hydraulic behaviour of the media where the embedded joints play an important role. The model considers a set of joints located within the finite elements (with properties such as separation or initial opening) which can change their aperture and, consequently, their permeability, according to the deformation (strains) computed from the mechanical constitutive model. By so doing, hydro-mechanical coupling is taken into account and preferential paths can be simulated within the otherwise continuous medium. See section 3.3.3 for more details.

Finally, the "strong discontinuity" approach is based on the idea of creating a constitutive model capable of describing the behaviour of a non-continuous medium (in this case, including jumps of the displacement field), just like the equations of continuum mechanics do with continuous media. By implementing this already developed theory in CODE_BRIGHT, a more sophisticated model accounting for strong discontinuities within the finite element mesh is obtained. Nevertheless, this is still a work in progress and only a brief description is included in section 3.3.4.

3.3.2. Zero thickness elements (Zandarín, M.T. et al.)

The formulation for the analysis of thermo-hydro-mechanical (THM) problems in joints was first presented by M.T. Zandarín et al. (2013). The work was developed following the basic ideas that rule CODE_BRIGHT approach to THM problems, this is, establishing equilibrium, mass balance and energy balance, formulated taking into account both air and water species. The main innovation consisted in developing joint elements and implementing them in the aforementioned general purpose finite element computer code. The model was first used to model some real cases, especially tests such as the shear hydraulic test. Joint properties such as roughness were included for different cases, and special attention to the coupling between permeability and joint deformation was paid. Additionally, a constitutive model including the effects of suction and roughness was proposed to simulate the unsaturated behaviour of rock joints.

3.3.2.1. Motivation

The mechanical behaviour of joints in various contexts has already been studied by different authors, and even finite element formulation was developed in the late 60's thanks to the pioneering contribution of Goodman et al. (1968). As for HM coupling, various studies had also been carried out, as briefly mentioned in Chapter 2. However, the effects of suction on the mechanical behaviour of rock joints had not been reported in the literature until the aforementioned studies developed by Zandarín et al. Since the fact that the prevailing suction has a very significant effect on rock strength is well-known (Oldecop and Alonso, 2001), suction is expected to be of utmost importance in fractures too. The motivation for having developed a model accounting for the effect of suction is related to the conditions found in some particular situations, such as in nuclear waste disposal designs (where initially unsaturated bentonite barriers experience strong suctions) or faults above an existing water level (which are relevant to slope stability and excavations). [1]

3.3.2.2. Basic formulation overview: governing equations

The purpose here is to give an idea of how this approach works, so detailed formulation is going to be avoided. For more information about this particular model, you can go to the series of papers written about it, which can be found in the bibliography at the end of this thesis.

The **mechanical formulation** is based on the fact that the joint elements used in this approach have double nodes and a defined mid-plane (see figure 11). The mid-plane relative displacements are interpolated using the nodal displacements and the corresponding shape functions. The vector of mid-plane displacements ($\boldsymbol{w}_{mp}$), which contains both the normal (u_n) and tangencial (u_s) relative displacements of the element's mid-plane, is computed as the vector of nodal displacements multiplied by other matricial quantities such as the matrix of shape functions and a rotation matrix (that transforms the relative displacements in the local orthogonal coordinate system into the global coordinate system). Then, the net stresses of the mid-plane ($\boldsymbol{\sigma}'_{mp}$), which contains both the normal effective stress (σ') and the tangential stress at the mid-plane (τ), can be calculated as $\boldsymbol{w}_{mp}$ affected by the stiffness matrix (***D***).

Two phase flow through a single joint is analyzed by means of the balance equations mentioned when talking about CODE_BRIGHT's theoretical approach (i.e. water, air and energy balance). The fluxes (both advective q and non-advective *i*) at mid-plane (mp) are calculated by interpolating the leak-off at the element boundaries, accounting for both transversal and lateral fluxes. The main concept of all three balances is the same as before, but now the balance is performed for a differential of joint (see figure 12). Consequently, parameters such as the opening of the joint element (*a*) or the discrete length of the joint element (*dl*) are included in the formulation. Just to give an idea of how mid-plane fluxes are computed, and in the particular case of water mass balance, transversal fluxes at mid-plane of the joint are calculated by means of the pressure drop between surfaces or boundary nodes, while longitudinal fluxes are calculated considering the average pressure in those nodes (this is, for instance, nodes 1 and 3 for mp_1 in figure 12).

The weighted residual method is applied to obtain the discrete forms of equations. Finally, the mechanical equations as well as the three balance equations are solved silmultaneously so as to obtain the values of the five unknowns: normal and shear relative displacements (u_n and u_s), the gas and liquid pressures (P_g and P_l) and the temperature (*T*).

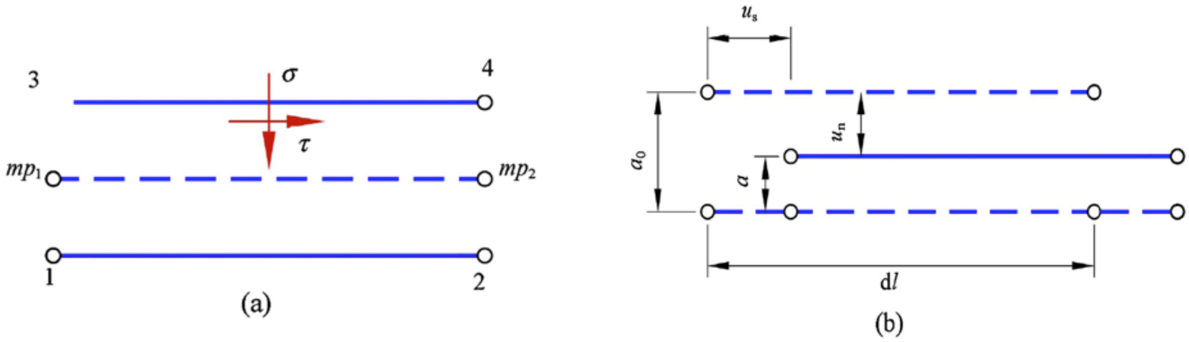

Figure 11: (a) Stresses at the mid-plane of a joint element ; (b) relative displacement at mid-plane [1]

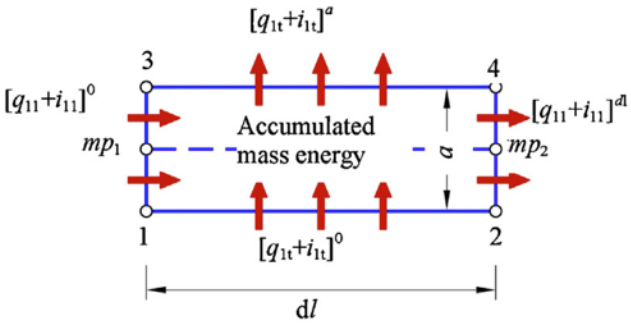

Figure 12: Scheme depicting the mass balance of a joint element. A diferential of joint *dl* is considered [1]

3.3.2.2. Basic formulation overview: constitutive equations

Having given some ideas of which equations have to be solved, now some comments about the constitutive equations used to relate all the problem variables to the independent ones (i.e. the aforementioned unknowns) are going to be made. The following two categories of consittutive models are considered:

- Mechanical model based on nonlinear elasto-viscoplastic formulation.
- Hydraulic model describing advective and diffussive fluxes, permeability evolution and heat condution.

In the **mechanical model**, the elastic formulation accounts for a nonlinear behaviour of the normal stiffness due to joint aperture, as well as a linear relationship between shear stresses and displacements by means of a shear stiffness modulus (see Chapter 2 for more details). The viscoplastic formulation, on the other hand, is based on the treatment of non-associated plasticity including a softening law associated to shear displacement. Thus, total displacements ***w*** are calculated adding a reversible elastic displacement and viscoplastic displacements, which are zero when stresses are below the threshold value defined by the yield surface. Since elastic behaviour has already been discussed in Chapter 2, only **viscoplastic formulation** (based on the formulations proposed by *Gens et al., 1990* and *Carol et al., 1997* for rock joints) is going to be briefly commented here.

According to these theories, it is necessary to define a yield surface, a plastic potential and a softening law. [1] The **yield surface** (*F*) in this model is assumed to follow an hyperbolic law (based on *Gens et al., 1990*) which depends on effective cohesion and internal friction angle (note some similarities with the simplest models presented in Appendix A). Variation of these parameters, which can be in fact associated to softening or hardening phenomena, results in a family of yield surfaces (figure 13).

The so-called **softening law** is intended to model the strain-softening behaviour of joints when subjected to shear stress. This is achieved by establishing laws that rule the degradation of strength parameters as stressing and/or displacement increases. In this case, the degradation of cohesion and friction angle depends linearly on viscoplastic relative shear displacement (based on the slip weakening model introduced by *Palmer & Rice, 1973*). Cohesion decays from the initial value c_0' to zero and the tangent of the friction angle $tg\varphi'$ decays from the peak (intact material) to the residual value as a function of a viscoplastic shear displacement (u_c^* for cohesion and $u_{tg\varphi'}^*$ for friction angle). For simplicity, mathematical formulation is not shown here.

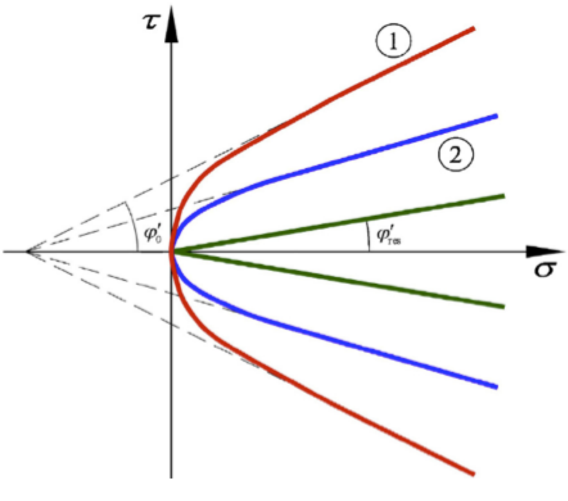

Figure 13: Shear strength (failure surface) evolution due to softening of strength parameters [1]

As mentioned, viscoplastic displacements only happen once the stress state reaches the elastic region boundary *F*, and can be calculated by means of a plastic potential *G* (or its derivative with respect to stress), a viscosity parameter and a function of the yield surface. With all this, the normal and shear viscoplastic displacement rates can be computed. From the **plastic potential surface** *G*, the displacements directions can be calculated. The derivative of *G* with respect to stress (i.e. $\partial G/\partial\sigma$) includes parameters so as to account for dilatant behaviour of joints under shearing.

As for the **hydraulic model**, the most relevant equations have already been mentioned in the section correponding to the theoretical approach of CODE_BRIGHT. However, it is important to note that some of the variables are conceptually different in this model since they have to be referred to the mid-plane. One of the most important parameters that has to be defined is the **intrinsic permeability of the joint**, which was actually already presented in Chapter 2 by means of the cubic law. Now, only one aspect remains to be noted and this is the relationship between hydraulic opening (which was called *b* in the previous chapter) and geometrical aperture (*a*) that has been considered so far in this model. In this case, the law proposed by *Barton et al. (1985)* is used. This law relates hydraulic opening to geometrical aperture by means of the joint roughness coefficient (JRC) and estimates that $e = a^2/JRC^{2.5}$ which can be directly substituted in the equation of intrinsic permeability. The other hydraulic constitutive equations and equilibrium laws considered in this model are Darcy's law, Fick's law, Fourier's law, retention curve and relative permeability function.

3.3.3. Embedded joints in finite elements

The basic idea of this particular approach consists in appropriately representing fractures embedded in continuous finite elements. The theoretical background concerning fractures in porous media have been presented in Chapter 2. Now, the main objective is to study how the existence of these fractures is taken into account within the finite elements of the mesh and how it affects them.

First, let's remember that a single fracture is characterised by its aperture *b*. Additionally, when a set of parallel fractures is considered, the separation *s* between joints is also a relevant parameter, as was depicted in detail in the previous chapter. Now, let's consider a finite element composed of a rock matrix (a porous media, in general) and a series of *n* parallel joints with a width *s* associated to each of them. The element size, mesured in the direction perpendicular to the set of discontinuities, is *l*. Thus, the number *n* of fractures in one of these elements depends on *s* and *l*, as shown in figure 14. In this type of fracture modelling, and since it is not convenient to use very thin elements, the element size becomes a limitation. In contrast to considering explicit joint interfaces (see 3.3.2), in this case homogenised properties are used and hence it is possible to mantain the finite element discretisation as well as the **continuous approach** to formulate coupled balance equations.

When a set of *n* fractures is embedded in a finite element, the equivalent intrinsic permeability (*k*) of the element in the direction parallel to the fractures can be calculated as follows: [8]

$$\mathrm{k} = \mathrm{k}_{\mathrm{matrix}}\left(\frac{\mathrm{l-nb}}{\mathrm{l}}\right) + \sum_{\mathrm{i=1}}^{\mathrm{n}}\left(\mathrm{k}_{\mathrm{fracture}}\ \frac{\mathrm{b}}{\mathrm{s}}\ \frac{\mathrm{s}}{\mathrm{l}}\right) = \mathrm{k}_{\mathrm{matrix}}\left(\frac{\mathrm{l-nb}}{\mathrm{l}}\right) + \sum_{\mathrm{i=1}}^{\mathrm{n}}\left(\mathrm{k}_{\mathrm{fracture}}\ \frac{\mathrm{b}}{\mathrm{s}}\ \frac{1}{\mathrm{n}}\right)$$

$$\mathrm{k} \cong \mathrm{k}_{\mathrm{matrix}} + \frac{1}{\mathrm{s}}\ \mathrm{k}_{\mathrm{fracture}} = \mathrm{k}_{\mathrm{matrix}} + \frac{\mathrm{b}^3}{12\ \mathrm{s}} \tag{31}$$

This expression is equivalent to that obtained from a more theoretical approach in Chapter 2. Note that permeability of the element does not depend on the size *l* of the element but on the width associated to each fracture (or separation between parallel joints) *s*.

All in all, the **permeability of the element** in the direction parallel to the fracture depends on the permeability of the matrix k_{matrix} and the permeability due to the existence of joints (which is, in fact, the only relevant one unless fractures have very low apertures). As for the the direction perpendicular to the joints, in this case it is set equal to the matrix permeability.

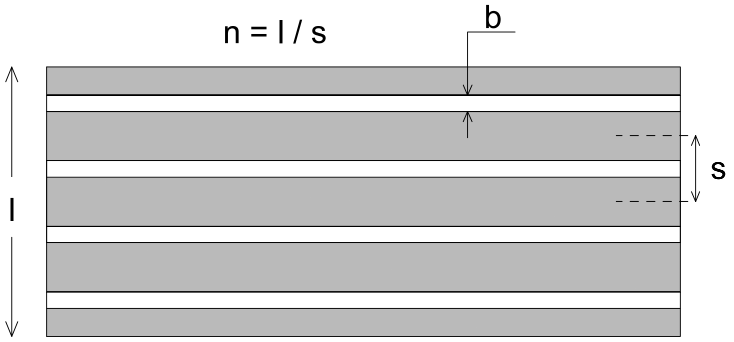

Figure 14: Scheme depicting a series of *n* parallel fractures along a length *l*, separated by a distance *s* and with an aperture equal to *b*.

In Chapter 2 some aspects concerning discontinuity planes were discussed. Additionally, expressions accounting for rotation matrices and how they affected permeability depending on orientation were presented. Nevertheless, to apply this theory to the embedded joints approach it is not necessary to know the fracture orientation, and it is not necessary to work with the corresponding tensorial magnitudes either. In the simplest case, if conditions for fracture development are met at some particular position (i.e in some elements of the finite element mesh), the change in aperture is calculated and the new permeability is computed using (31). Then, the overall permeability of this particular element is changed in an isotropic way, to such an extent that preferential flow paths (composed of a set of elements with increased permeability) may be created. Despite isotropic changes of permeability within the elements, the development of **preferential paths** leads to an induced flow anisotropy and heterogeneity.

Joint opening is controlled by the stress and strain states, and this is indeed where the hydro-mechanical coupling plays the most relevant role. The aperture of the fracture can be estimated from deformation as follows:

$$\begin{aligned} &\mathrm{b} = \mathrm{b}_0 + \Delta\mathrm{b} && \text{for} \quad \Delta\mathrm{b} \geq 0 \\ &\Delta\mathrm{b} = \mathrm{s}\Delta\varepsilon = \mathrm{s}(\varepsilon - \varepsilon_0) = (\mathrm{l}/\mathrm{n})(\varepsilon - \varepsilon_0) && \text{for} \quad \varepsilon > \varepsilon_0 \end{aligned} \qquad (32)$$

where b_0 is the initial aperture and Δb its variation, calculated from the associated width *s* and the localised deformation ε. Note that a threshold ε_0 has been included in the formulation so that the aperture changes start only once deformation has reached this value. If the fracture already exists and has an initial aperture b_0, this threshold is set to zero, which means that opening will take place as soon as deformation starts to increase. Note that in this case, the initial aperture can be zero too, which is an indication that fractures already exist, but they are closed. All in all, the threshold value ε_0 defines the initiation of fracture aperture, from which two cases can be established: [8]

- **Existing fracture**, where $\varepsilon_0 \approx 0$ (initially closed) or $\varepsilon_0 < 0$ (initially open) and the tensile strength is $\sigma_t = 0$ because the discontinuity already exists. In any case, normal extension leads to aperture opening from the beginning of stressing. Fracture closure would take place with unloading, but a residual aperture is expected in a general case, accounting for irreversible deformations associated to elasto-plasticity. Using (32) residual aperture b_r can be computed from residual deformation ε_r (see figure 15).

- **Non-existing fracture**, where $\varepsilon_0 \neq 0$ (it is, in fact, equal to the failure strain ε_1) and $\sigma_t \neq 0$, which means that a tensile strength exists in this case. The relationship between tensile strength and failure strain is given by the constitutive equation used to compute the stress-strain behaviour.

As mentioned, the type of constitutive law chosen to describe the material behaviour (in other words, the stress-strain behaviour of the matrix) is crucial to compute aperture changes. Indeed, this is where the relationship between the stress path followed and the existing deformation comes from. If an elastic model is considered for the matrix, fracture aperture may be associated with tensile sresses. On the other hand, if an elasto-plastic behaviour is considered, dilatancy associated to shear stresses also plays an important role. If (32) is introduced in (31) the following expression for computing the permeability of the element is obtained:

$$\mathrm{k} = \mathrm{k_{matrix}} + \frac{[\mathrm{b_0} + \Delta \mathrm{b}]^3}{12\ \mathrm{s}} = \mathrm{k_{matrix}} + \frac{[\mathrm{b_0} + \mathrm{s}(\varepsilon - \varepsilon_0)]^3}{12\ \mathrm{s}} \qquad (33)$$

The element permeability depends on the fracture spacing *s* but not on the element size. In other words, in this approach permeability is affected by a characteristic parameter of the material such as *s* but is independent of the meshing parameters, which is obviously something necessary to guarantee the consistency of the method. In general, it is interesting to consider one or more fractures in each element (i.e $l \geq s$), hence some of the elements will develop higher permeability due to opening of fractures contained in them while others will keep the properties of the matrix. If this condition is not accomplished (i.e less than one fracture in each element) a single fracture would be homogenised into various elements leading to an unsuitable smoothing of the preferential flow paths.

Having computed the permeability changes in each element, then the fluid flux (carbon dioxide, in the context of CCS) and flow rate can be calculated using the theoretical expressions presented in Chapter 2. The flow rates are obtained after application of the finite element approach. Neglecting the effect of the matrix permeability in the direction of the fracture (as compared with the effect of the cubic law), the flow rate in that direction depends on the number of fractures (*n=l/s*) and their aperture (*b*). It is important to note that, apart from affecting permeability, joint opening also has an important effect on other hydraulic properties, as seen in the previous chapter.

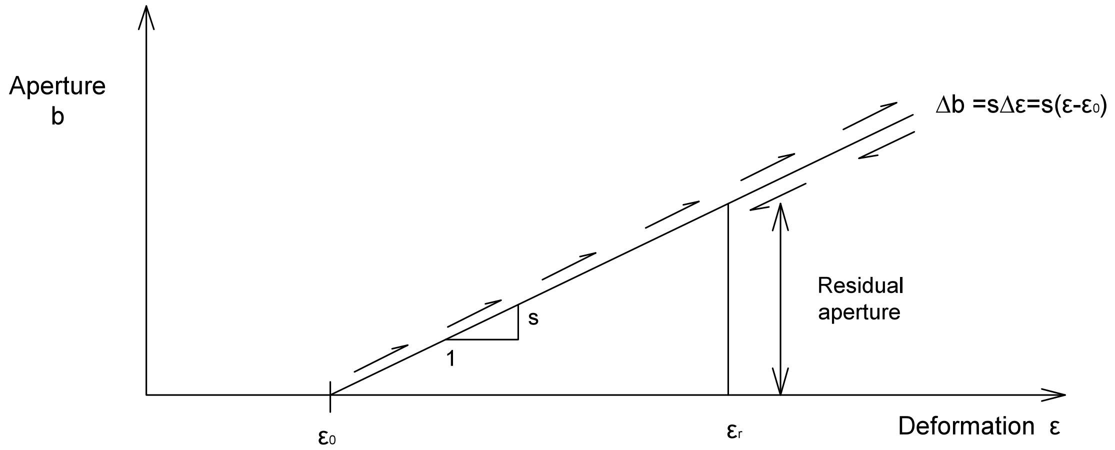

Figure 15: Graph schematically depicting how joint aperture evolves with deformation. Note the existence of an irreversible deformation and, thus, the presence of a residual aperture.

3.3.4. Presence of "strong discontinuities": overview

One of the most complex approaches to simulate rock damage consists on the embedment of real discontinuities in finite elements. This means that fractures are not only considered for computing changes within the elements, but a discontinuity path is in fact placed inside of them, irrespective of the size and specific orientation. Thus, a discontinuity tracing a domain divides several finite elements as seen in figure 16.

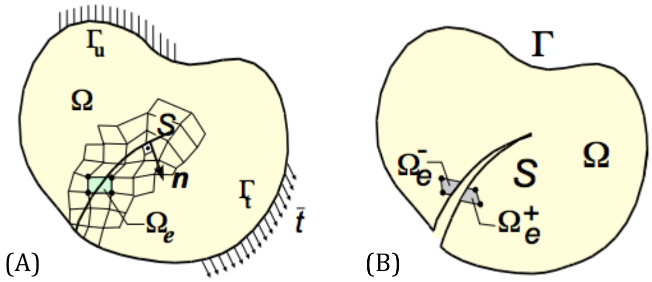

Figure 16: Discontinuity path placed inside the elements (Oliver et al., 1999)
(A) Discontinuity tracing in a domain.
(B) Finite element divided by discontinuity. [9]

This approach involves a whole theory based on the introduction of strong discontinuity kinematics in order to derive discrete constitutive models from the more known and common constitutive original ones. This theory has been developed by *Oliver, J.* and thoroughly explained in *On the discrete constitutive models induced by strong discontinuity kinematics and continuum constitutive equations* (2000). The main idea is to consider jumps in the displacement field across the discontinuity interface, which induces projected discrete constitutive models (traction-displacement jumps) in a consistent manner and provides possible links between classical continuum strain-localisation analysis and the non-linear fracture mechanics techniques. [9] Oliver concluded that by reguling the continuum softening parameter in a band around the discontinuity, continuum models could be adapted so as to simulate the presence of strong discontinuities. In fact, not only a discrete constitutive equation but a complete model could be derived from the continuum one. The fact that the parent continuum model behaves as the induced discrete one would do in a discrete formalism offers a complete set of advantages and possibilities for simulation purposes (Oliver, 1996; Oliver et al. 1999).

The implementation of this strong discontinuities theory is still in development at the Universidade Federal de Pernambuco (Brazil), but part of it is already available in some versions of CODE_BRIGHT. and can be applied to 2D problems with fractures that propagate due to tensile failure. One of the most interesting aspects of the whole development is the insertion of interface finite elements throughout a mesh or in the most requested area. These elements, which have high aspect ratio (figure 17) and are based on strong discontinuity kinematics (Manzoli et al., 2012), can be opened by a preferential path, forming a fracture and thus relaxing the stress in the other elements.

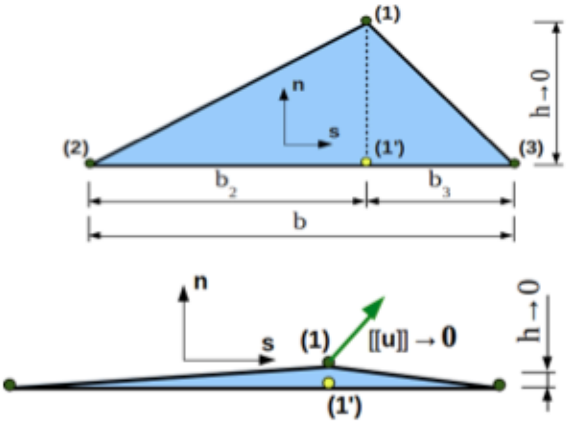

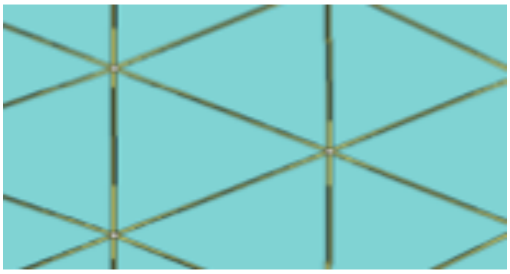

Figure 17: Scheme depicting the concept of finite element with high aspect ratio (left) and interface elements inserted within the mesh.

CHAPTER 4

PRESENTATION OF A REAL CASE: INJECTION AT IN SALAH

4.1. Main interest

The In Salah (Algeria) CO_2 storage project is an extremely interesting case to understand not only how a project of this size is undertaken but also how geomechanics may play a key role in explaining the observed behaviour of a geological storage site. The main interest of this case is the unusual double-lobe uplift detected on ground surface after months of intense monitoring. Being able to model this uplift pattern is paramount so as to understand the geomechanics associated to it as well as the reasons that have caused such deformational behaviour.

The aim of this fourth chapter is to briefly describe the project in question and then present a simplified version of a 2D model developed in CODE_BRIGHT. While it is aknowledged that a 2D model cannot simulate this complex case in the most accurate way, the simulation of a single cross-section of the real 3D storage site is enough to reproduce the aforementioned uplift patterns and the reasons that causes them.

4.2. Description

4.2.1. The In Salah injection project

The Krechba gas field at In Salah (Algeria) is the site of the first industrial scale on-shore CO_2 storage demonstration project (a joint venture among BP, Sonatrach and Statoil). Injection started in 2004 and, although no leakage of CO_2 was reported during the lifetime of the project (this is, an injection of 3.8 MT of CO_2 in total), it was suspended in 2011 due to concerns about the integrity of the seal. It has been estimated that the formation has a total storage capacity of 17 million tons and an expected operational life of 20 years. Apart from its size and importance, this is also a relevant project because the succesful storage of carbon dioxide in the Krechba formation gives valuable insight into how CO_2 can be stored in analogous carboniferous sandstone wells which are common in China and Northwest Europe. In Salah has been recognised by the Carbon Sequestration Leadership Forum as one of the most important CCS initiatives in the world. [6]

***Figure 18**: Natural Gas production at In Salah (Algeria)*

The Krechba saline formation is a depleted gas reservoir formed by a Carboniferous sandstone unit and located at a depth of 1.9 km. Gas processing from In Salah Oil Field serves as CO_2 source. Since the natural gas contains small amounts of carbon dioxide, it is necessary to separate the pure gas from the CO_2 so as to meet purity standards for sale. To avoid increasing the amount of CO_2 being sent to the atmosphere, it was decided to invest $100 million (an approximate cost of 6 dollars per ton of injected carbon dioxide) to store it geologically in the aforementioned Krechba site. [6]

Due to the relatively low level of rock permeability in the Krechba storage well (compared, for instance, to oil reservoir rocks) the injection has been undertaken via three long-reach (more than 1 km) horizontal wells. These wells (KB-501, KB-502 and KB-503, see figure 19) were drilled using geosteering technologies to mantain them within the formation and perpendicular to the maximum stress direction (i.e. the dominant fracture orientation) and so maximise the injection capacity. In the process of drilling a borehole, geosteering is the act of adjusting the borehole position (this is, inclination and azimut angles) in light of the geological information gathered while drilling. Approximately 75 % of the CO_2 has been injected into the two northern wells.

One of the most relevant innovations of this project is the close monitoring of the storage site, which has been carried out using a great variety of techniques, including geochemical, geophysical, 3D and 4D seismic and satellite technologies. By so doing, areas such as overall plume migration, well and caprock integrity, surface movement and pressure development over time have been assessed. This close observation is essential to ensuring secure CO_2 storage in the long-term and provides information on how the fluid migrates in the formation. The most relevant monitoring technologies which have been used are:

- Satellite imaging, for identifying ground movement over days, months and years.
- Well monitoring, to measure the migration and movement of the injected fluid.
- Microseismic monitoring, a listening technique that detects very small movements in rock structures such as the "creak" due to changes in temperature and pressure.
- Seismic monitoring, which uses sound waves generated from near the surface of the arth and listens for the reflected signals that are used to create a detailed "picture" of the subsurface.

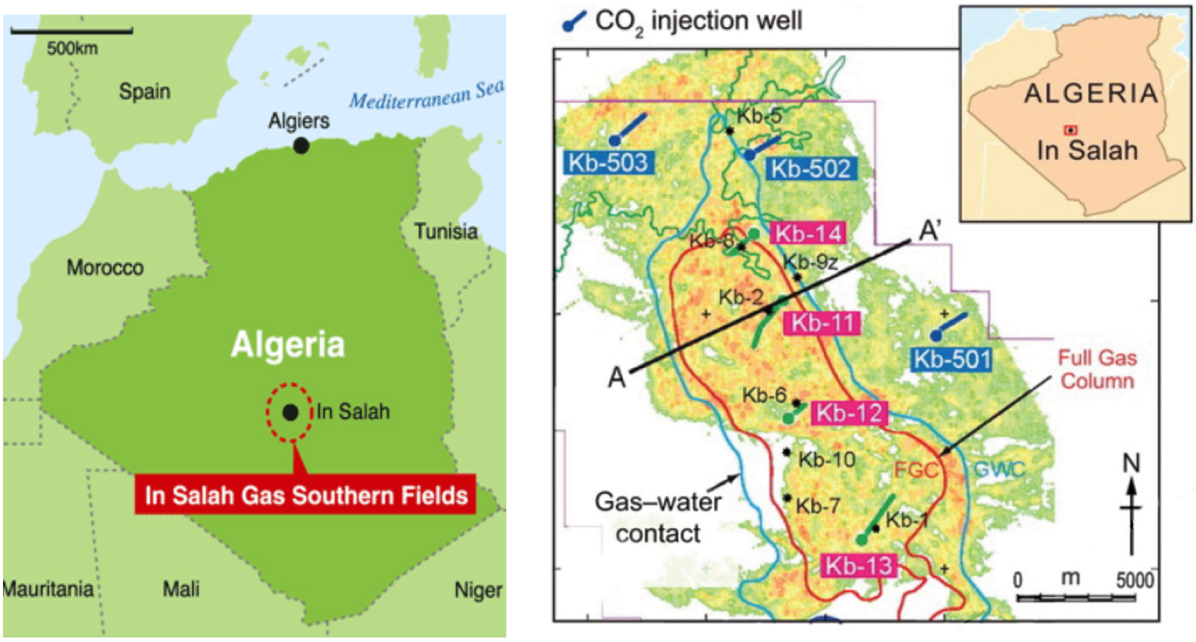

Figure 19: Location of the Krechba formation and the three injection wells (blue), as well as the natural gas extraction wells (green). AA' represents the seismic line (see 4.2.2) [6] [10]

The pioneering use of satellite InSAR (Interferometric Synthetic Aperture Radar) has allowed to detect and monitor subtle changes in surface deformation due to fluid injection. The implementation of this satellite technology is very new and has provided the most (or one of the most) valuable results of the programme. [6] Additionally, time-lapse seismic and micro-seismic studies have also provided valuable information concerning formation response to injection, even if the vast amount of data have taken many months to interpret. While 3D processing can be used to provide an image of the positions of the rock formations, 4D processing is used to detect differences in the signals caused by changes in fluids between one survey and the next. Consequently, monitoring data has allowed to update and refine the geological, geomechanical and flow dynamical models of the storage complex. [10]

The decision of suspending CO_2 injection in June 2011 was taken after analysis of seismic and geomechanical data from 2010 due to concerns about possible vertical leakage into the caprock. Nevertheless, the comprehensive site monitoring continues with an intensified research and development programme so as to plan the future injection strategy.

4.2.2. Storage site: geomechanical aspects

4.2.2.1. The Krechba saline formation and its lithology

As mentioned, carbon dioxide injection is performed into the aquifer leg of a 20-metre thick water-filled Carboniferous sandstone reservoir (with a relatively low permeability) from which the Krechba field produces CO_2 rich gas. The fluid is injected at a depth between 1850 and 1950 m. This reservoir has porosities ranging from 10% to 18% and permeabilities around $10^{-14}\ m^2$. As any typical storage site, the reservoir is sealed by much less permeable layers that make up the so-called caprock. In this case, the injection reservoir is sealed by around 950 m of a mixed sequence of Carboniferous mudstones. These are unconformably overlain by approximately 900 m of a mixed Cretacious of sandstones and minor mudstones, a sequence that comprises the regional Pan Saharan potable aquifer. [6] Hence, it is extremely important to avoid any type of leakage from the injection reservoir.

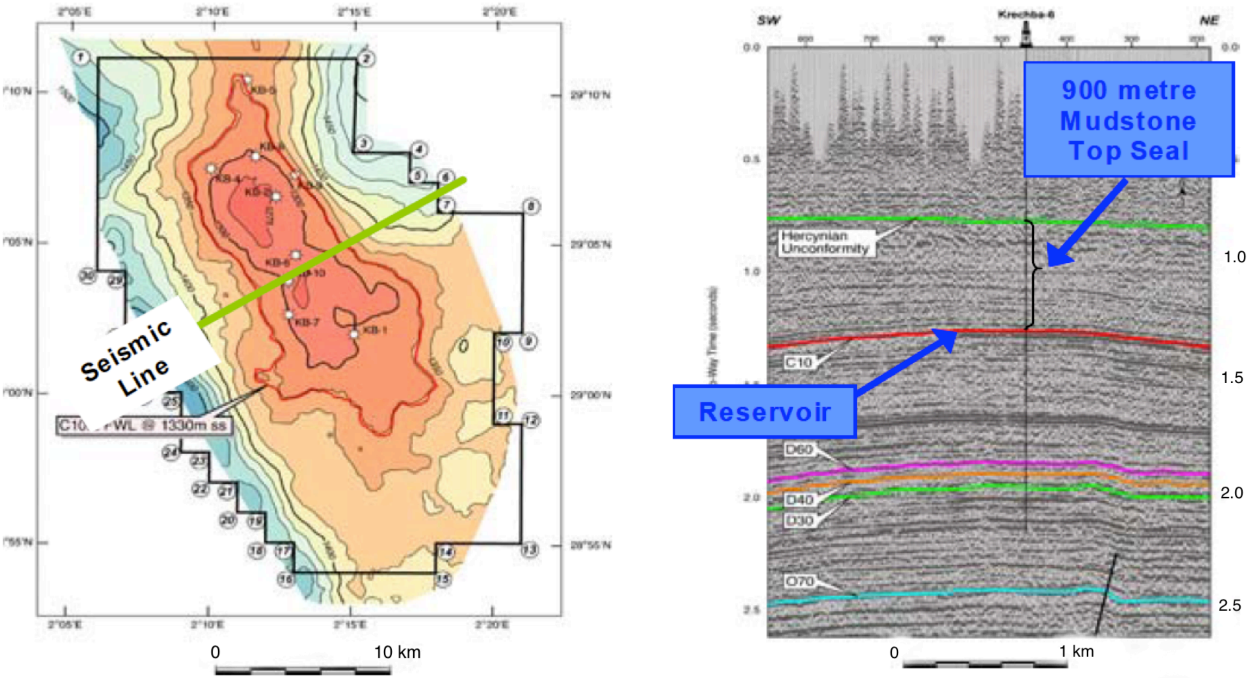

Figure 20: Krebcha structural map and 1997 3D seismic survey. [6]

In spite of being notably thin, it is important to mention the existence of an impermeable anhydrite at the top of the Hercynian unconformity, some 3 m thick, that divides the Corboniferous from the Cretaceous over the whole region as a final top seal. Finally, surface outcrop consists mostly of Cretaceous muddy carbonates.

4.2.2.2. InSAR-detected ground uplift at KB-502 injection well

The existence of heterogeneities such as the aforementioned fractured area may affect the observed ground movement. The presence of minor faults may affect the pore-pressure and plume distribution, as well as causing changes in permeability distribution due to fracture reactivation within the injection zone. All this turned out to be much more relevant once the pattern of deformation observed through satellite based measurements at KB-502 injection well was analysed.

In any type of geological carbon storage project, one expects a certain degree of ground surface deformation, which normally consists in an uplift close to the injection point that turns into almost unnoticeable deformation far from the zone in question. In this case, however, a double-lobe pattern of deformation has been observed even since the first years of injection. The rate of distance change above injection wells KB-501, KB-502 and KB-503 has been as high as 5 mm/year and, additionally, a small subsidence has been observed in the gas field (this is, between all three wells) and associated with production-induced pressure depletion. Nevertheless, the uplift pattern, which (as mentioned) features two parallel uplift lobes rather than one single lobe, is still the most interesting aspect of this case, and all indicates that it cannot be explained by the overpressure effect only but with a series of heterogeneities present in the Krebcha formation.

It is indeed the opening or reactivation of a fault zone due to an increase in the bottomhole pressure that can produce such a pattern. More precisely, both semi-analytical inverse deformation analysis (*Vasco et al., 2010; Rucci et al., 2012*) and coupled numerical modelling of fluid flow and geomechanics (*Rutqvist et al., 2011*) have shown that this behaviour can be explained by injection-induced deformation in a deep vertical fracture zone or fault intersecting the injection well and extending a few hundred metres up to a depth of 1600 m (*Rutqvist et al., 2012)*. [10] The existence of such a fracture zone was already suggested by initial seismic data and have been confirmed by more recent surveys (*Gibson-Poole and Raikes, 2010; Wright, 2011*). When analysing the injection data, *Bissell at al. (2011)* found an abrupt increase in the injectivity once the estimated bottomhole pressure reached a certain value, which indicates a sudden fracture opening or (tensile) reactivation of a pre-existing fault.

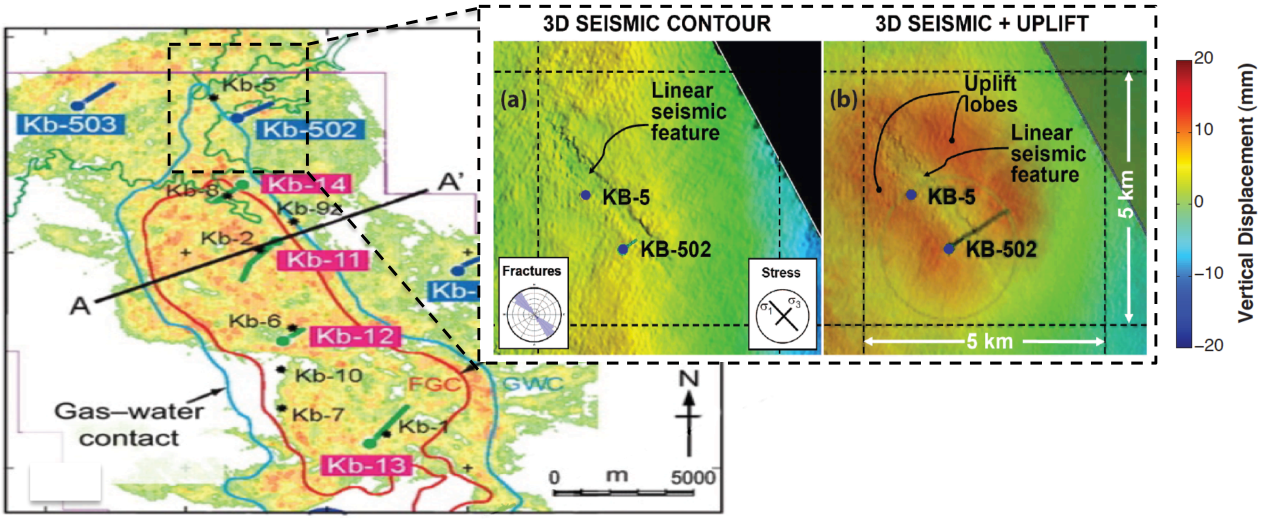

Figure 21: 3D seismic contour and map of uplifts observed around the KB-502 injection well. [10]

Since the beginning of the injection at KB-502, the following facts associated to ground surface movements have been observed:

- April 2005: injection at KB-502 well started.
- April to September 2005: ground uplift of less than 5 mm during this period of time.
- September 2005: the injection pressure increased sharply.
- January/February 2006: the fracture zone was possibly activated, with the ground uplift reaching a value of 10 mm and showing the double lobe pattern for the first time.
- December 2006: the ground uplift reached a displacement of around 15 mm.
- Mid-2007: the KB-502 well was shut, but almost 20 mm of ground uplift remained after one year. Then, although at a much lower rate, a small subsidence phase occurred.

4.3. 2D Simulation of the KB-502 ground uplift

4.3.1. Overview of previous studies

Rutqvist et. al (2010, 2012) carried out numerical simulations of this case using the TOUGH-FLAC/ECO2N simulator for coupled deformation and fluid flow. The modelled domain was centered in the KB-502 injection well, which is the most interesting of all at least from the double lobe uplift pattern perspective. All material data were obtained according to the Krechba field lithology (see 4.2.2.1 and 4.3.2). Hydraulic properties were chosen considering both numerical results (*Rutqvist et al., 2010; Shi et al., 2012*) and *in situ* observation (*Iding and Ringrose, 2010*), while mechanical properties were based on Statoil log analysis (*Gemmer et al., 2012*). Parameters for capillary and relative permeability were taken from former numerical modelling studies of CO_2 injection in a deep saline aquifer (*Zhou et al., 2008; Pruess et al., 2001*). [10] All in all, a linear poroelastic medium was simulated, and so no failure processes were considered. Initial conditions, as well as initial stress, were derived from site investigations and regional data.

The existence of a fracture zone was modelled considering a change in both mechanical and hydraulic properties after the fifth month of injection. Thus, the simulation was composed of an initial period of 5 months with intact layers and then a second period in which an abrupt change in mechanical and hydraulic properties occurs so as to explain the double-lobe uplift pattern. The vertical fracture zone was simulated as a highly permeable and anysotropic zone, 80 m wide and extending 350 m above the injection zone and 3500 m long in the NW-SE direction. This includes a series of three 20 m wide zones, separated from each other by 10 m of intact rock (see figure 22). The intact rock zones were included so as to achieve more precise results and avoid unrealistic displacements at some numerical nodes which would affect the ground surface uplift. [10]

Nevertheless, recent studies and analysis (*Morris et al., 2011* ; *Davis, 2011*) concluded that it was difficult to constrain the height of the fracture zone. In other words, it was not clear that the fracture zone only affected part of the caprock layer and not the whole stratum or even some meters of the upper layers. This is indeed an important issue, since a very high fracture zone would allow carbon dioxide to reach and pollute the upper aquifer, which is one of the reason for which it was decided to stop fluid injection in 2011. From the ground uplift perspective, though, *Rutqvist et al. (2010, 2012)* concluded that considering the aforementioned height of 350 m above the reservoir led to the most accurate numerical results when compared to InSAR data. Additionally, they are consistent with current interpretations of the 2009 3D seismic survey.

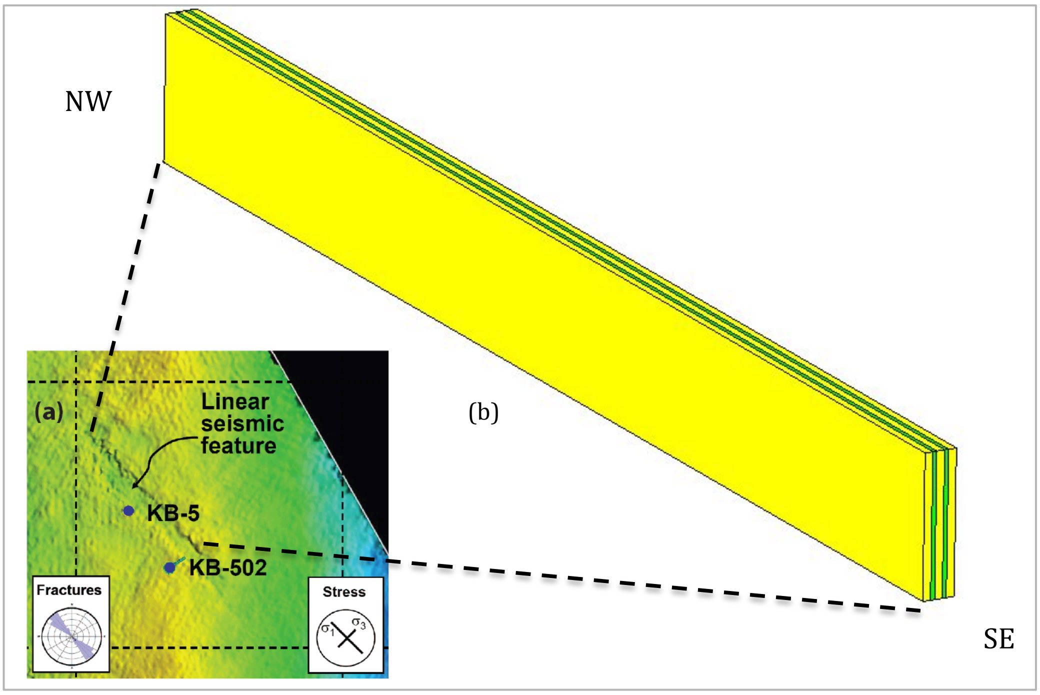

Figure 22: (a) View of the location of the feature with respect to the injection well ; (b) Simplified geometry of the fracture zone that intersects the caprock overlying the KB-502 injection reservoir.

As a summary of this simulations, the following point should be mentioned:

- Latest studies by *Rutqvist et al.* focused on the double-lobe uplift pattern observed in ground surface and its relationship with the existence of a vertical fractured zone.
- Fracture opening/reactivation was simulated by an abrupt decrease in the fault zone Young's modulus and a sudden increase in permeability, homogeneous for the whole reservoir.
- Uplift results were, in general, consistent with real data. The double lobe shape was present in the numerical simulations despite some small differences.
- The differences were more notable after shut-in occured and also far from the injection well. This can be explained, respectively, by the assumption of elasticity and also by the fact that permeability had been changed abruptly and homogeneously.
- The authors mention the necessity of considering fracture propagation and stress-dependent permeability for a more accurate modelling.

4.3.2. Model set-up

In an attemp to avoid providing too much data that would difficult the reading of this text, only some relevant aspects regarding the modelled geometry is included here. More information (material properties, boundary conditions, initial conditions and finite element mesh formation) can be seen in Appendix C.

From a geometrical point of view, the modeling of the region around the KB-502 injection well presented here is based on the 3D model described by *Rutqvist et al. (2012)*. So as to simplify the simulation, and because the objective here is essentially academic since an exhaustive analysis would require much more data and high computational cost, only a cross-section of the problem has been modelled. Obviously, a section including both the fracture zone and the horizontal injection well has to be chosen if one wants to model the effect of fluid injection on the geological media.

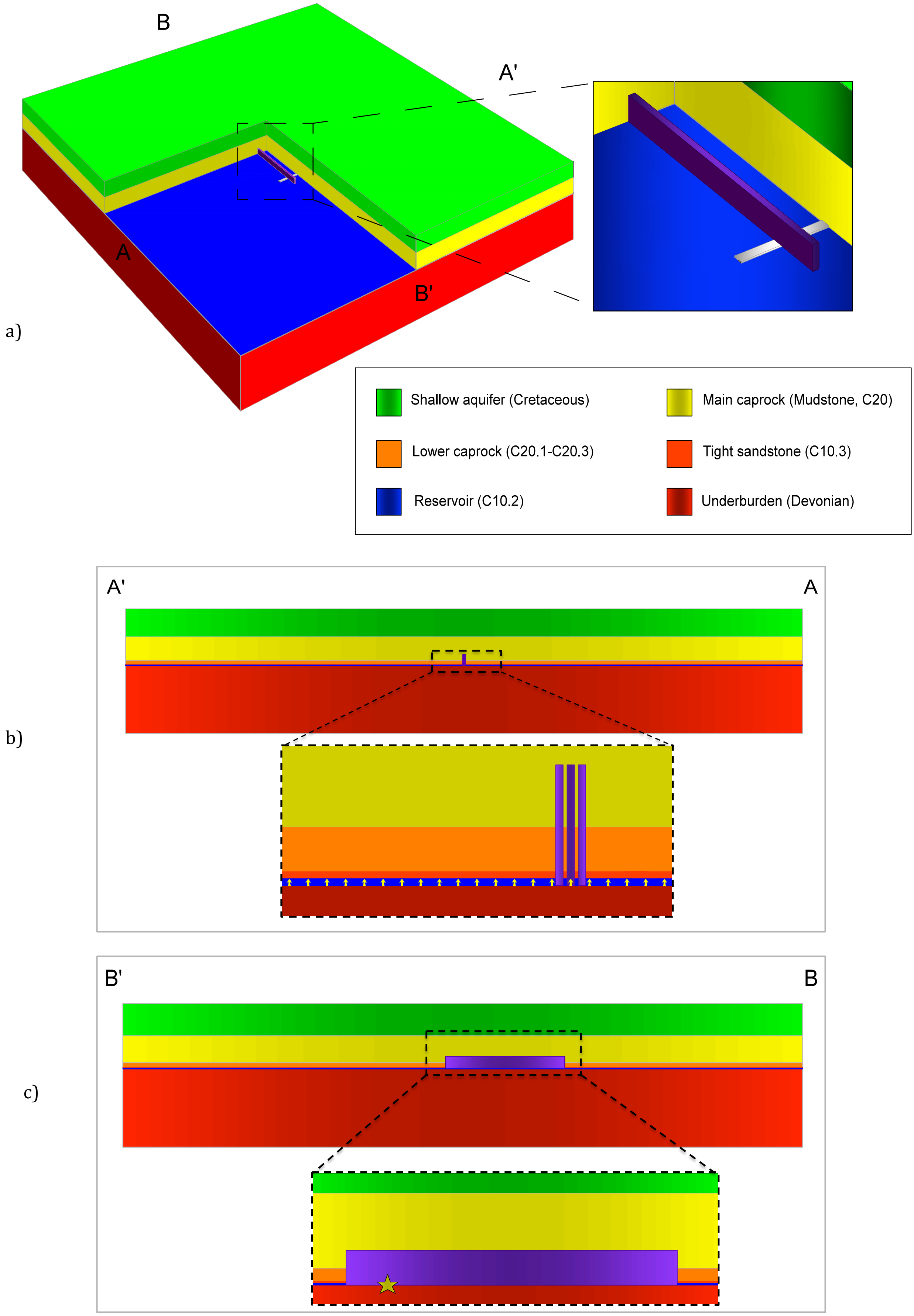

Figure 23: Geometry of the multilayer system modeled to simulate the injection of CO_2 (based on Rutqvist et al., 2013)

From the already simplified 3D domain (see figure 23.a), two relevant sections AA' and BB' could be extrapolated (figure 23.b and 23.c). Nevertheless, section AA' (perpendicular to the fault plane) is the most interesting from the perspective of ground deformation, as well as being more likely to be accurately modelled assuming plane strain. As a consequence of all this, only section AA' is going to be modeled, although some ideas regarding the fault direction are going to be commented afterwards. As in can be seen, the fault zone has been modelled according to the three-layer scheme mentioned in 4.3.1, although the embedded joints approach has been used instead of a sudden permeability increase (see Appendix C).

Table 4 lists all different layers, their depth within the geological formation and their thickness. Height, thickness and length for the fault zone and the KB-502 horizontal injection well have also been included. Dimensions are referred to as *vertical*, *NW-SE* (fault direction) and *NE-SW* (direction normal to the fault). It is important to note that all different caprock layers have been depicted as only one in the general 3D scheme. Otherwise, due to the dimension of the problem and the fact that some layers are relatively thin, they would be difficult to see.

Geological strata			
Layer		depth (m)	thickness (m)
Shallow aquifer (Cretaceous)		0-900	900
Caprock	Main caprock (Mudstone, C20)	900-1650	750
	Lower caprock (C20.1-C20.3)	1650-1780	130
	Tight sandstone (C10.3)	1780-1800	20
Reservoir (C10.2)		1800-1820	20
Underburden (Devonian)		>1820	-
Fractured zone dimension (m)			
NW-SE direction ("length" of the fault zone)		3500	
NE-SW direction ("thickness" of the fault zone)		80	
Vertical drection ("height" of the fault zone)		variable (350 m, 920 m, 1600 m)	
Horizontal injection well dimension (m)			
NE-SW direction ("length" of the horizontal well)		1000	
NW-SE ("thickness" of the horizontal well)		100	

Table 4: List of different layers that make up the Krechba formation, different thicknesses and dimension of the injection well.

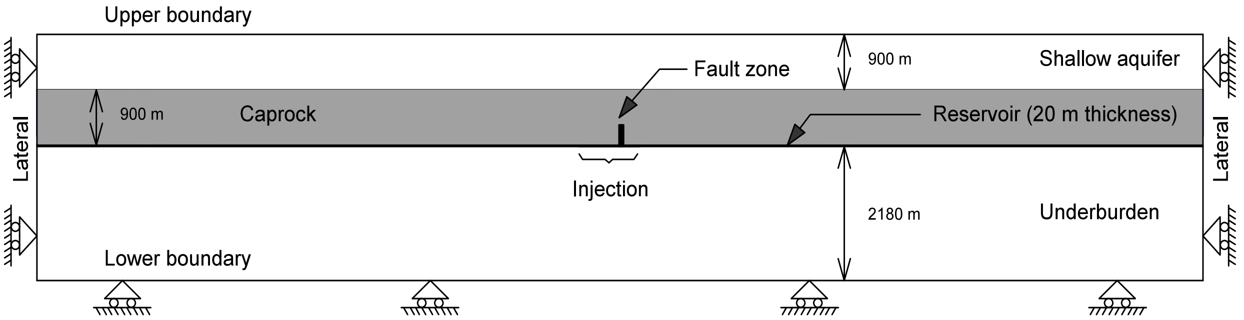

Figures 24: Simplified scheme depicting the modelled 2D domain. See Appendix 3 for a detailed list of material properties and boundary and initital conditions.

4.3.3. Simulated uplifts: presentation and discussion of results

Vertical displacement, but also fluid pressure due to its big effect on the former, are the two most interesting variables to analyse in this case. Additionally, some comments regarding horizontal displacements around the fracture zone are going to be made. The effect of fluid injection on other variables is not going to be presented here, but a thorough analysis of how CO_2 storage can alter a typical injection site is presented in the following chapter by simulating a more general case.

First of all, surface uplift patterns have been compared assuming two different scenarios: one with no presence of a fracture zone and another with a 1600 meter-high vertical feature which allows the injected fluid to migrate. This has been done in an attemp to see how the existence of such damage in the caprocks is responsible for the observed deformational behaviour. As expected, the non-existence of a fracture zone leads to a typical one-lobe pattern of displacement, as seen is figure 25.a (after around 2 years of injection). Indeed, the colour map shows the tendency of the medium to deform more in the surroundings of the horizontal injection well, following an almost symmetrical uplift pattern. The effect is clearly felt at surface level, but does not match any of the double-lobe pattern detected by InSAR.

The assumption of a potentially highly-conductive vertical feature, though, allows for a better matching between simulated vertical displacement pattern and observed real behaviour. Figure 25.b shows a clear tendency of the geological medium to deform in a different way than that observed in 25.a (same time step). Vertical displacements are accentuated at both sides of the vertical feature, an effect that can be felt several meters above the injection zone. Even though the colour map already shows this tendency, a contour line map of the fracture zone and its surroundings has been included for a better visualisation.

Displacements are bigger at the NE side (i.e. left-hand side of figure 25.b) and, thus, the uplift pattern is not symetrical, although it is clear that the vertical zone has an effect on where the low point of the double-lobe uplift is located. Actually, it is plausible to assume that the reason why the vertical feature does not act as a symmetry axis (in 2D) is that it does not intersect the horizontal injection well at its midpoint. Consequently, injection is not symmetric with respect to the vertical feature, and neither is the uplift. This behaviour is closely related to the effect of pressure build-up in the reservoir and the fact that it increases more in one side than the other. In other words, when the vertical path is opened, the pressure of the CO_2 that has been accumulating in the SW side can be more easily dissipated for it is closer to the fracture to.

Apart from pressure build-up, the other reason that explains this double-lobe pattern when a highly-conductive vertical path is opened is the tendency of this zone to expand laterally when fluid penetrates it. The observation of figure 25.b and 25.c allows to understand how horizontal and vertical displacement are related to each other. After 2 years of injection, fluid penetration in the fracture zone has caused it to expand several millimetres to both sides (NE-SW direction), as seen in 25.c. At the same time, the media has experienced vertical displacements but, to make these compatible with the horizontal ones, the aforementioned particular pattern has appeared. This lateral expantion is not the only reason for this behaviour of the storage site, but it seems to be a key factor in the formation of the double-lobe uplift.

While it seems obvious that the existence of a fracture zone is the main responsible for the double-lobe pattern, establishing its height with precision is a difficult task. A more complex model would be required to match the simulated values with the real ones. Notwithstanding, the present model is useful to compare how different heights of the fracture zone affect surface uplifts under the same injection conditions.

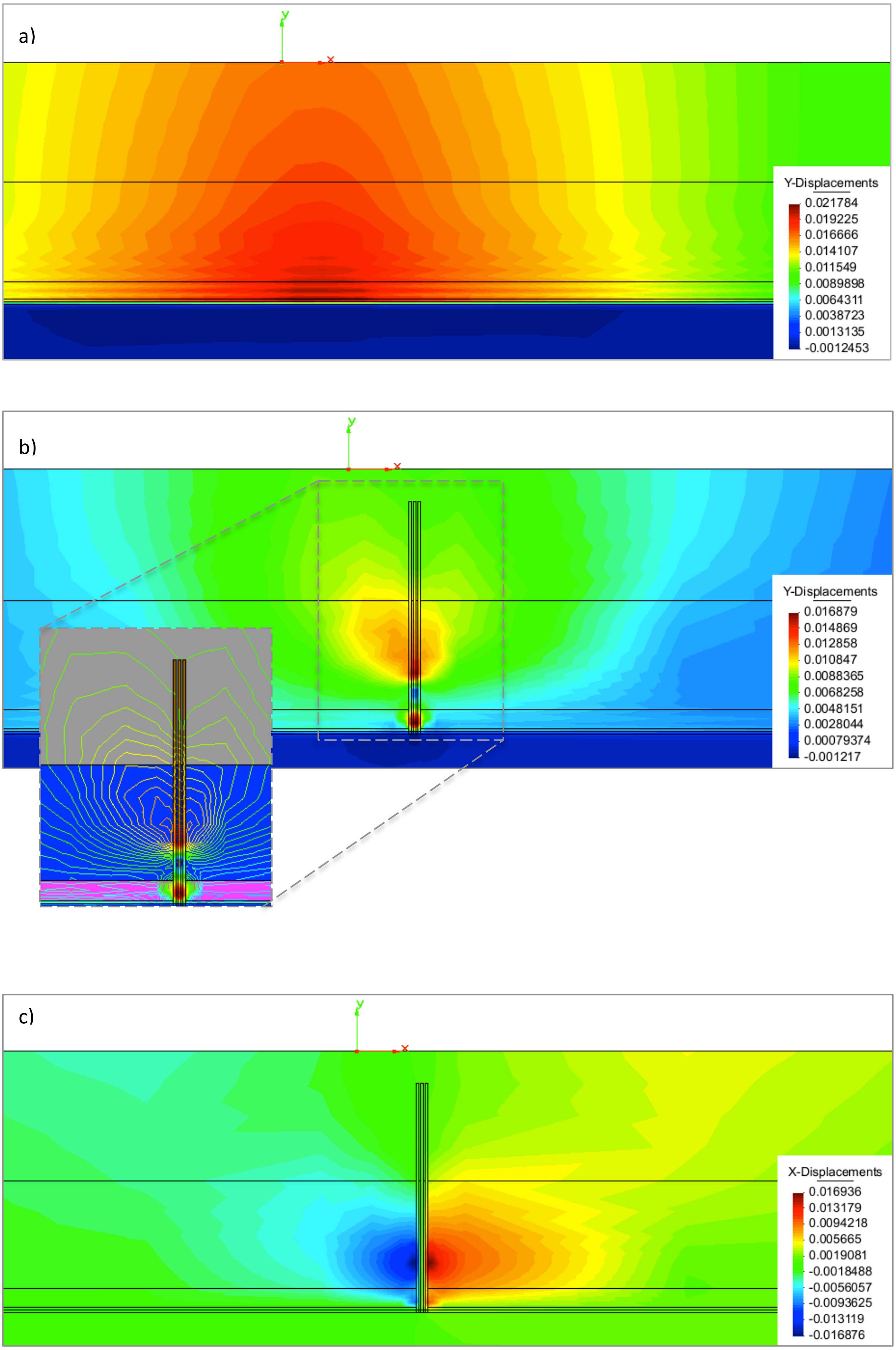

Figures 25: Displacement (in metres) after 800 days of injection: a) vertical displacement without the existence of a fracture zone ; b) vertical displacement with fracture zone penetrating in the shallow aquifer (height 1600 m) ; c) horizontal displacement at both sides of the aforementioned fracture

Figure 26 shows a perfectly typical uplift pattern when no fracture zone is considered, with a maximum vertical displacement of almost 15 mm observed at x=250 m (which is the horizontal coordinate of the injection well midpoint) and distributed along the whole modelled domain. When vertical damaged areas are considered, though, the uplifts have a tendency to concentrate around the fracture zones due to the opening of a highly-conductive (and more deformable) path after 150 days of injection. In these cases, the effect of fracture opening on transient evolution of surface vertical uplift is clearly noticeable (see figure 27). As expected, after 150 days of injection the vertical uplift rate increases because the fluid is allowed to penetrate a much more deformable zone and also migrate through its fractures.

Different heights lead to a great variety of results. Generally, when the fracture zone reaches the shallow aquifer the observed vertical displacements are smaller, as depicted in figures 26 and 27 after having simulated fracture zones with heights of 350 m (confined in the caprock), as well as 920 m and 1600 m (both reaching the shallow aquifer). The fact that higher fracture zones lead to smaller uplifts can be explained by lower values of pressure build-up as a consequence of the opening of a big area which allows this pressure to dissipate faster than in the other cases. Indeed, as seen in 26, with heights of 920 m and 1600 m the uplift stabilises at a much early stage of injection, while it keeps increasing sustainedly in the other two scenarios. It is important to mention, though, that this sustained increase is also a consequence of having modelled this problem using a 2D geometry. Oherwise, fluid would be allowed to move through the fracture zone in the NW-SE direction (i.e the direction perpendicular to the simulated domain), and so a vertical uplift stabilisation would be expected as injection progresses.

As for CO_2 pressure evolution, figure 28 shows its evolution at a point located where the vertical feature intersects the reservoir (i.e. the inlet of the fracture zone). Note how the presence of the highly-conductive path makes pressure stabilise at some point or another. After an initial period in which pressure increases slowly, a change of tendency is observed once the vertical feature is reactivated. The transient evolution shows how the injected fluid penetrates the fracture zone (i.e passes through the inlet) and finally stops increasing, reaching lower values than those observed when the intact caprock assumption is made. Another interesting observation is that higher fracture zones lead to a more rapid increase in CO_2 pressure at the inlet. This happens because by connecting the injection reservoir to upper, more pervious strata, CO_2 is allowed to migrate more easily by effect of pressure gradient and buoyancy and, consequently, starts to penetrate the fracture zone at an earlier stage.

Finally, observation of the CO_2 pressure profile along the reservoir-caprock contact after 800 days of injection (figure 29) reveals the effect of the fracture zone on pressure build-up. Note how, indeed, pressure decreases in the surroundings of the vertical feature, following a pattern which is clearly connected to that of vertical displacement.

The values provided by InSAR images suggests that the fracture zone is confined in the caprock, with heights between 350 and 920 m, but probably closer to the first value. The assumption of higher fracture zones lead to uplifts values which are too small in comparison to those detected by the satellite. For confined fracture zones, though, surface uplifts of around 16 mm, with rates of 5 to 10 mm/year are obtained, which are closer to the real ones. Figure 30 shows the similarities between the simulated and InSAR detected uplift evolution tendencies. The fact that simulated values are higher than the real ones can be explained by the fact that the problem has been modelled as a 2D domain.

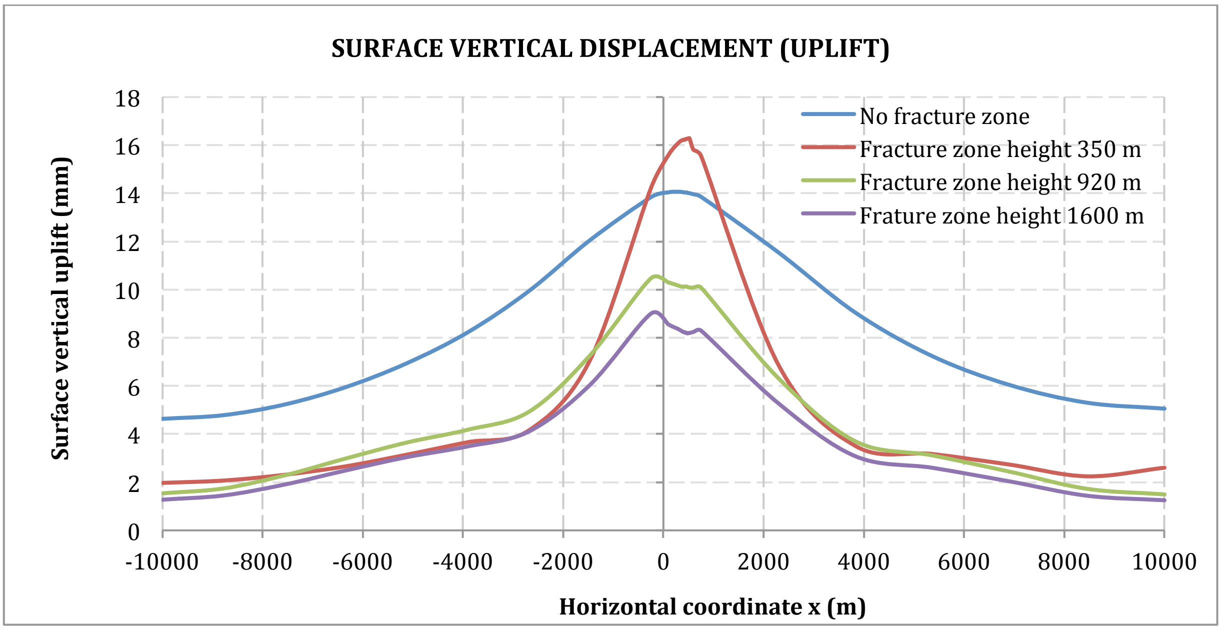

Figures 26: Surface uplift after 800 days of injection for different fault heights.

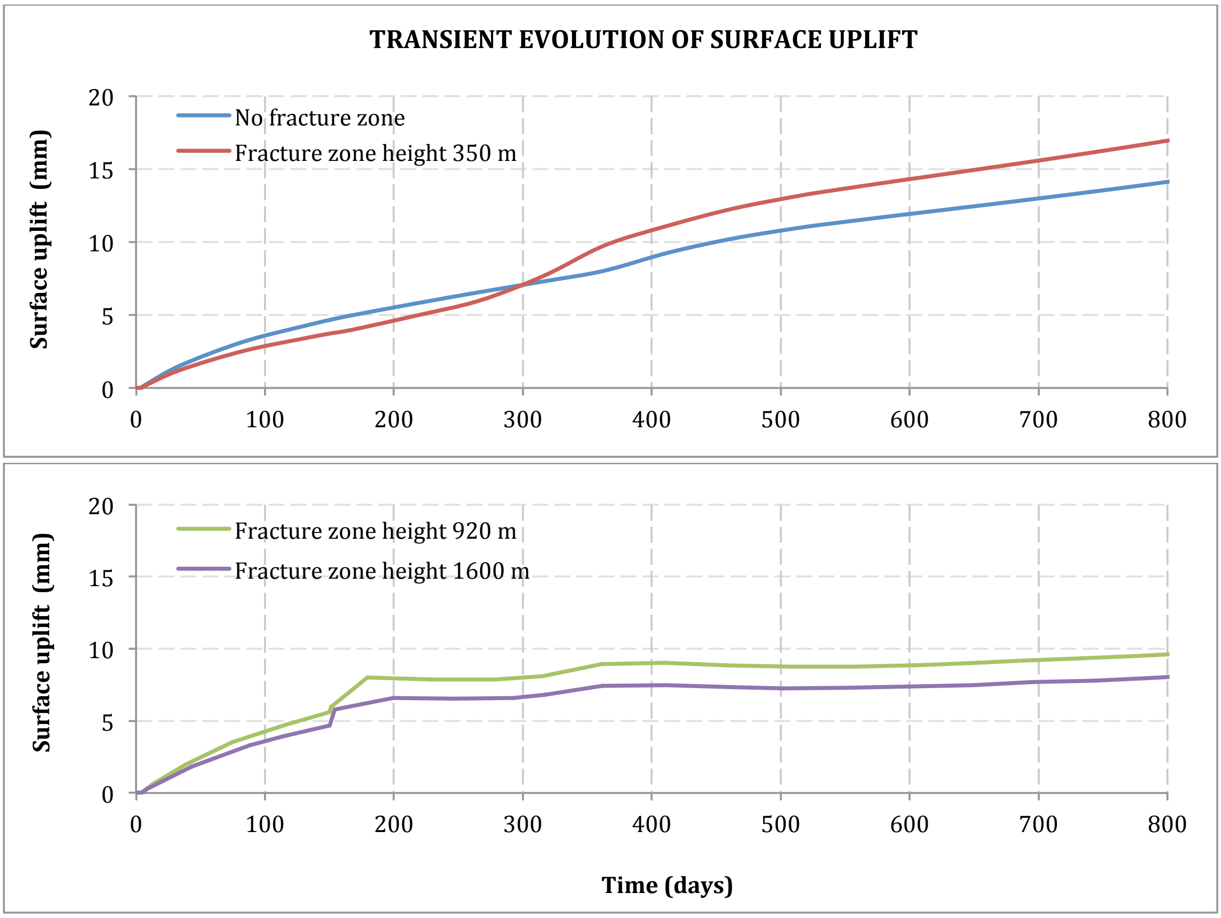

Figures 27: Evolution of maximum vertical displacement with time for different fracture zone conditions. Note the effect of fracture zone height on surface uplift.

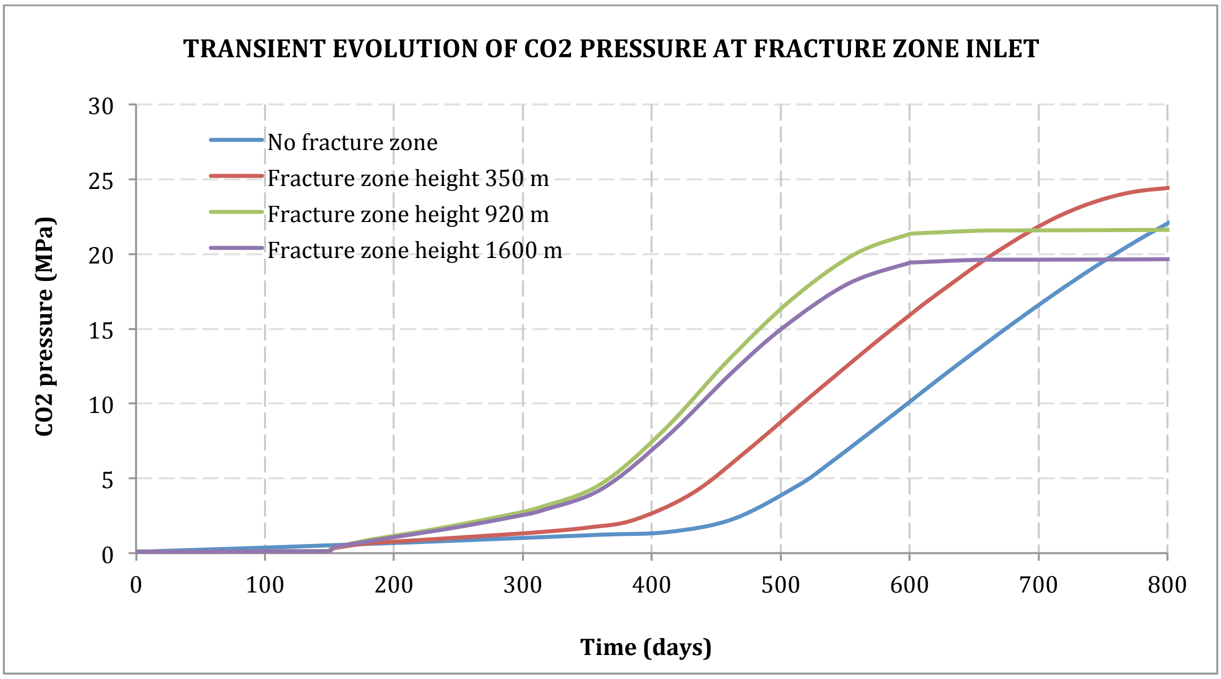

Figures 28: Evolution of CO_2 pressure with time at the contact between fracture zone and injection reservoir.

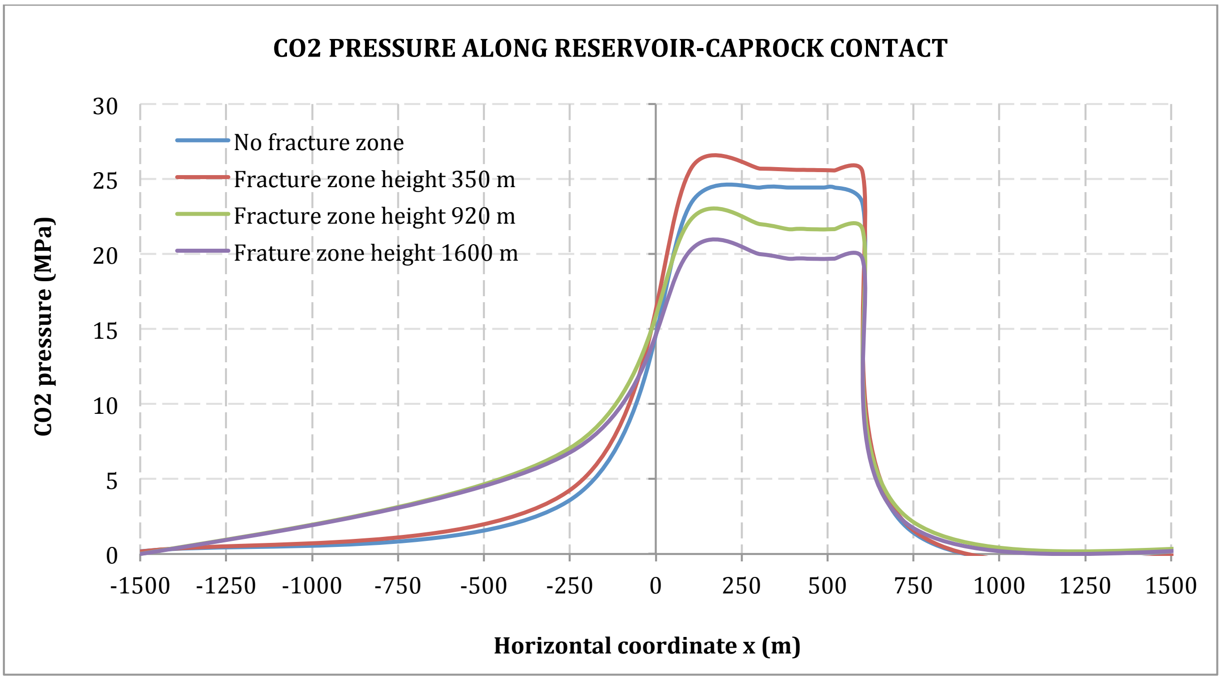

Figures 29: CO_2 pressure along the reservoir-caprock contact after 800 days of injection.

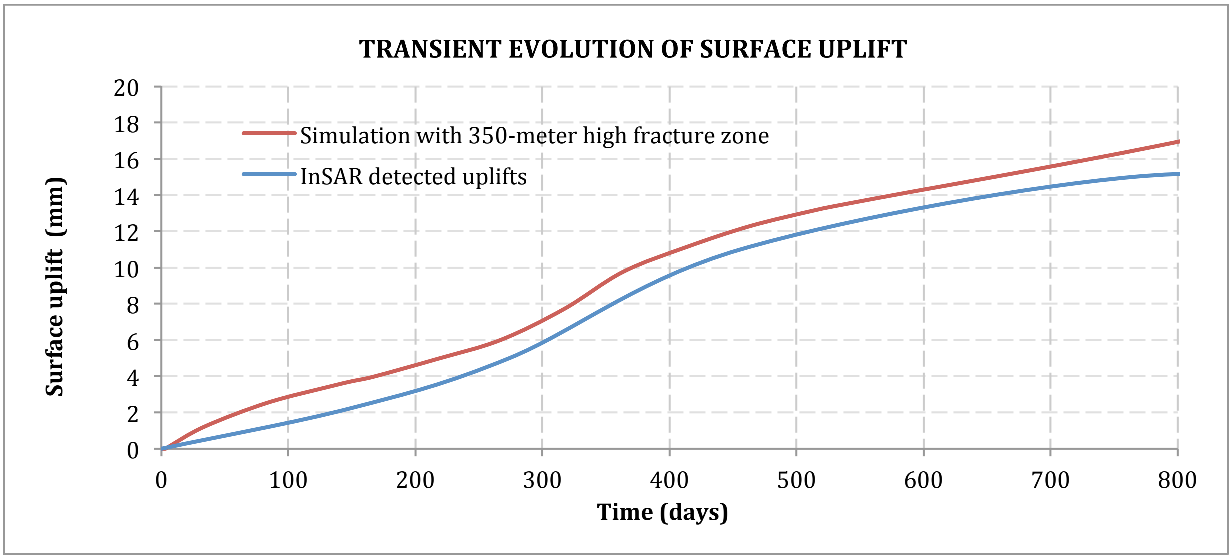

Figures 30: Comparison between simulated and InSAR detected uplifts at In Salah.

4.3.4. Ground uplifts at In Salah: concluding remarks

A 2D simulation of the KB-502 injection well activity during 800 days has been carried out with the objective of studying how the existence of a vertical feature affects vertical displacement and, in particular, how it explains the double-lobe pattern observed in InSAR images. It is concluded that:

- The double-lobe pattern is, indeed, associated to a vertical zone that allows the injected fluid to migrate. A typical uplift (one-lobe) is observed when no fracture zone is considered, thus the unusual deformational behaviour indicates the presence of a damaged area in the caprock overlying the injection reservoir.

- The fact that the two lobes are separated by no more than 1 km and have a clearly defined minimum between them is an indication of the vertical orientation of the damaged feature.

- The double-lobe pattern appears because of: (1) the tendency of the fracture zone to expand laterally when fluid penetrates it and (2) a slight pressure dissipation due to the opening of the higly-conductive vertical path, which leads to a less pronounced uplift above it.

- It is not necessary to model the fracture zone as a higly anysotropic material to simulate the double-lobe effect. This pattern is observed as long as the fracture zone is allowed to change its permeability and become pervious enough for CO_2 migration to happen.

- The existence of a fracture zone and its potentiality for allowing fluid flow has a big effect on vertical displacement values. The assumption of one fracture height or another, as well as how permeabilty varies with pressure build-up, can make a big difference when simulating surface uplifts.

- It is difficult to establish the height of the fracture zone. A more detailed, 3D model would be needed to reproduce the surface uplift values accurately. Nevertheless, the values which have been obtained indicate that the fracture zone is probably confined within the caprock limits, with a height close to 350 m. Further reasearch would be necessary to confirm this.

CHAPTER 5

SIMULATION OF A TYPICAL CARBON STORAGE SITE: DESCRIPTION

5.1. Introduction

Last section of this work is devoted to the simulation of a typical reservoir-caprock environment in which a geological sequestration project could be implemented. Chapter 5 is aimed at describing the model in question (geometry, material properties, boundary conditions,...), while in the following, and last chapter of this thesis, results will be presented and discussed. The main interest here lies in comparing both CO_2 and storage site behaviour under different conditions, which could basically be summarised as damaged and undamaged situations. The undamaged scenario represents the ideal conditions for a carbon storage poject to be implemented, while the damaged one is useful to understand which dangerous situations could be triggered if the injection is performed in sites where fractured materials exist.

5.2. General model

All three simulated cases are based on the same model presented in several papers published by the Lawrence Berkeley National Laboratory. More precisely, most of the information has been obtained from *Cappa & Rutqvist, 2010. Modeling of coupled deformation and permeability evolution during fault reactivation induced by deep underground injection of CO2*. The geometrical conditions of the basic model are introduced in figure 31. The geological medium is assumed to have infinite horizontal extension, thus the hypothesis of plane strain conditions seems reasonable at this point and the domain is modelled as a 2D geometry. It consists of a multilayer system made up by three aquifers (upper, basal and storage aquifer) as well as two low-permeable layers (caprocks) which bound the reservoir. Permeable aquifers represent sandstone, whereas caprocks represent shale. The vertical extension of each layer is:

- Upper aquifer: From $\mathrm{z} = 0\ \mathrm{m}$ to $\mathrm{z} = -1350\ \mathrm{m}$
- Upper caprock: From $\mathrm{z} = -1350\ \mathrm{m}$ to $\mathrm{z} = -1450\ \mathrm{m}$
- Storage aquifer: From $\mathrm{z} = -1450\ \mathrm{m}$ to $\mathrm{z} = -1550\ \mathrm{m}$
- Lower caprock: From $\mathrm{z} = -1550\ \mathrm{m}$ to $\mathrm{z} = -1700\ \mathrm{m}$
- Basal aquifer: From $\mathrm{z} = -1700\ \mathrm{m}$

Note that this follows one of the typical geological structures for carbon dioxide capture, as mentioned in chapter 1. All layers are horizontal, but since the storage area is very big compared to the volume of fluid that is going to be injected, one expects the CO_2 to remain relatively trapped by both caprocks unless a fractured zone exists.

The multilayer system is discretized in a two-dimensional model with both a horizontal and a vertical extension of 2 km (i.e a 2 km x 2 km square). In the vertical direction the model extends from 500 m to 2500 m depth, whereas horizontally it has to be large enough so as to guarantee that the boundary does not affect results in the zone of interest. In other words, this boundary has to be far enough from the injection point to ensure that laterally infinite acting conditions can be properly simulated. Consulted documents and papers suggest a horizontal size of 2 km, a number which has been chosen after performing several sensitivity studies (*Rutqvist et al., 2010*). [12]

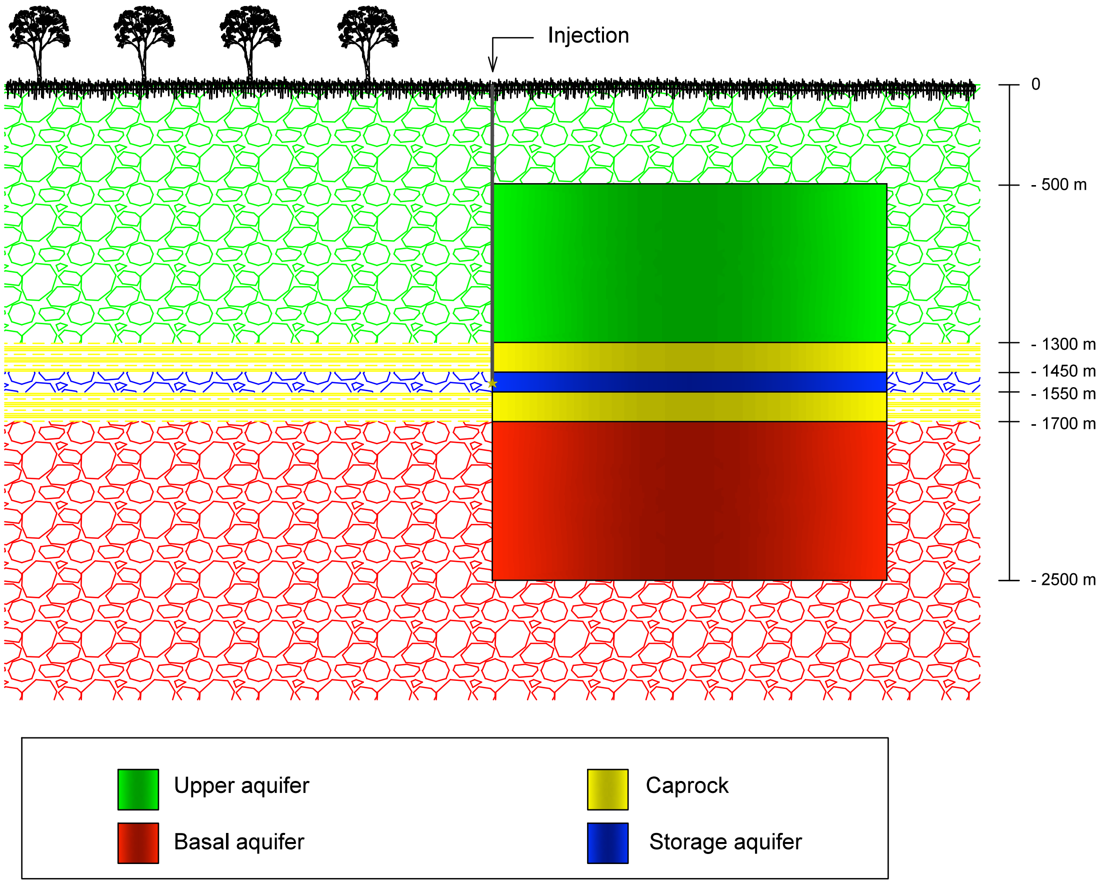

Figure 31: Geometry of the multilayer system modeled to simulate the injection of $\mathrm{CO_2}$.

Mechanical and hydraulic boundary conditions, as well as initial conditions, have to be set. In both left and right boundaries, the horizontal displacement is restricted so as to simulate symmetry conditions (left) and nule lateral deformation due to the fact that, horizontally, the multilayer system is infinitely extense (right). The latter is also a reasonable hypothesis because the right boundary is far enough from the injection point. In the lower boundary the vertical displacement is restricted while, on the upper boundary, a distributed load equal to *11.085 N/mm* is prescribed so as to simulate the weight of material that lies above the modeled domain. As for hydraulic conditions, liquid pressure is prescribed in the upper and lower boundaries (5 MPa and 24.63 MPa, respectively) and gas pressure is set to a very low value or even zero to simulate almost fully-saturated conditions far from the injection point. A depth gradient of 25 ºC/km is considered [12] so, assuming a temperature of 10 ºC on the ground surface, a temperature of 22.5 ºC and 72.5 ºC is prescribed at the -500 m and -2500 m boundaries respectively. No flow occurs in the left boundary.

Initial conditions are set on the whole 2D domain. Except for initial gas pressure, which is constant and equal to zero (or very small) at every point, all the other variables (stress, temperature and liquid pressure) are, initially, linearly variable with depth according to material density (or specific weight), depth gradient of temperature and hidrostatic pressure, respectively. An extensional stress regime ($\sigma_h = 0.7\ \sigma_v$) has been assumed. It is important to note that not only initial values for the unknowns have been defined, but also initial values for some other relevant variables which play a major role in the THM problem have been considered. For example, as mentioned, initial stress state is defined, as well as other variables such as initial porosity or degree of saturation, which is implicitely prescribed once initial gas and liquid pressure have been set.

In this simulation, carbon dioxide is injected as a point source at 1500 m depth with a constant rate of 0.02 kg/s/m. Remember that this is actually a 3D problem, so the fluid should be injected through a horizontal well, which turns into a single point if only a section of the problem is simulated. This is why the injection rate is defined in units of mass per unit of time and distance. At 1500 m depth, supercritical conditions for the CO_2 are assured because of initial fluid pressure (14.72 Mpa) and temperature (47.5 ºC). Figure 32 shows the 2D domain that has been modelled as well as some of the prescribed boundary and initial conditions. Table 5 shows the most relevant mechanical and hydraulic properties of the materials that make up the different layers of the media (note that elastic behaviour has been assumed, thus making the number of data necessary to define the problem smaller).

Another important material property that has to be defined is the relative permeability function, which indicates how conductivity variates with the (liquid) degree of saturation (see chapter 2). Since we don't have enough experimental data to define a more accurate expression for relative permeability, it has been estimated to be proportional to $S_r{}^6$ following data provided by other similar examples where reservoir-caprock systems were involved (*UPC. June, 2013.CODE_BRIGHT tutorial manual*). If k_{rl} refers to liquid relative permeability, then we consider that gas relative permeabilty k_{rg} is equal to $1 - k_{rl}$, although more complex relationships between all these variables could be defined if with more experimental data. Remember that relative permeabilty is a value between 0 and 1 that affects the intrinsic value and accounts for the fact that the material is not completely saturated. Figure 33 shows how relative permeability evolves with the degree of saturation.

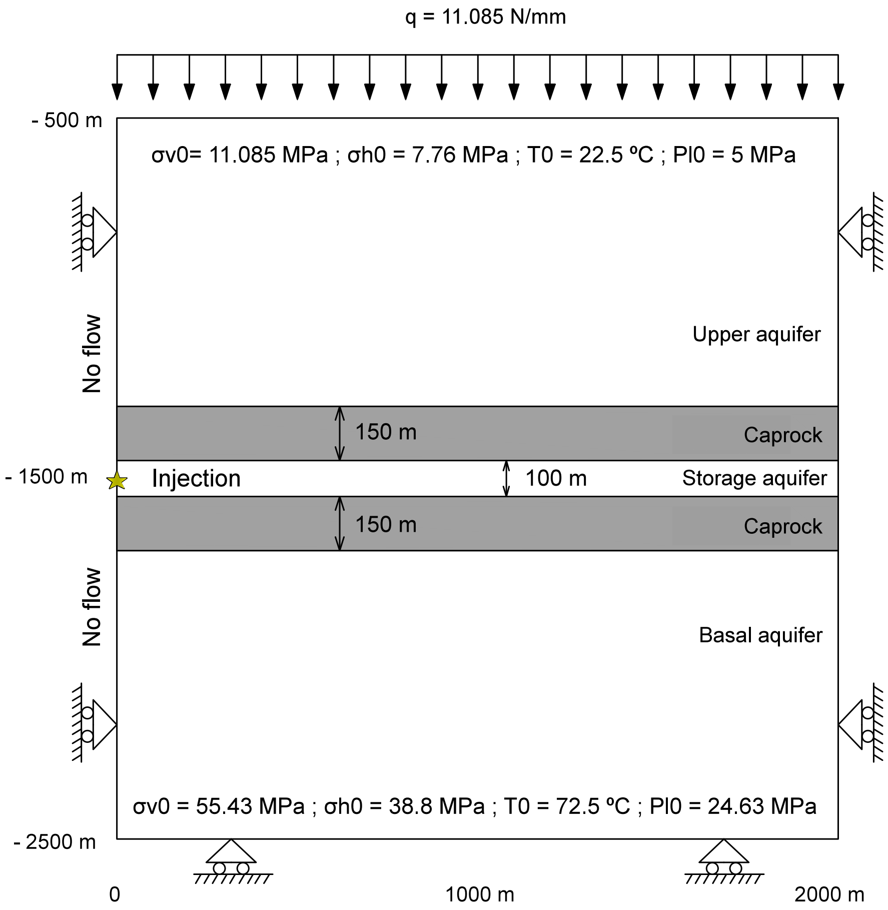

Figure 32: Model geometry, including the main boundary and initial conditions.

Parameters	Upper aquifer	Caprock	Storage aquifer	Basal aquifer
Young's modulus E (GPa)	10	10	10	10
Poissons ratio υ (-)	0.25	0.25	0.25	0.25
Rock density ρ_s (kg/m^3)	2260	2260	2260	2260
(Initial) porosity ϕ (-)	0.1	0.01	0.1	0.01
Intrinsic permeability k(m^2)	$1{\times}10^{-14}$	$1{\times}10^{-19}$	$1{\times}10^{-13}$	$1{\times}10^{-16}$
Residual gas saturation (-)	0.05	0.05	0.05	0.05
Residual liquid saturation (-)	0.2	0.2	0.2	0.2
Van Genuchten P_0 (MPa)	0.02	1	0.02	1
Van Genuchten λ (-)	0.7	0.3	0.7	0.3

Table 5: Material properties of the reservoir-caprock system where the CO_2 injection is going to be simulated

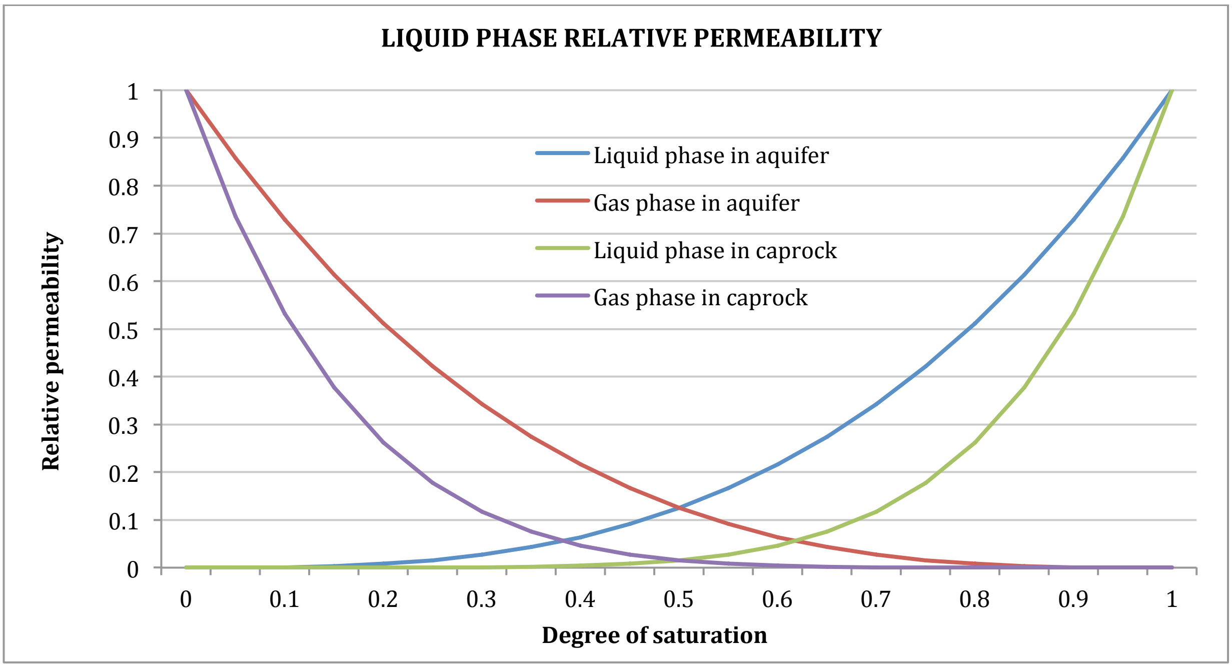

Figure 33: Relative permeability of liquid and gas phases in aquifer sandstones and caprock shales.

Figure 34 and 35 show the retention curves of each type of material, following the data provided by the table presented above these lines. The first curve represents the behaviour of both the central (reservoir) and upper aquifer while the second one represents the caprock material. Since the aquifer sandstones are much more permeable and have bigger pore size than the caprocks, the material starts to desaturate with lower suction forces. With a suction value close to 100 kPa, the aquifer materials get almost completely dessaturated. Caprock shales, on the other hand, are much less pervious and have smaller void size, a fact that explains why bigger suction forces are needed to desaturate the material.

Taking the geometry depicted in figure 32, three different cases are simulated. The idea is to simulate CO_2 injection in a not fractured geological formation first and, then, include the concept of damaged geological formation by embedding joints in the elements that make up the mesh.

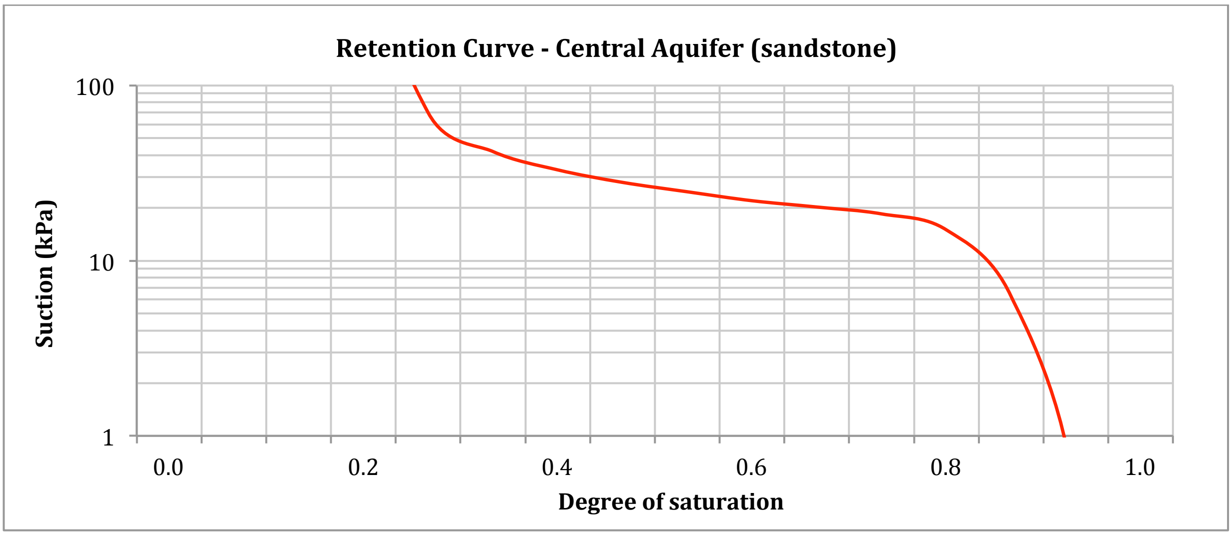

Figure 34: Retention curve of the materials that make up the central and upper aquifers (sandstone).

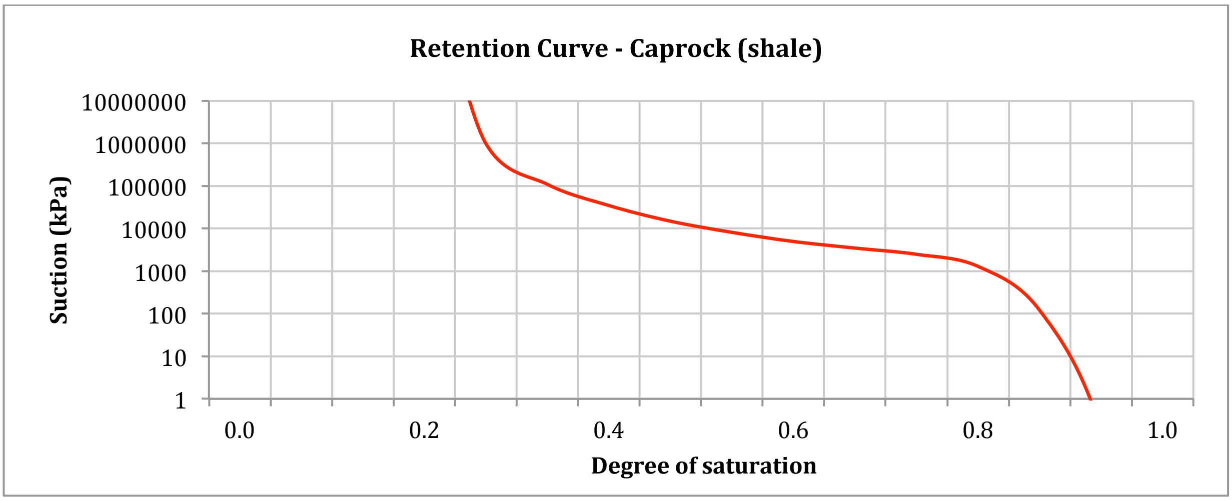

Figure 35: Retention curve of the materials that make up the caprocks (shale).

5.3. Not damaged geological formation

This case refers directly to the geometry depicted in figure 32 and the material properties shown in table 5. The fluid is injected in the central or storage aquifer, bounded by two caprock layers that keep the CO_2 within the reservoir. In general, this would be an ideal site to perform CCS injection tasks because the fluid would remain capped within the storage layer and no risk of CO_2 reaching and polluting other aquifers would exist.

Due to the effect of buoyancy, one expects carbon dioxide to remain within the space bounded by the caprocks, but with a tendency to move upwards and then expand laterally just like it was described in Chapter 2 when talking about the evolution of the plume. Injection implies CO_2 pressure build-up which also leads to a liquid pressure increase due to equilibrium between both phases. Thus, a certain vertical displacement is expected on the ground surface. It is important to control the amount of fluid being injected in the central aquifer so as to avoid net effective stress to get close to zero or even reach a negative value. Nevertheless, the fact that the injection is performed at such depth allows for quite reasonable and efficient injection rates due to the existence high initial stresses.

5.4. Damaged geological formation: fractured caprocks

Now, the same geometry as the one depicted in figure 32 is considered, as well as similar properties as those shown in table 5 for all layers except for the caprocks. The main difference is that now it is assumed that the material (shale) that makes up the caprocks is full of fractures. Actually, it is assumed that the whole caprock is highly fractured (see figure 36), to such an extent that isotropic properties can be assumed in that two layers. Fractures exist and are initially closed (or almost closed), but one expects them to open progressively as fluid pressure increases.

From a mechanical point of view, the damage in the caprocks is simulated by reducing its Young's modulus to 5 GPa. Nevertheless, it is in the hydraulic properties where most of the interest lies. In this line, the embedded joints approach (already explained in Chapter 3) is implemented. Table 6 shows the new properties for the fractured caprock.

At this point, it is important to remember that the main feature of the hydraulic model considered here is the variation of permeability with joint aperture. Since joint aperture depends on the stress-strain relationship and, at the same time, effective stresses depend on fluid pressure, it is straightforward to see that CO_2 injection will lead to fracture opening and an increase in permeability. As mentioned in Chapter 3, permeability increases with strain as follows:

$$\mathrm{k} = \mathrm{k}_{\mathrm{matrix}} + \frac{[\mathrm{b}_0 + \mathrm{s}(\varepsilon - \varepsilon_0)]^3}{12\ \mathrm{s}} \tag{37}$$

It is important to note that k_{matrix} is not a constant value because, although it does not depend on joint opening, it may change with porosity. CODE_BRIGHT's hydraulic model accounts for porosity variation as well as joint aperture. However, in this case the effect of fractures is much bigger than porosity variation (note that the materials are, in general, quite stiff).

Although parameter s has the physical meaning of fracture spacing, in practice it can be treated as a parameter used to control joint opening. It is interesting not to pick a very small value of s so as to simulate joint opening properly but, on the other hand, very big values would lead to abrupt (and not realistic) permeability changes.

Another important aspect is which strain value (ε) is considered to compute permeability change. In CODE_BRIGHT two different values can be chosen: deformation according to the joint direction or volumetric strain. In our case, since it is assumed that the caprocks are highly fractured and the material behaves in an elastic way, the second option has been chosen. Figure 37 shows how permeability evolves with fracture aperture. The graphic shows how intrinsic permeability starts to increase once fracture aperture reaches a value close to 10^{-6} m, assuming an initial joint aperture equal to 10^{-7} m.

With fractured caprocks, fluid is expected to move upwards and reach the upper aquifer. At first, the behaviour of the plume is expected to be similar to the previous case until the pressure build-up leads to joint opening. Once CO_2 starts to migrate, pressure is not expected to keep increasing like it did when the fluid was completely capped. This would translate into smaller vertical displacements on the ground surface and a less sustained decrease in effective net stresses.

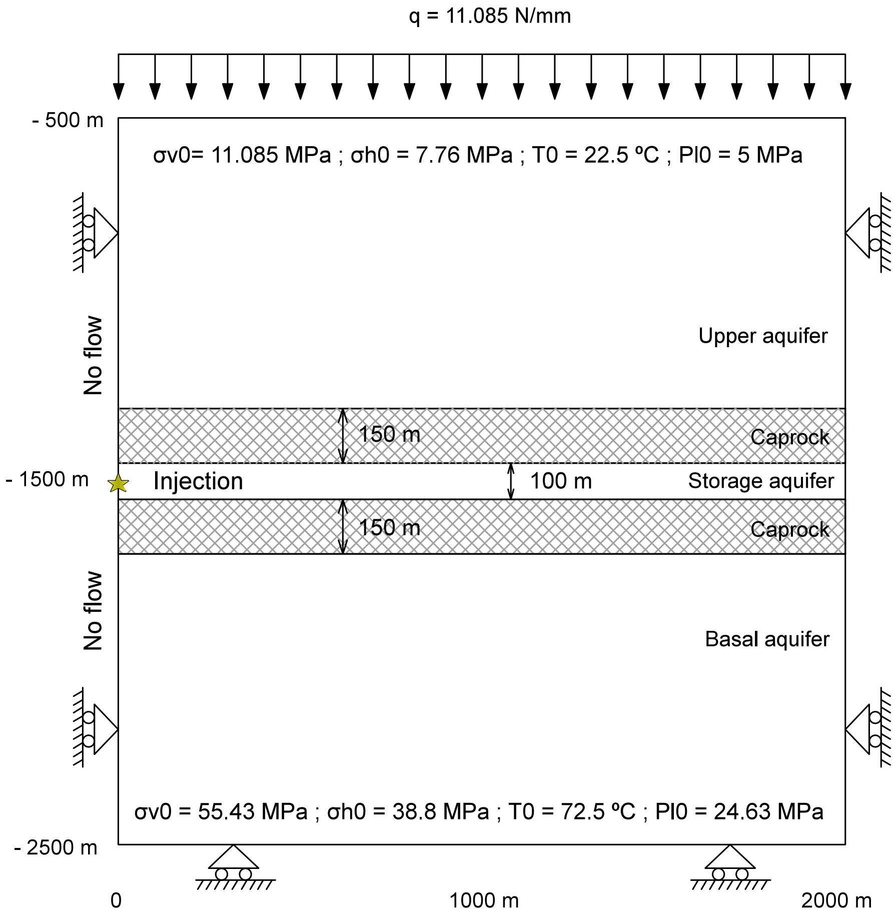

Figures 36: Model geometry with fractured caprocks

Damaged caprock properties	
Young's modulus E (GPa)	5
Poissons ratio υ (-)	0.25
Rock density ρ_s (kg/m^3)	2260
(Initial) porosity ϕ (-)	0.01
Intrinsic permeability k (m^2)	Variable with an initial value of 10^{-19}
Residual gas saturation (-)	0.05
Residual liquid saturation (-)	0.2
Van Genuchten P_0 (MPa)	1
Van Genuchten λ (-)	0.3
Hydraulic model properties (caprock)	
Initial intrinsic permeability k (m^2)	1×10^{-19}
Initial porosity ϕ (-)	0.01
Initial aperture b_0 (m)	1×10^{-7}
Threshold strain ε_0 (-)	0
Fracture spacing s (m)	0.5
Maximum aperture b_{max} (m)	1×10^{-2} (not restricted)

Table 6: Material properties and hydraulic model parameters for the highly fractured caprock

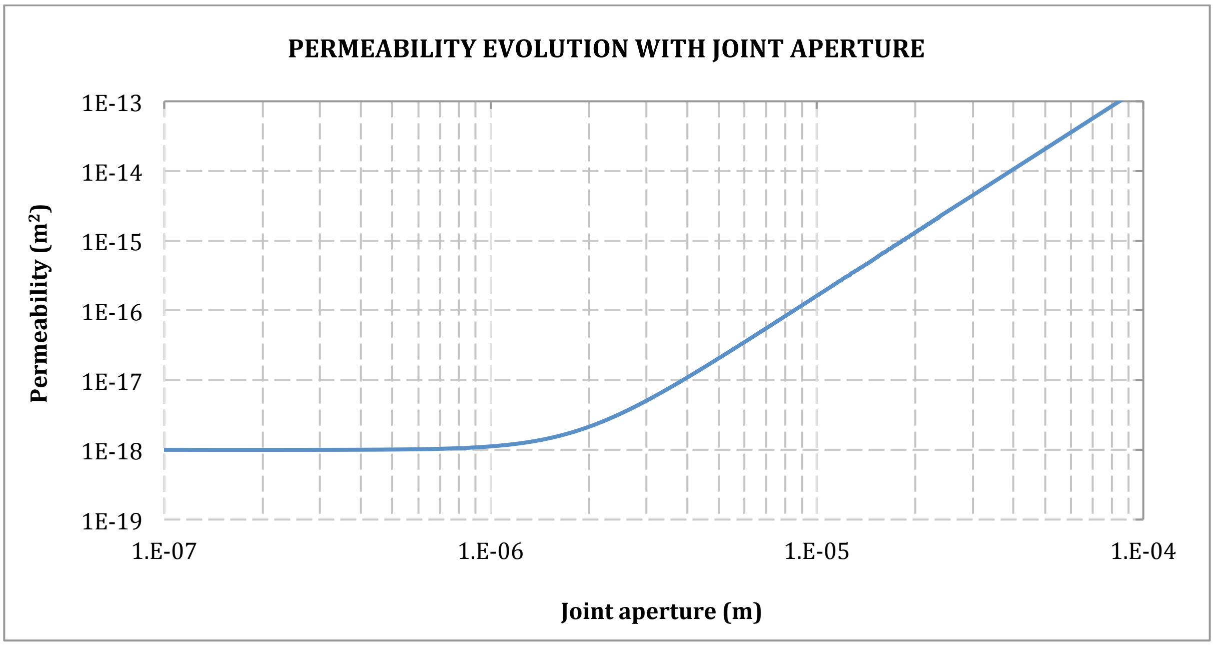

Figure 37: Evolution of intrinsic permeability due to joint opening. The graph shows the relationship between volumetric strain and intrinsic permeability starting from the initial value $k_0 = 1\times10^{-18}$

5.5. Damaged geological formation: fault zone

In this third and last simulation example, a geometry as the one depicted in figure 38 is considered (all conditions are the same as in the previous two cases). Note that the only difference with respect to figure 32 is that, in this case, it is assumed that the multilayer system is intercepted by an already existing fault with a dip angle of 90º. For an extensional stress regime like the one we have presented ($\sigma_h / \sigma_v = 0.7$) the natural tendency of the medium is to develope discontinuities with dip angles ranging from 45º to 90º (probably close to 60º) rather than more horizontal ones. Thus, the assumption of a pre-existing vertical (or almost vertical fault) seems reasonable. The horizontal distance between the fault and the injection point is 500 m. In reality, the existence of faults commonly imply a few meters offset between both sides of the fault due to the relative displacement that such discontinuities generate. [11] However, in this case a minor fault with an offset of just a few meters (less than 10 m) is envisioned, so this offset would not affect gas flow.

As mentioned in the last subsection of chapter 3, different approaches can be considered to simulate the fault zone. Actually, since the fault width is indeed very small in comparison to the size of the modeled geometry (2km x 2km), a zero thickness joint interface could be considered so as to model its hydro-mechanical behaviour. Nevertheless, one of the main interests here lies in being able to see how the CO_2 plume evolves with time and, in particular, how the fluid may escape from the primary storage site due to the existence of a damaged zone. Since a joint interface would not allow a visualisation of fluid migration, it is considered that approaching this case from the embedded joint perspective is the best option for these purposes. Additionally, in a more detailed analysis than the developed here, the finite element approach would allow to model the different components of the fault architecture so as to obtain a quite realistic behaviour of the zone in question. This would require a pretty refinate finite element mesh which would allow to assign different properties (mechanical and hydraulic) to each series of elements and represent both the fault core and damaged zone (see table 7 figure 39).

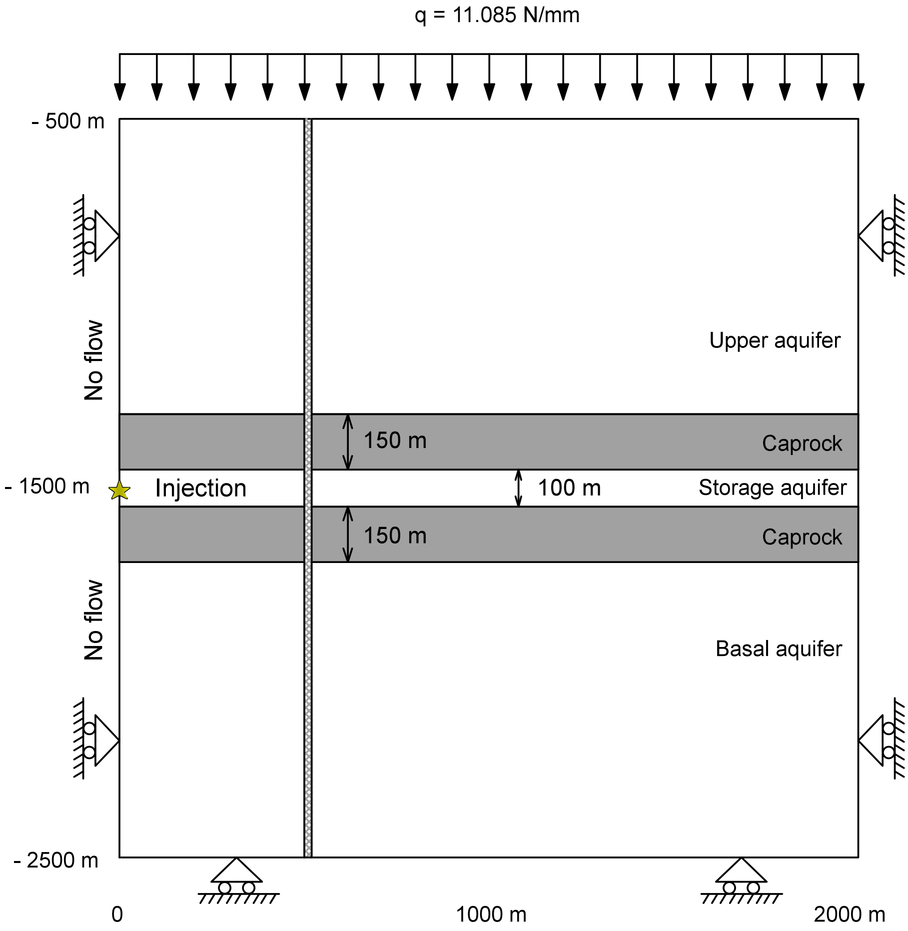

Figure 38: Model geometry with fault zone represented by finite elements with embedded joints

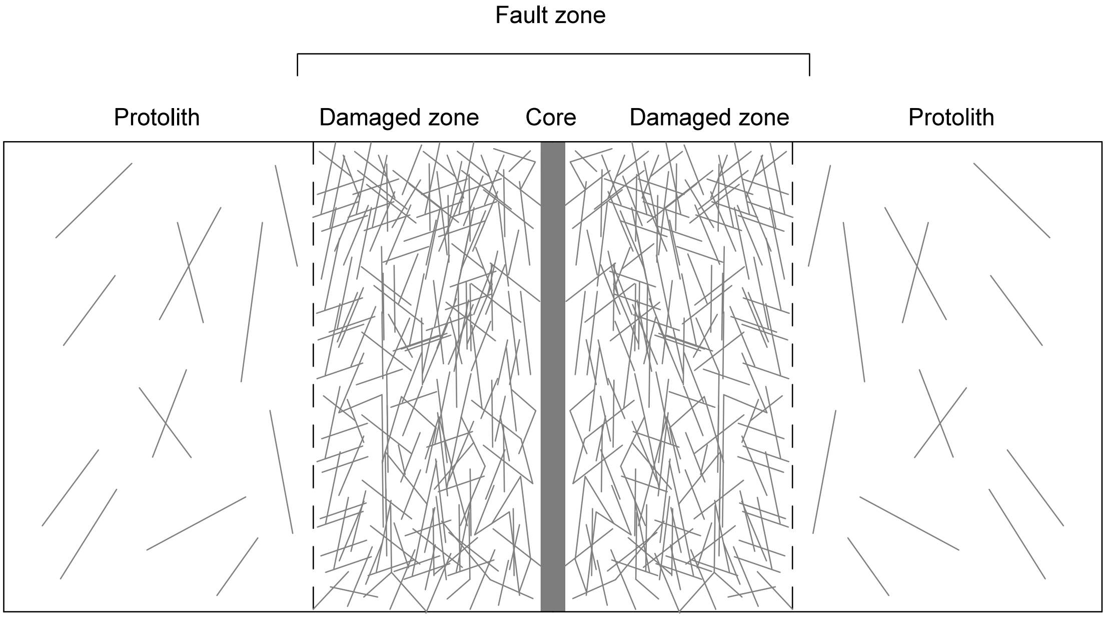

Figure 39: Fault architecture, schematical view of its structure.

Properties	Core	Damaged zone	Protolith
Young's modulus E (Gpa)	1	$1-10$	$50-70$
Permeability k (m^2)	$10^{-17}-10^{-21}$	$10^{-13}-10^{-16}$	$10^{-16}-10^{-18}$

Table 7: Approximated values of permeability and Young's modulus for the different zones that make up a typical fault structure

All materials have the same properties as the ones in the first case, but a new material (i.e. the 20-metre wide fault zone) is introduced now. New properties are defined in a similar way to the ones defined for fractured caprocks, this is, modelling the damaged areas by reducing the Young's modulus (in comparison to intact rock) and simulating permeability changes by using expression (37) with volumetric strain. The initial fault permeability is set to $k_0 = 1{\times}10^{-16}$, which is a reasonable value considering field and laboratory data (*Wibberley and Shinamoto, 2003 ; Townend and Zobak, 2000 ; Talwani & Acree, 1984*). This value is indeed a lower limit of the permeability within the damaged zone within a typical fault (see figure 39 and table 7). Note that this zone is more permeable than the surrounding caprock (shale) even before joint aperture. It is important to point out that an elastic model has been considered for simplicity and lack of data to simulate the problem using a more complex constitutive model. Table 8 summarizes the main mechanical and hydraulic properties of the fault zone.

At first, a similar behaviour to case 1 is expected, which means that the injected fluid is expected to start moving horizontally until it reaches the fault zone. Then, some fluid may penetrate the damaged zone and pressure build-up may trigger joint opening to such an extent that permeability can increase by 2 or 3 orders of magnitude, taking the damaged zone permeability close to its upper limit. It is important the note that, while the fault zone may act as a conduit within the caprock (due to its higher permeability), it may as well act as a barrier within the storage site. This implies that pressure may increase more than in the previous cases until the fault is reactivated (this is, until joint start to open).

Fault zone properties	
Young's modulus E (GPa)	5
Poissons ratio υ (-)	0.25
Rock density ρ_s (kg/m^3)	2260
(Initial) porosity ϕ (-)	0.1
Intrinsic permeability k (m^2)	Variable: $1{\times}10^{-16}$ - $2{\times}10^{-13}$ approx.
Residual gas saturation (-)	0.05
Residual liquid saturation (-)	0.3
Van Genuchten P_0 (MPa)	0.02
Van Genuchten λ (-)	0.7
Hydraulic model properties (fault zone)	
Initial intrinsic permeability k (m^2)	$1{\times}10^{-16}$
Initial porosity ϕ (-)	0.1
Initial aperture b_0 (m)	$1{\times}10^{-7}$
Threshold strain ε_0 (-)	0
Fracture spacing s (m)	0.5
Maximum aperture b_{max} (m)	$1{\times}10^{-2}$

Table 8: Material properties and hydraulic model parameters for the fault zone.

CHAPTER 6

SIMULATION OF A TYPICAL CARBON STORAGE SITE: PRESENTATION AND DISCUSSION OF RESULTS

6.1. Not damaged storage site

- CO_2 *plume and gas pressure*

As expected, due to the presence of the caprocks sealing the injection aquifer and avoiding further vertical migration, the fluid plume has a tendency to spread laterally. It moves from the injection point, around which gas pressure builds up fast, to the rest of the reservoir due to pressure difference and following Darcy's law as explained in detail in Chapter 2. In spite of having a liquid-like density due to supercritical conditions, carbon dioxide is still less dense than water (or brine), a fact that explains the particular shape the plume has, which somehow resambles a logarithmic function.

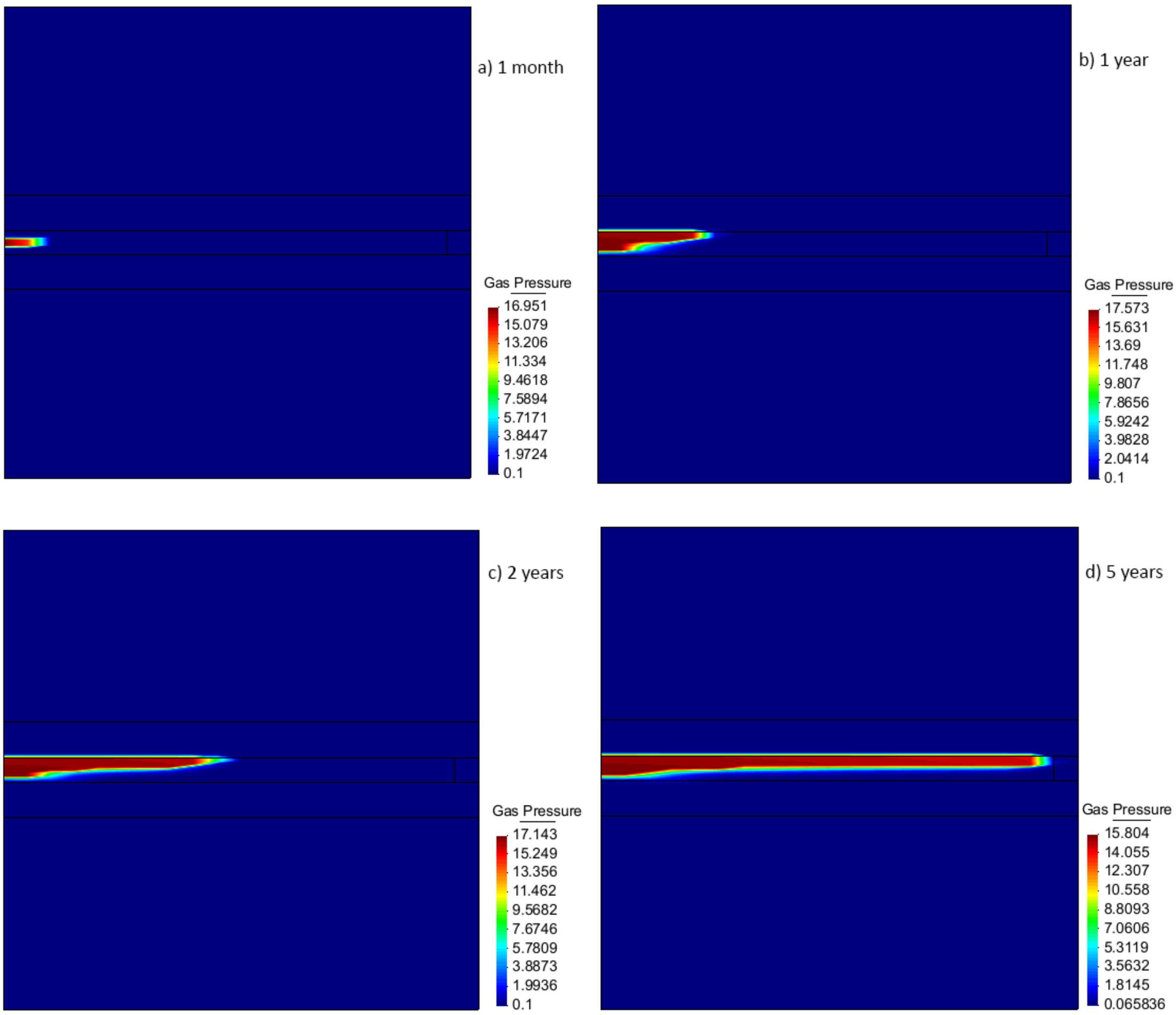

Figure 40: CO_2 plume and pressure (in MPa) at different stages of the injection process (not damaged).

Figures 40.a, 40.b, 40.c and 40.d show how the CO_2 plume evolves with time, as well as the pressure values the supercritical fluid reaches at every point. A sharp interface between supercritical fluid and water / brine is observed. Figure, on the other hand, shows the transient evolution of CO_2 pressure at the injection point and two more points located along the reservoir (y=-1500 m). Note the rapid pressure increase since the beginning of injection, which is a typical behaviour in this type of processes.

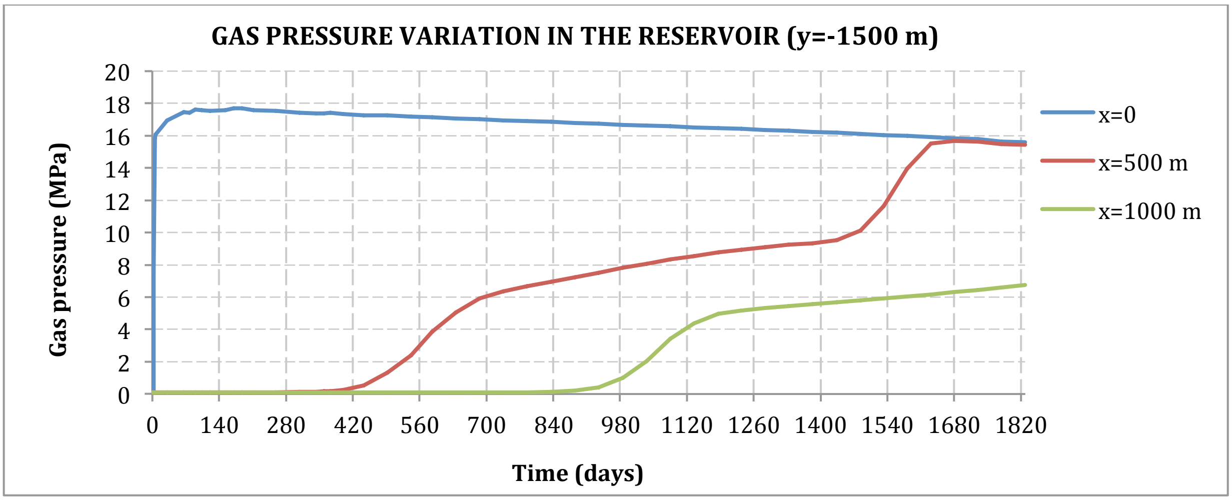

Figure 41: Gas pressure evolution at three points located in the reservoir (not damaged)

- *CO_2 density*

Gas density reaches a maximum value of $750\ \mathrm{kg/m^3}$ at the injection point and then decreases, but not much. Note that, indeed, the density is always high enough to resamble a liquid, but never reaches or surpasses the water density value. Gas density within the plume is a function of both pressure and temperature. Since the whole injection process is assumed to take place at a constant temperature (i.e the problem is isothermal), gas density variation depends on pressure variations only. This explains the almost identical evolution that both variables follow. Note how the density values are in accordance with the Redlinch-Kwong equation (figure 43)

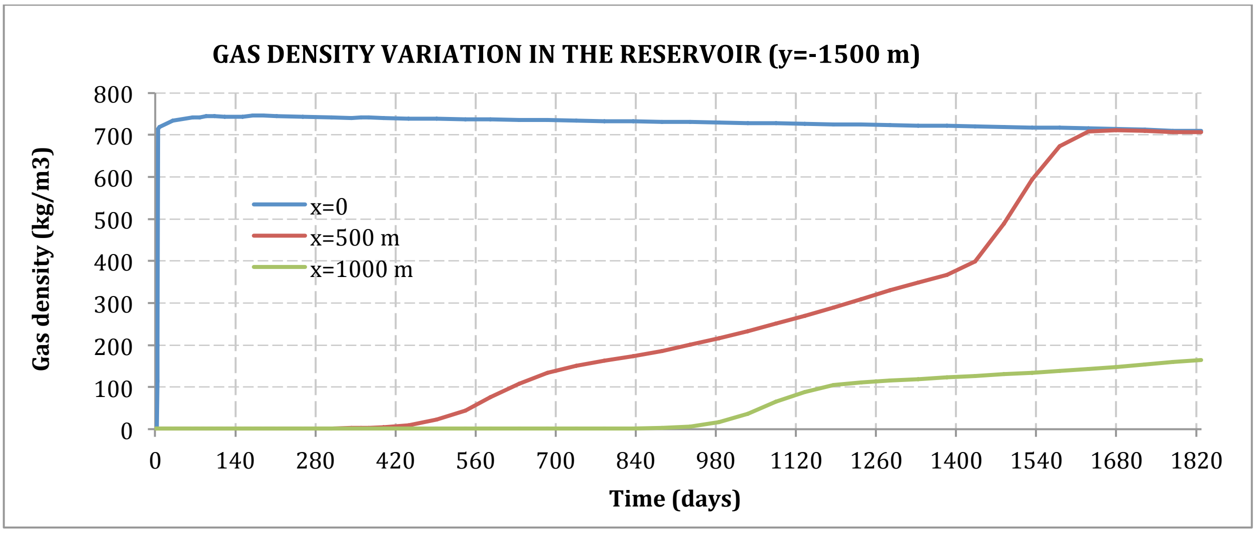

Figure 42: CO_2 density evolution at three points located in the reservoir (not damaged).

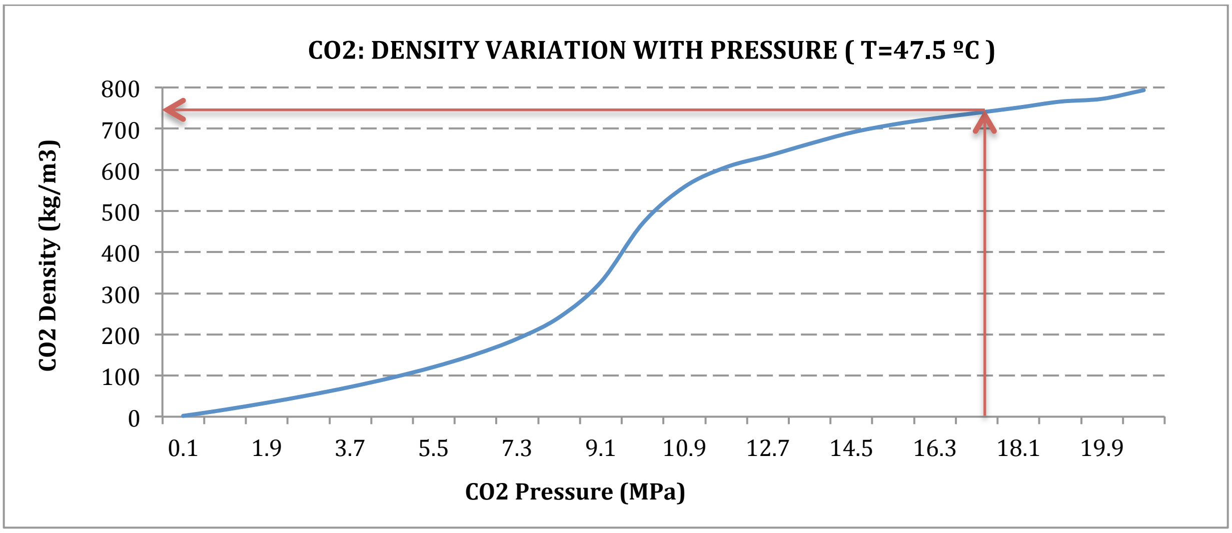

Figure 43: Redlich-Kwong equation for carbon dioxide pressure-temperature-density relationship. In this case, a temperature of 47.5 ºC has been assumed and density is a function of pressure only.

- *Liquid pressure and degree of saturation*

Due to equilibrium between CO_2 and water /brine, the pressure of the latter tends to increase until it reaches a pressure value similar to that of the former. From that moment, gas pressure generally mantains a higher value than liquid pressure, and thus suction forces (defined as gas pressure minus liquid pressure) appear. If this suction is big enough to desaturate the medium (a value that depends on the retention curve parameters), CO_2 starts to fill the reservoir voids and the (liquid) degree of saturation decreases.

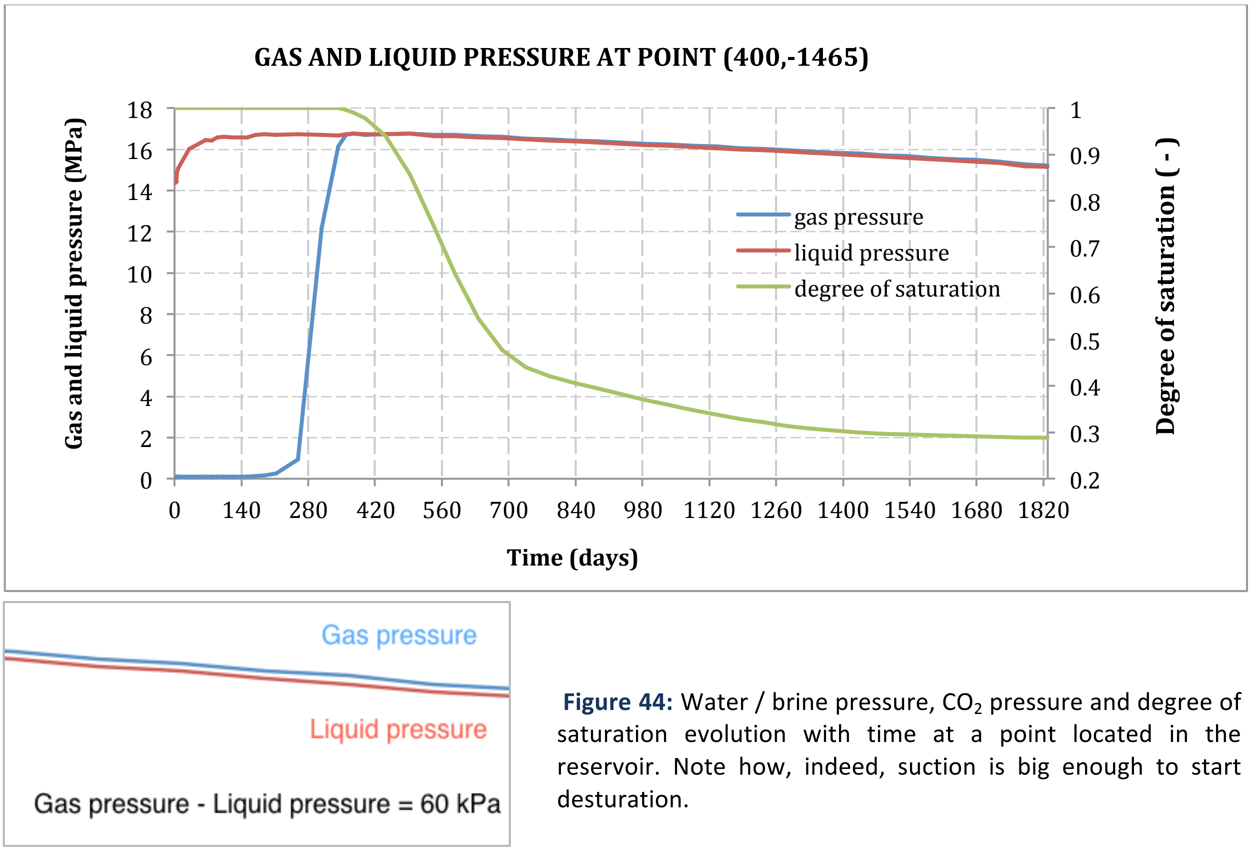

Figure 44: Water / brine pressure, CO_2 pressure and degree of saturation evolution with time at a point located in the reservoir. Note how, indeed, suction is big enough to start desturation.

Figure 44 shows the gas and liquid pressure evolution in a particular point of the medium as well the degree of saturation. Note that the medium starts to desaturate once suctions forces appear, this is, when gas pressure surpasses liquid pressure. In this case, suction is always higher than the corresponding value set in the retention curve of the reservoir material (10 kPa, approximately), a fact that explains the continuous decrease in the saturation degree. Since the residual saturation degree for liquid has been set to 25 %, this is the smallest value that can be achieved. Figures 45.a, 45.b, 45.c and 45.d depict this process of desaturation in space for different time periods.

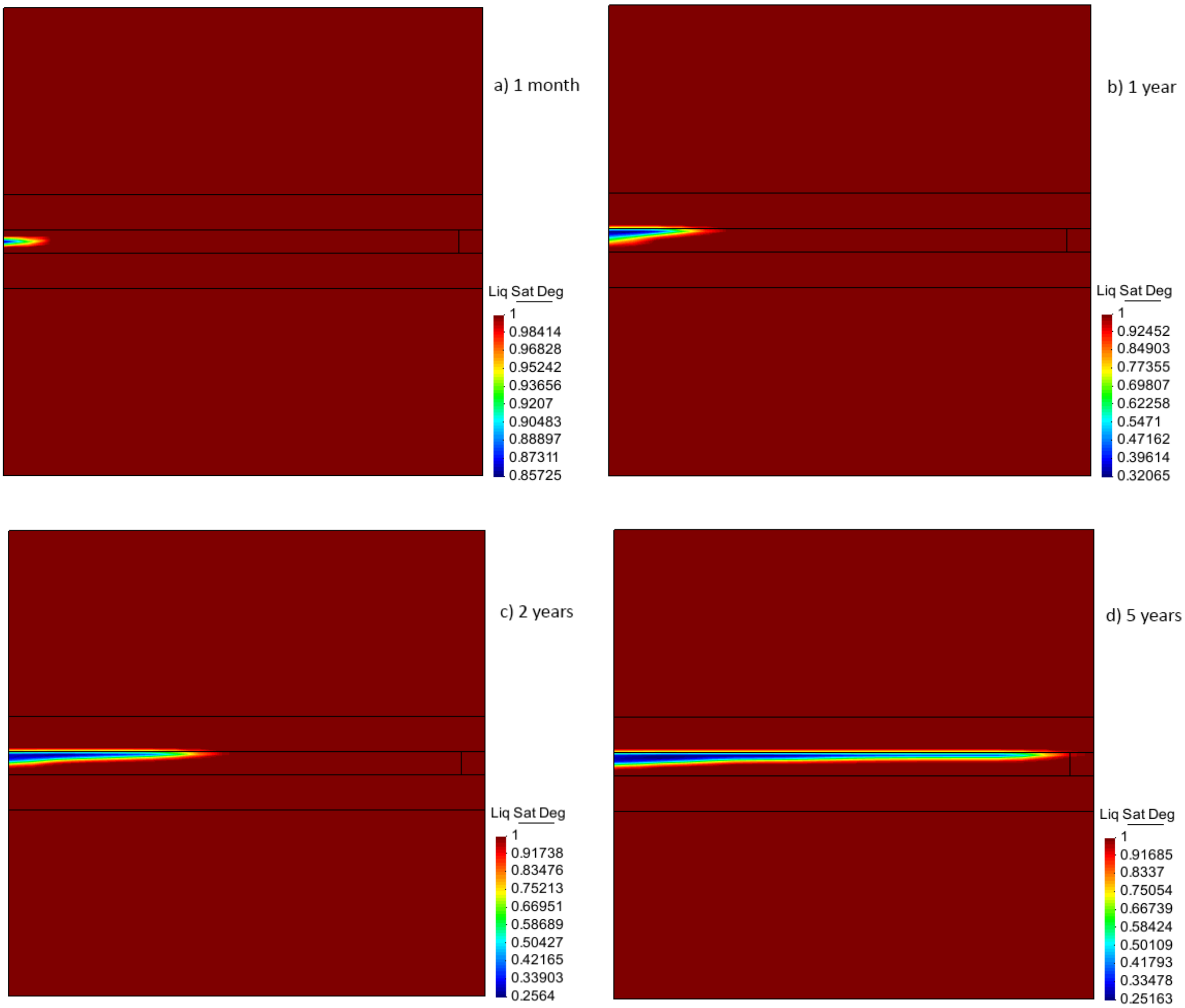

Figure 45: Liquid saturation degree, evolution with time. Note that the residual value 0.25 is a lower bound of this variable.

- *Porosity*

In this case, and despite gas injection, porosity remains almost constant during the whole process. This result was already anticipated, since all materials are characterised by high Young's moduli. It is important to remember that these injections are performed in rocks, not soils, and thus stiffness is quite high for big porosity changes to happen (E=10 000 MPa in this case).

- *Vertical displacement*

Ground surface movement is always an important issue when dealing with injection problems, not only because of the effects that such displacements can have but also because they are an indication of how the geological site is being altered by the hydro-mechanical coupling. In this particular example, it is not possible to obtain results on ground surface because the modelled domain does not reach such level. However, it is interesting to represent the vertical displacement along some lines, for example in the contacts between the reservoir and the caprocks, so as to note the significant uplift close to the injection point as well as its relationship with pressure build-up (see figure 38).

Vertical uplift reaches a maximum value of, approximately, 1.8 cm in the aforementioned contact line. This value is observed after around two years of injection. Then, as pressure stabilizes and the carbon dioxide plume keeps moving laterally, vertical displacement stabilizes and starts to decrease too. Just to give a general idea of how injection deforms the reservoir site, figures 39 depicts the altered geometry as well as the gas pressure colour map for two years. The scale has been exaggerated using a 20 000 factor to make the deformation noticeable at first sight.

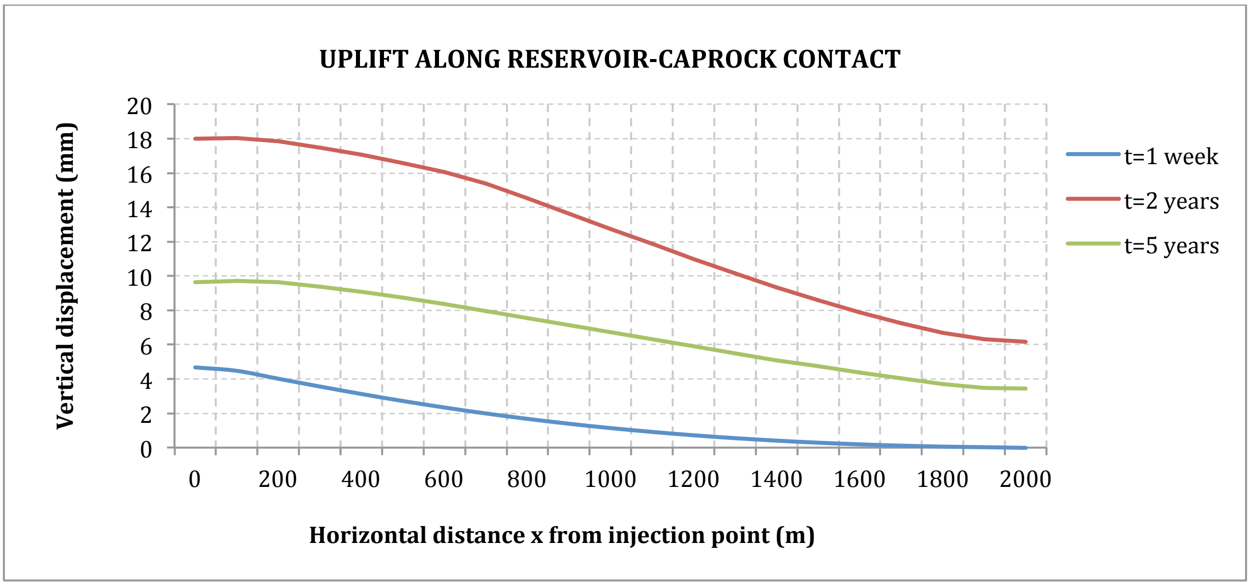

Figure 46: Profile of vertical displacements observed at different stages of the process. (not damaged)

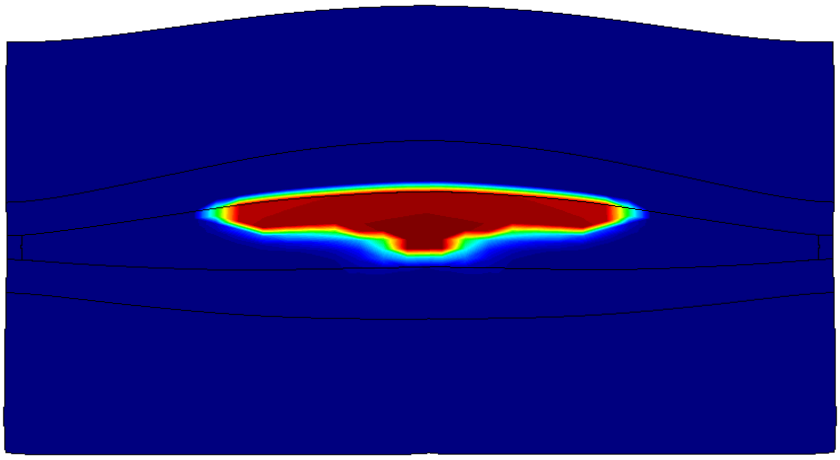

Figure 47: Deformed geometry and gas pressure colour map after two years of injection. Note that the whole geometry (assuming symmetry) has been depicted. For gas pressure values, see figure 33.c

- *Total stresses*

During the whole injection process (i.e. 5 years), the most notable increase in the horizontal total stress takes place in the surroundings of the injection point after, approximately, 6 months of CO_2 injection. This tendency matches the gas pressure evolution, which reaches its maximum value after that period of time. As seen in figure 47, horizontal total stress increases around 1.6 MPa in the injection point due to this process ($\Delta\sigma_h = 1.6\ \mathrm{MPa}$). As for vertical total stress, it evolves in a very similar way, but in this case the maximum increase is only 0.13 MPa in the injection point ($\Delta\sigma_v = 0.13\ \mathrm{MPa}$). Vertical stress at a point is basically controlled by the weight of geological media which lies above it, and so its value remains alomst constant regarless of fluid injection.

The asumption of a thin, laterally extensive reservoir allows to use the following analytical expression to estimate the horizontal poroelastic stressing:

$$\Delta\sigma_h = \alpha \frac{1-2\,\nu}{1-\nu}\,\Delta P \qquad (38)$$

where α is Biot's coefficient, ν is Poisson's ratio and ΔP is the increment of fluid pressure. In this case, Biot's coefficient is assumed to be equal to one while Poisson's ratio is 0.25, so expression (38) gives $\Delta\sigma_h = 0.67\,\Delta P$. The initial fluid (liquid) pressure of 14.8 MPa and the maximum pressure of, approximately, 17.4 MPa after 190 days of injection gives an increase of 2.8 MPa. Consequently, the horizontal total stress increment is estimated to be equal to 1.7 MPa, which is consistent with the results obtained from the numerical model.

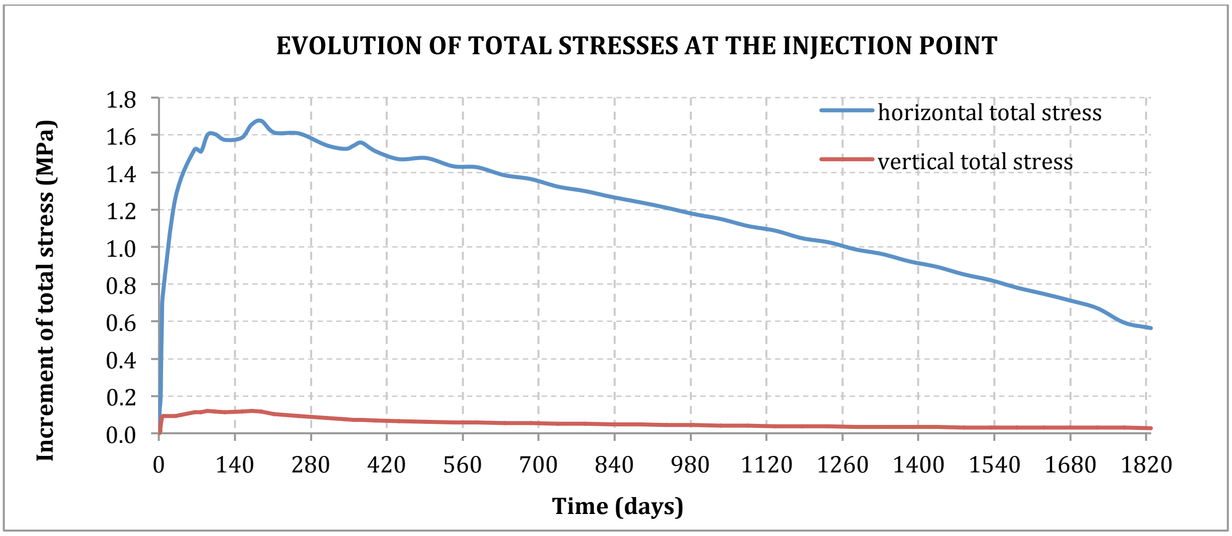

Figure 48: Increment of horizontal and vertical stress with time at injection point (not damaged ; compression positive).

- *Effective and net stresses*

Effective stresses decrease due to fluid injection. Since it is indeed the effective stress, and not the total stress, that actually acts on rigid particles, paying attention to its evolution is extremely important. Injecting an excessive amount of CO_2 in a geological formation would lead effective stresses to decrease dramatically. However, due to the fact that injection is performed at deep storage sites, initial effective stresses are quite high and so the changes triggered by fluid pressure build-up (with reasonable injection rates) are generally not big enough to cause serious problems, unless damaged areas are involved.

Actually, in this case, the existence of both gas and liquid phases makes it necessary to talk about net stresses rather than effective stresses. Nevertheless, since both phases tend to equilibrate and liquid pressure is kept well above gas pressure until the equilibrium is reached (figure 44), the concept of effective and net stress is almost the same in this case.

Figure 49 shows the horizontal effective stress colour map in the reservoir after three months of injections, which shows how the minimum effective stresses tend to concentrate in the surroundings of the injection point. The same can be said of the vertical effective stress (figure 42). It is important to note that the values of stresses in both figures are shown following the continuum mechanics criteria (compression negative) because this is how results are provided by CODE_BRIGHT and GID. In any case, the fact that effective stresses have a tendency to decrease explains the vertical uplift the media experiences.

As for effective stress evolution with time, figure 43 shows its tendency in the injection point. The graph shows how, indeed, the maximum decrease in effective stresses takes place after 6 months of injection, with an increment of, approximately, -1.3 MPa (initial value of 9.8 MPa) for horizontal stress and -2.7 MPa (initial value of 21.45 MPa) for vertical stress (compression positive). Since fluid pressure is the same in all directions and horizontal total stress increases more due to pressure build-up (figure 40), it is straightforward to see why vertical effective stress decreases more (the double, approximately) than the horizontal component.

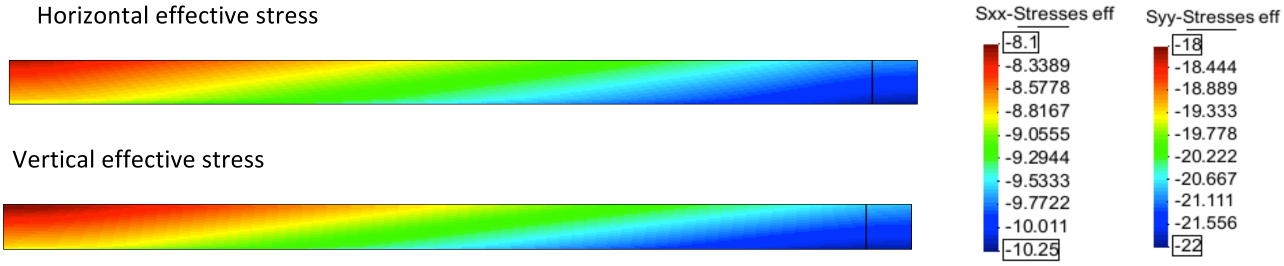

Figure 49: Effective stresses (MPa) in the reservoir after 6 months of injection. Note that in this image compressive stresses have negative sign.

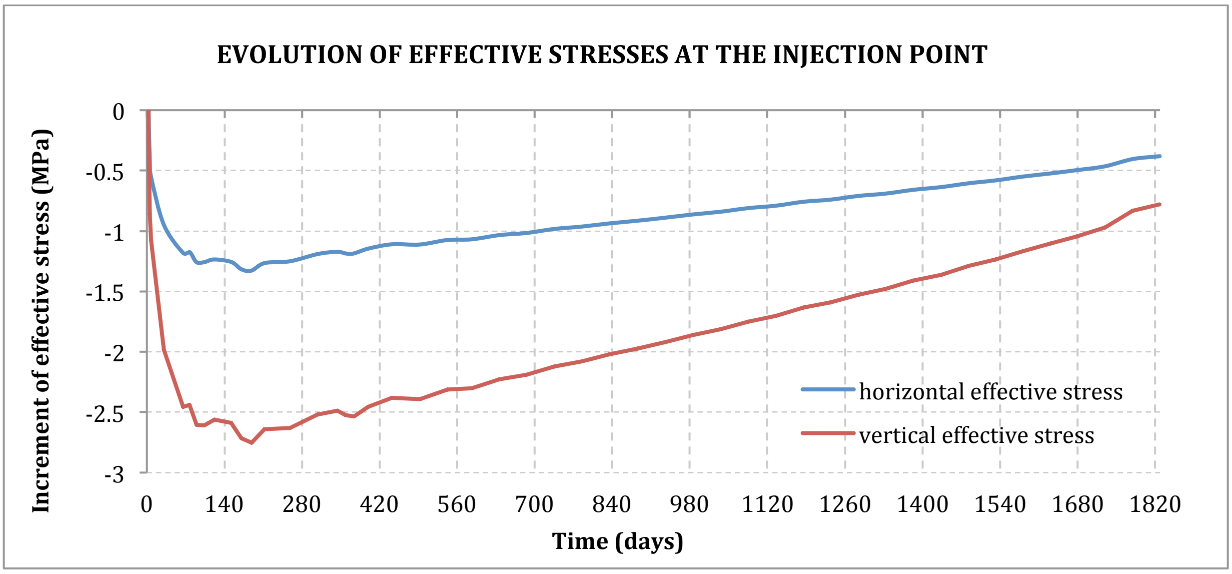

Figure 50: Increment of horizontal and vertical effective stress with time at injection point (not damaged ; compression positive).

6.2. Damaged storage site: fractured caprocks

- *CO_2 plume and gas pressure*

The upper caprock has now been modelled as damaged material, the supercritical fluid is allowed to move upwards in case that pressure build-up is big enough to trigger fracture opening. In this case, joints start to open from the beginning of the injection process (they already existed, despite being almost closed) and so the CO_2 plume soon penetrates the caprock and keeps moving until it reaches the upper aquifer.

As for pressure transient evolution, the tendency is again similar to that observed in the undamaged formation, but now values are slightly lower (figure 52). The fact that pressure values are lower than expected is an indication that the injected fluid is migrating from the reservoir. In the surroundings of the injection point, a maximum value of 16.3 MPa is achieved (7% less than in the undamaged case). Nevertheless, the decrease is almost unnoticeable, partly because the fluid was already allowed to move freely even when the caprocks were not damaged. Obviously, the difference would have been much bigger if the storage site had not been as extensive or the injection rate had been bigger.

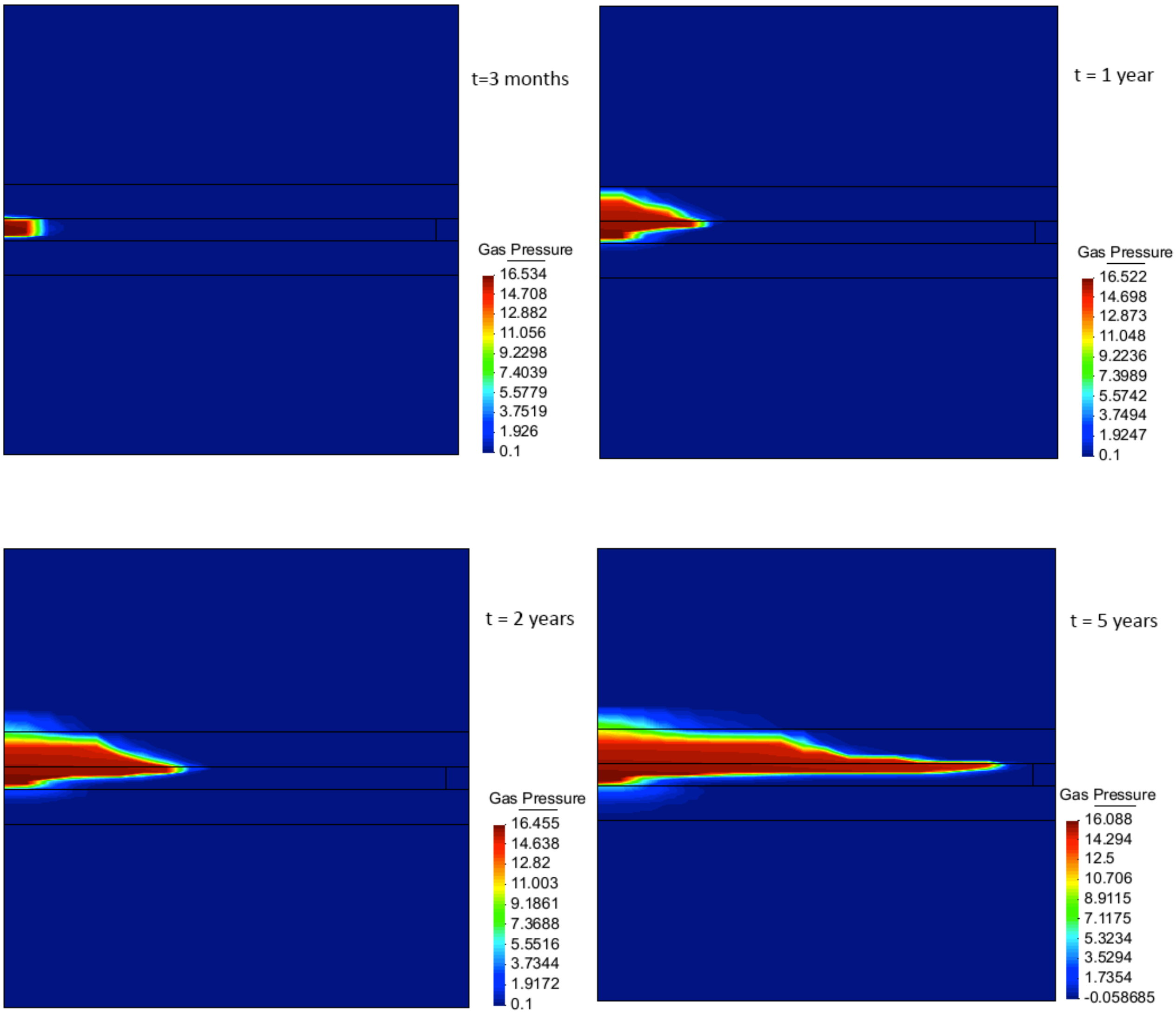

Figure 51: CO_2 plume and gas pressure (in MPa) at different stages of the injection process (damaged caprocks)

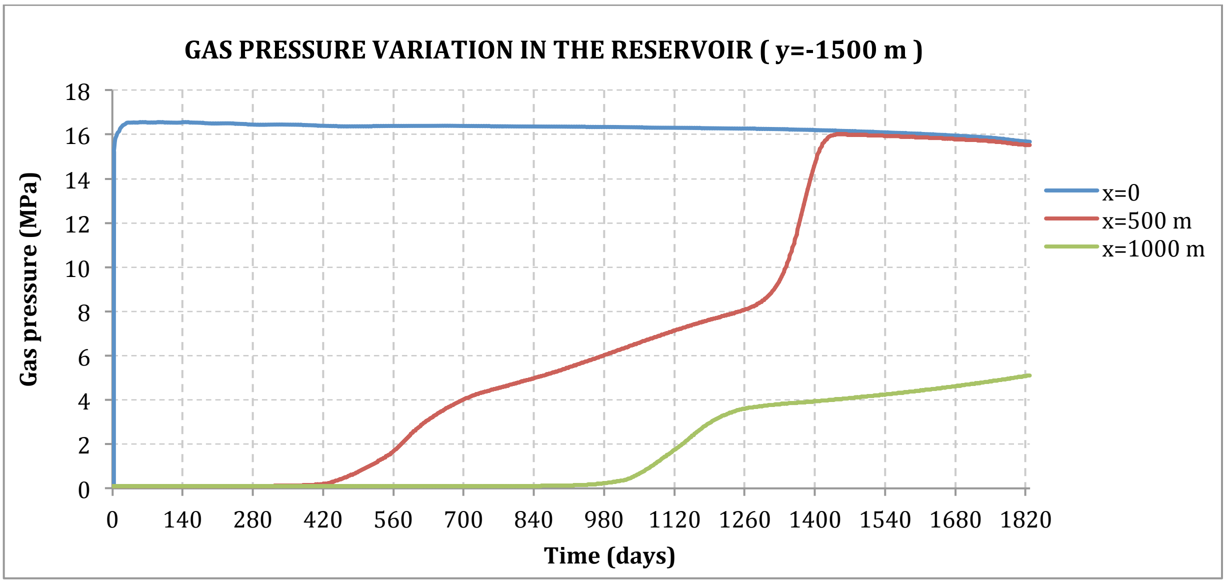

Figure 52: CO_2 pressure at three points located in the reservoir (damaged caprocks).

- *Permeabilty evolution*

The presence of fractures is directly related to permeability changes in the caprock, which is the main reason for fluid to migrate. Since fracture permeability depends on aperture and aperture depends on the deformation of the medium which has been defined by means of an elastic constitutive model, joints can be opened and closed with complete reversibility. Permeability values have been represented along the reservoir-caprock contact (figure 53). As it can be observed, permeability increases the most in the surroundings of the injection point, a fact that was already anticipated since it is indeed around that area where pressure build-up is bigger. Note how permeability increases very fast because fluid pressure also does. A maximum value of $4 \cdot 10^{-14}\ m^2$ is achieved at *x=0 m* (being *x* the horizontal distance to the injection point). This is a very important permeability change (more than 5 orders of magnitude) and clearly explains why the injected fluid migrates much more easily than in the previous simulation.

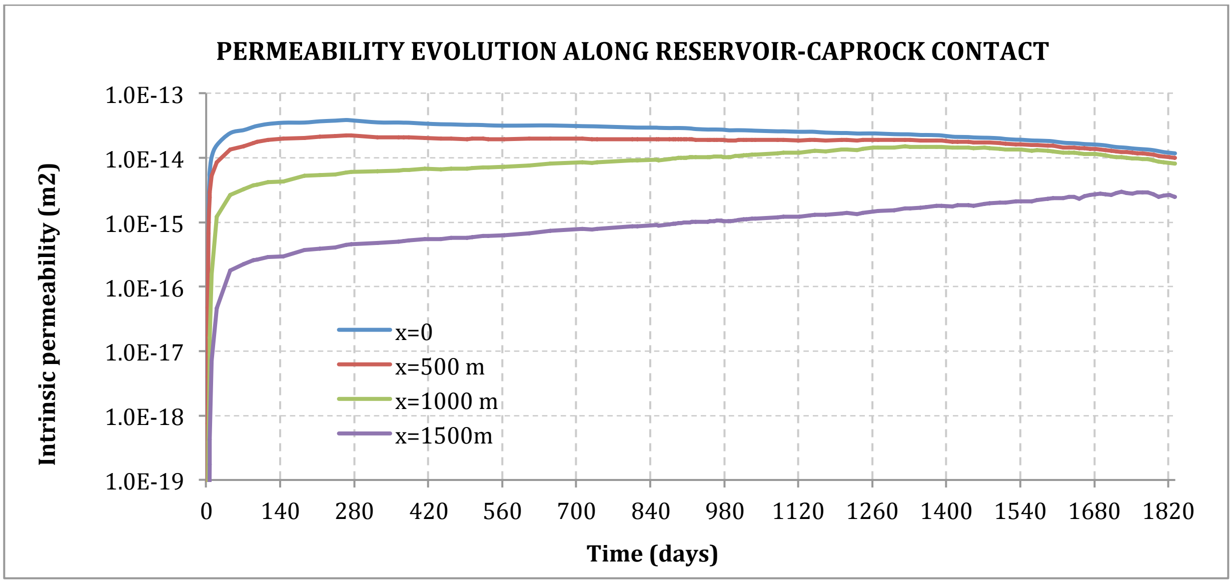

Figure 53: Permeability evolution at several points located in the reservoir-caprock contact

- *Liquid pressure and degree of saturation: capillarity*

As seen in figures 34 and 35, caprock shales have to experience much bigger suction forces compared to sandstones before noticeable desaturation takes place. This is true assuming intact material, but joint aperture affects capillary pressure as explained in Chapter 2:

$$\mathrm{P} = \mathrm{P}_0 \frac{\sqrt[3]{\mathrm{k}_0}}{\sqrt[3]{\mathrm{k}}} \frac{\sigma}{\sigma_0} \qquad (39)$$

where *P* refers to the capillary pressure necessary to start desaturation. Assuming constant surface tension and taking into account how permeability changes according to figure 53, we observe that the pressure necessary to desaturate the material (caprocks) is now much lower. Close to the injection point (*x=0*), it reaches a minimum of 0.014 times P_0 , being P_0 the initial value of P. This easily explains why shales are now able to desaturate with much lower suction forces. Figure 54 shows how *P* evolves with time at some points located in the contact between the reservoir and the upper caprock. Additionally, the colour map in figure 55 depicts the degree of saturation in the injection site at the end of the process (this is, after 5 years of injection).

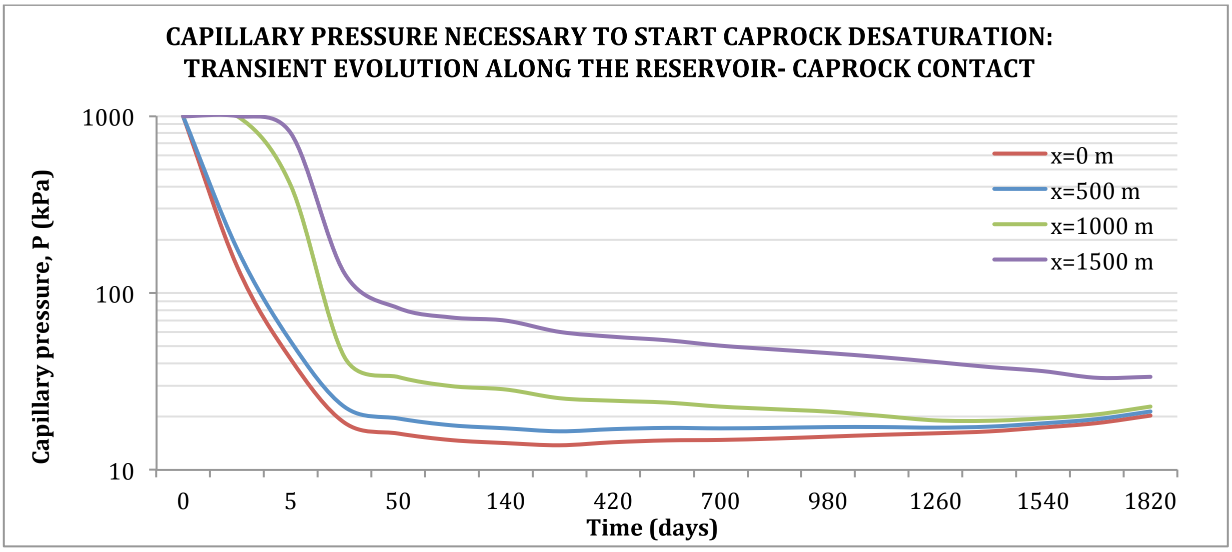

Figure 54: Transient evolution of the capillary pressure necessary to dessaturate shales, as observed along the reservoir-caprock contact.

It is interesting to note that, under damaged conditions, the retention curve of the caprock is no longer constant, but it depends on permeability (i.e. on joint aperture) and, thus, it is a function of space and time. This makes it impossible to define only one retention curve capable of describing how the whole rock desaturates with capillary pressure. Nevertheless, it is possible to set boundaries, this is, retention curves for minimum and maximum permeabilities. Following this idea, figure 55 shows two retention curves: one for the undamaged caprock (i.e. minimum, almost zero, fracture aperture) and another for the damaged caprock, assuming a maximum possible joint aperture (or permeability) according to the results presented in figure 53. All other retention curves will lie between these two. Such variations make the desaturation process less predictable *a priori*, but it still follows the expected tendency. It is important to note how the variation of the degree of saturation in space seems less pronounced or abrupt in the damaged caprocks, in contrast with the reservoir where a more sharp interface is observed. This fact can be explained by the evolving retention curves, which are now different from the original ones and make the material desaturate differently.

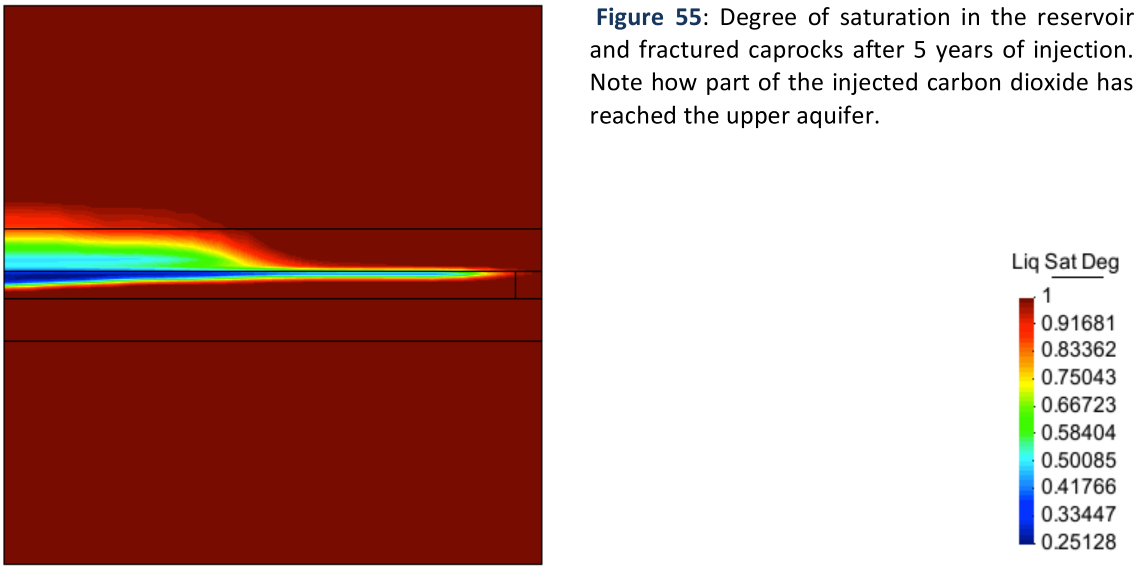

Figure 55: Degree of saturation in the reservoir and fractured caprocks after 5 years of injection. Note how part of the injected carbon dioxide has reached the upper aquifer.

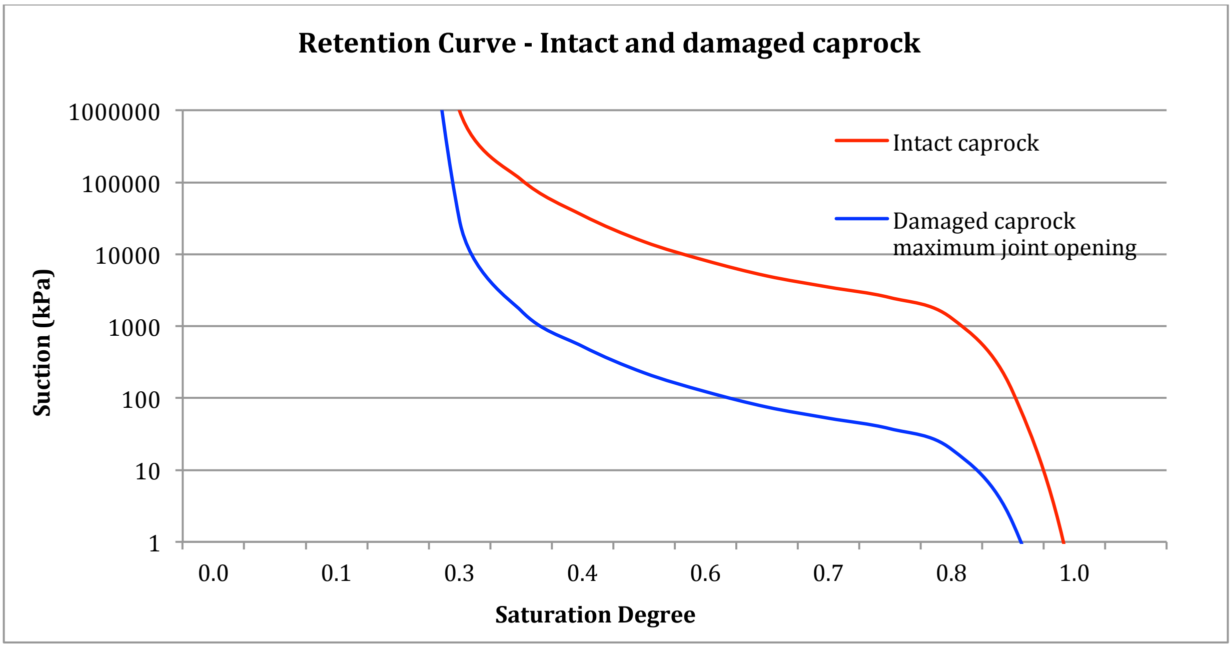

Figure 56: Retention curve of caprock material assuming intact and damaged (maximum aperture) conditions.

- *Vertical displacement*

While gas migration, and subsequent reduction of pressure build-up, should be associated to smaller values of vertical uplift, simulation results show that displacements are actually much bigger than expected. This is because gas migration not only involves pressure losses but also gas spread through the upper caprock which, additionally, is now assumed to be more deformable so as to simulate damaged conditions.

Vertical displacements along the reservoir-caprock contact show that these values are similar to those obtained for the undamaged case during the first weeks of injection. Differences are not big because pressure build-up is only slightly smaller than in the previously simulated case. Once the injected fluid reaches and penetrates the caprock, this tendency starts to change. The maximum vertical uplift at that point assuming damaged conditions takes place after 3.5 years of injection. Figure 57 shows vertical uplift along the reservoir-caprock contact at different times assuming damaged conditions. Observation of vertical effective stress helps understanding vertical uplift behaviour in both situations and the reasons for their different evolution.

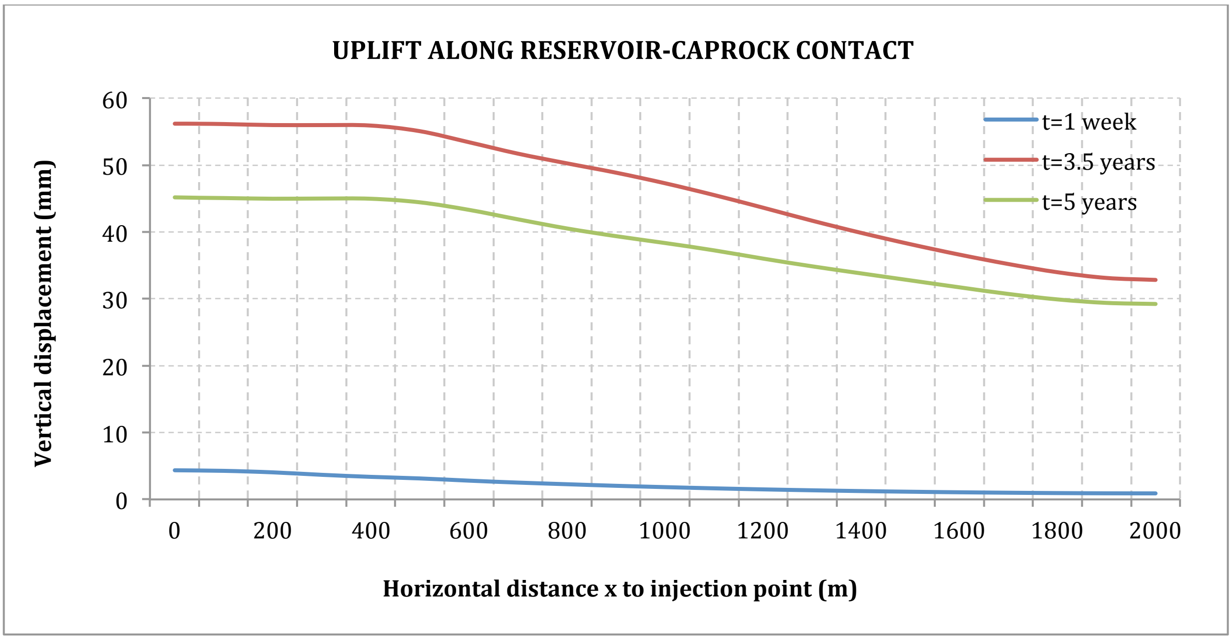

Figure 57: Vertical uplift along the reservoir-caprock contact assuming fractured caprocks.

- *Total stresses*

In the reservoir, a similar tendency to that commented in 6.1 is observed, but the increase in horizontal total stresses is smaller due to gas migration ($\Delta\sigma_{h,max} = 0.8 \text{ MPa}$). Additionally, stresses in caprock strata are much more affected by injection because CO_2 is now allowed to move through shale fractures. Although the maximum increment of total stresses is still observed in the injection point, stress evolution in reservoir and caprocks are now very similar to each other.

- *Effective stresses*

The relationship between vertical and horizontal effective stress shows that vertical stress is the one that decreases the most ($\Delta\sigma_v = -1.6 \text{ MPa}$). As mentioned, it is interesting to observe how a different effective stress distribution affects vertical displacement. Figure 58 shows vertical effective stress evolution at three points, all of them on the symetry axis and in the middle of the reservoir and caprock layers, respectively. As it can be seen, caprocks and reservoir are affected in a very similar way, something that does not happen in the not damaged scenario, where effective stresses in the caprocks remain almost constant because fluid is not allowed to penetrate them. This explains why vertical uplift is now bigger than it was when caprocks were perfectly intact: effective stresses increase more in the caprocks when they are fractured and so vertical deformation globally increases.

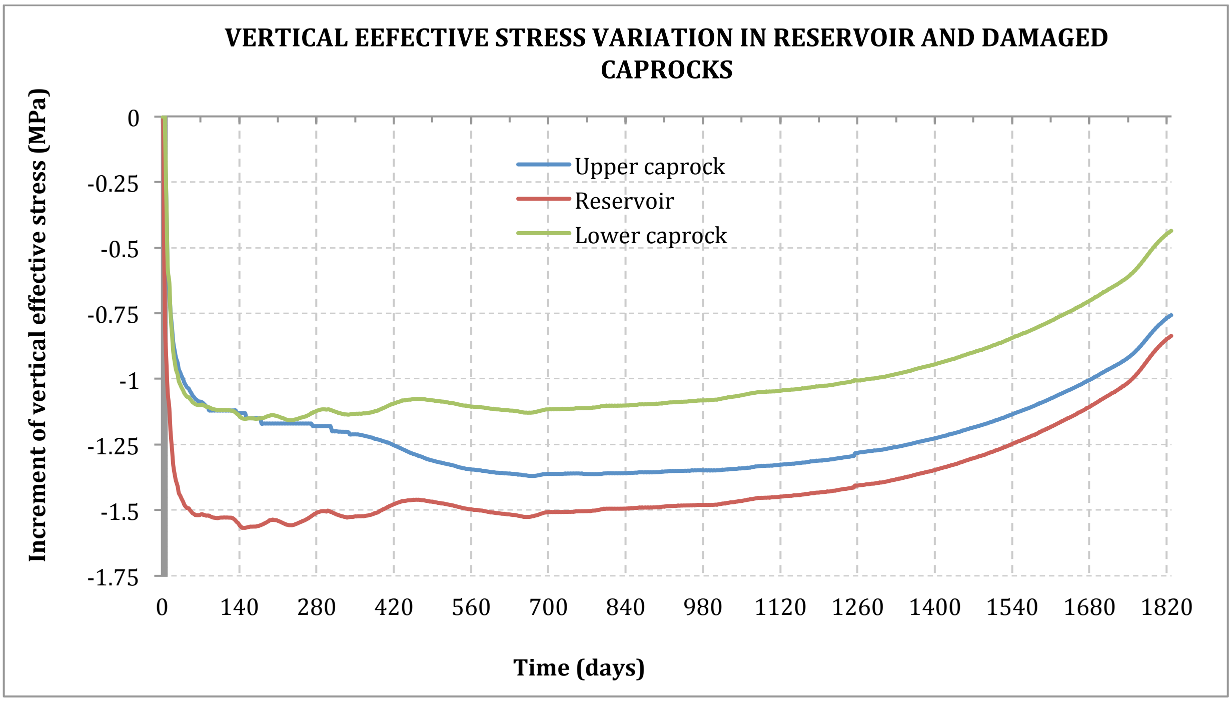

Figure 58: Vertical effective stress variation at three points located on the symmetry axis and within the upper caprock, reservoir and lower caprock strata.

6.3. Damaged storage site: fault

- *CO_2 plume, fluid pressure and degree of saturation*

During the first year and a half of injection the CO_2 plume behaves as described in 6.1. Although the fault first acts as a barrier (having an initial permeability 3 orders of magnitude lower than the surrounding sandstones), the effect is almost unnoticeable. Once the CO_2 reaches the fault zone, the fluid starts to migrate upwards due to the presence of embedded joints in the finite elements. At the same time, the injected fluid keeps moving horizontally, and only part of it follows the newly opened vertical path. Initially, a tendency to move through the fault rather than reservoir is observed, which can be explained by the effect of buoyancy and the fact that the vertical feature is directly connected to upper strata. Figure 59 shows the carbon dioxide plume (as well as gas pressure) at the end of the injection process.

The maximum CO_2 pressure values are almost identical (only slightly higher) to those obtained in the intact scenario, reaching 17.7 MPa in the injection point after 6 months of injection. Though not very pronounced, a slight pressure decrease can be observed after 1.5 years (550 days), which is the time when the injected fluid starts to penetrate the fault zone (see figure 60). The slight decrease in pressure at the injection point can be explained by fracture opening, which allows the gas to migrate upwards through the 20-metre-wide vertical fault. Nevertheless, the 500 meters that separate the source point and the fault attenuate this effect.

It is also interesting to observe how some relevant hydraulic variables evolve along the fault (figure 61). Two time steps have been chosen: 1.5 years (i.e. 550 days), because it is the time when the injected fluid starts to move through the fault zone, and 5 years, which is the end of the process. CO_2 and liquid (water / brine) pressure reach their maximum increment near the reservoir after 1.5 years of injection, and then start to spread upwards as the injected fluid migrates (until t=5 years). Note how injection affects liquid pressure along the whole fault zone even when CO_2 has only started to move through it. This fact makes it more difficult for the fault zone to desaturate, because the difference between CO_2 and liquid pressure is sometimes not big enough. Nevertheless, the effect of fluid moving upwards is obvious in figure 61.

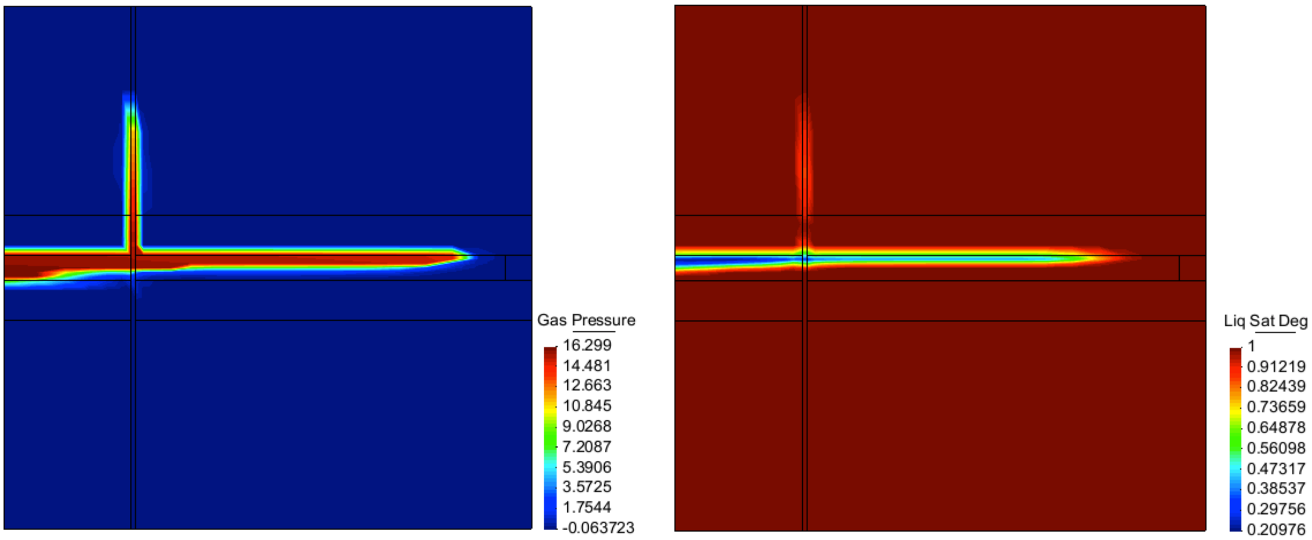

Figure 59: CO_2 plume (pressure and degree of saturation) after 5 years of injection.

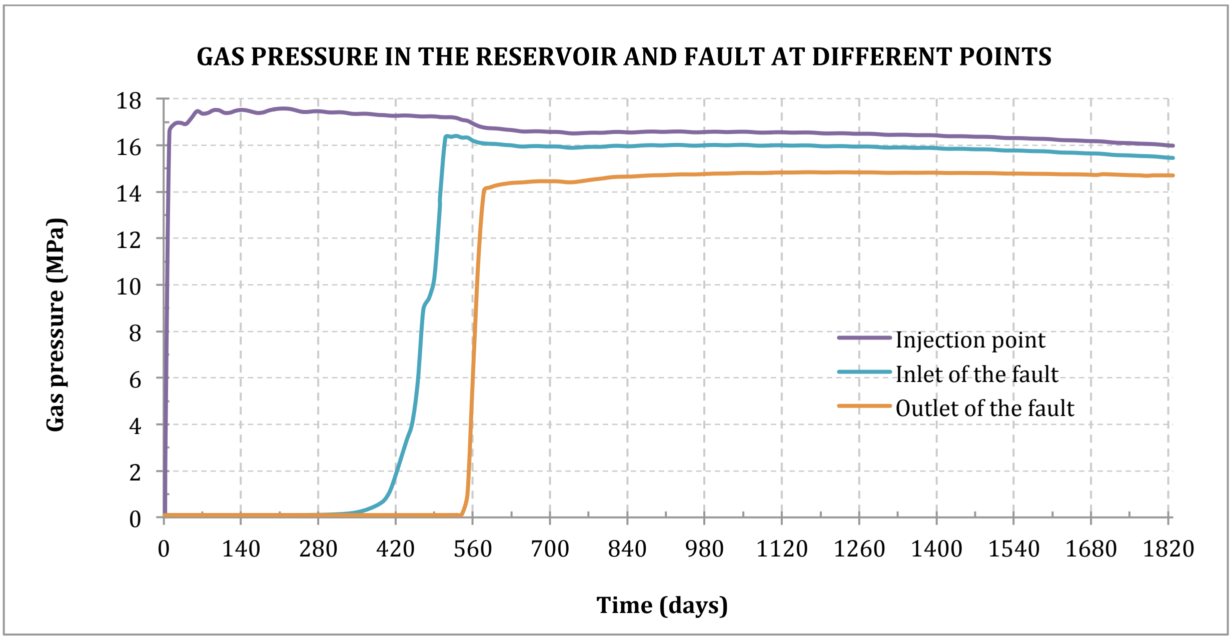

Figure 60: Gas pressure evolution at the injection point and the inlet and outlet of the fault in the upper caprock.

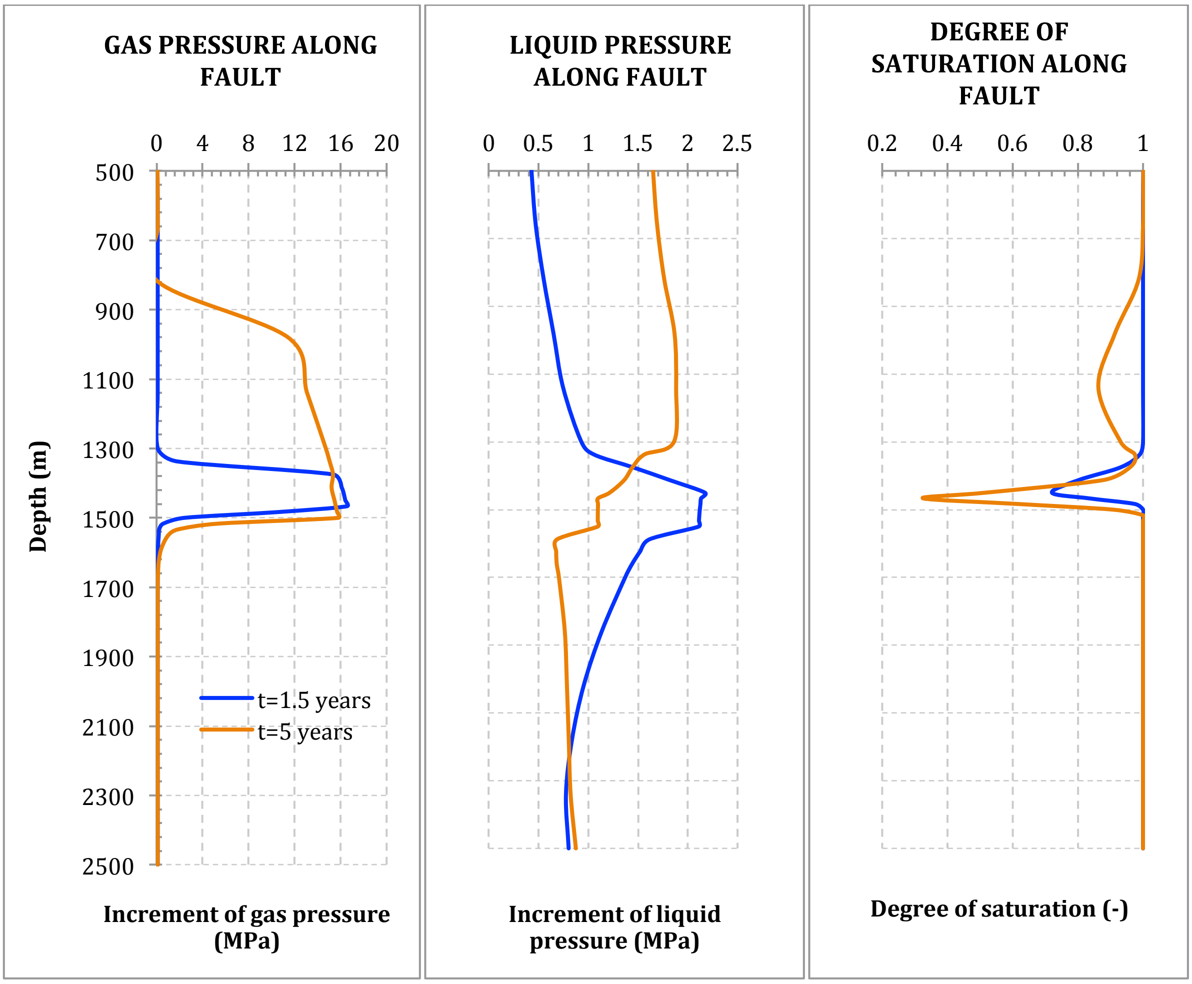

Figure 61: Gas, liquid pressure and degree of saturation along the fault after 1.5 and 5 years of injection.

- *Permeability and formation of preferential paths*

Joints have been embedded in the elements that simulate the vertical fault, so it is interesting to observe how permeability evolves in that zone. Fracture opening in this case is crutial to explain fluid migration to upper strata. Two points (one being the inlet and the other the outlet of the fault in the upper caprock) have been considered. Figure 62 shows permeability evolution (increment) with time in these two points.

Note how permeability in the inlet point starts to increase from the beginning of the injection. In other words, the effect of injection is noticeable even before the CO_2 plume reaches the fault. Assuming the properties we already mentioned in Chapter 5, permeability increases by more than 3 orders of magnitude. It is interesting to observe the sudden increase after 1.5 years of injection (when the injected fluid reaches the inlet point) and then an abrupt decrease which can be explained by the slight drop in pressure, as depicted in figure 60. Permeability depends on joint aperture raised to the third power, so a slight change in the strain state may have a much more noticeable effect on permeability. It is important to note that the permeability of the fault is kept above that of the reservoir during the central months of injection, which explains the initial tendency of the fluid to move upwards rather than continue its way through the reservoir (figure 63, t=1.5 years).

As for the outlet point, it is straightforward to see how permeability increases at a higher rate after CO_2 has reached the fault (figure 62). Since the elements that make up the fault zone near the outlet point have a permeability an order of magnitude higher than that of the surrounding aquifer, the fault becomes a preferential path for fluid migration. By modeling a fault like this (i.e. with embedded joints in finite elements) we have been able to simulate anysotropy of permeability and the formation of preferential paths. Thus, CO_2 has a clear tendency to keep moving upwards through the fault rather than migrate laterally (figure 63, t=2 years). Had the fault zone been equally pervious than the surrounding aquifer, the fluid would have also spread laterally due to the inexistence of a clearly defined preferential path (see figure 64)

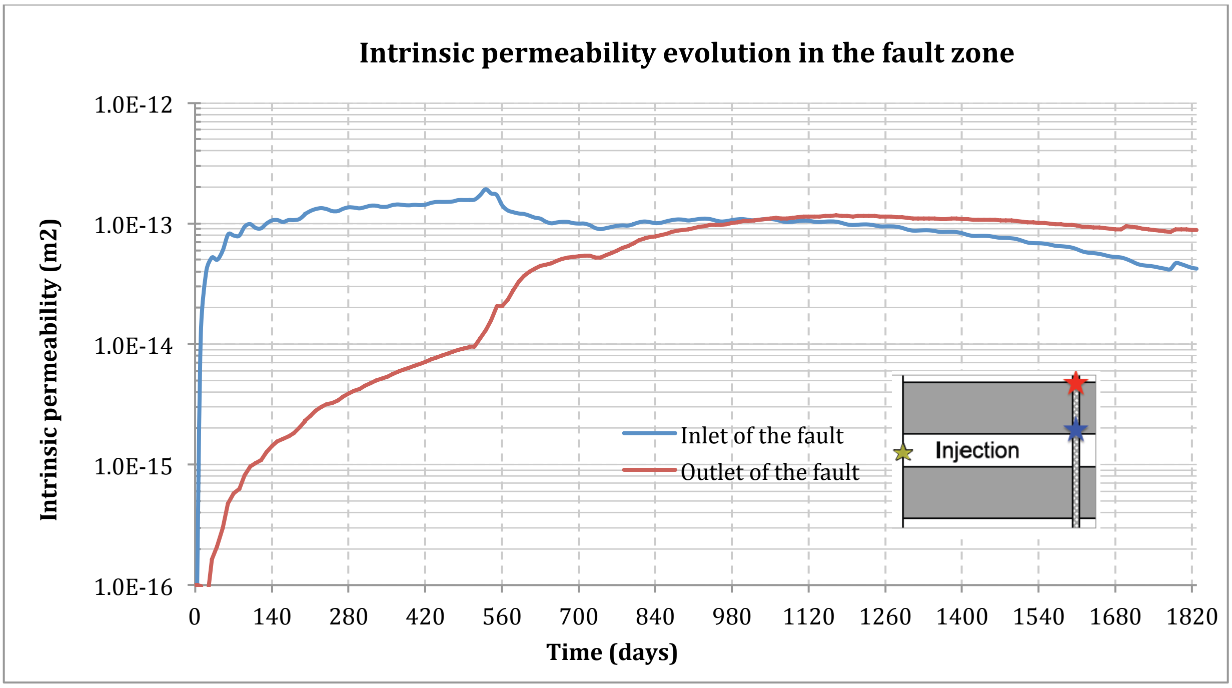

Figure 62: Permeability evolution at the inlet and outlets of the fault in the upper caprock

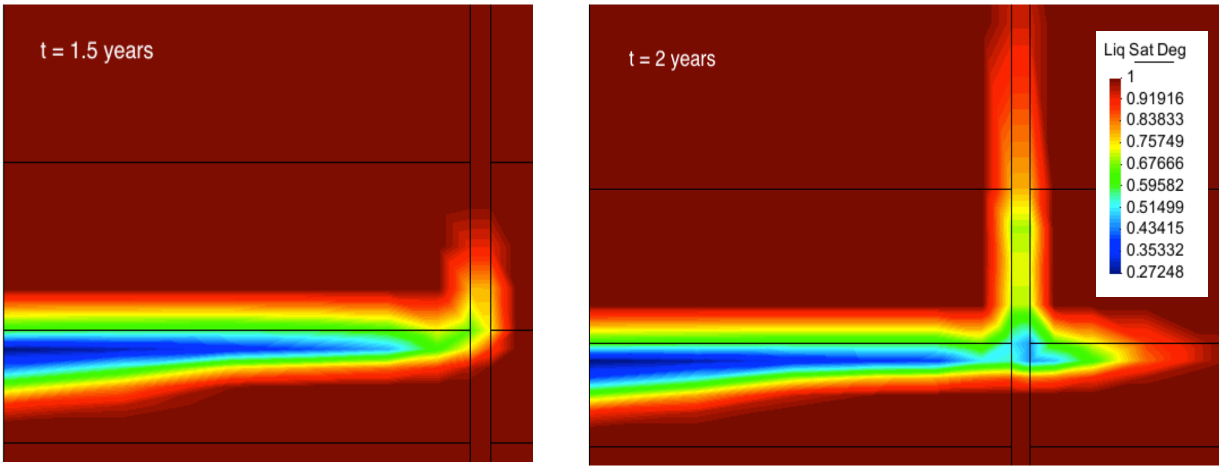

Figure 63: Migration of the injected fluid assuming s=0.5 to compute joint aperture. Note the formation of a vertical preferential path due to joint aperture in the fault zone.

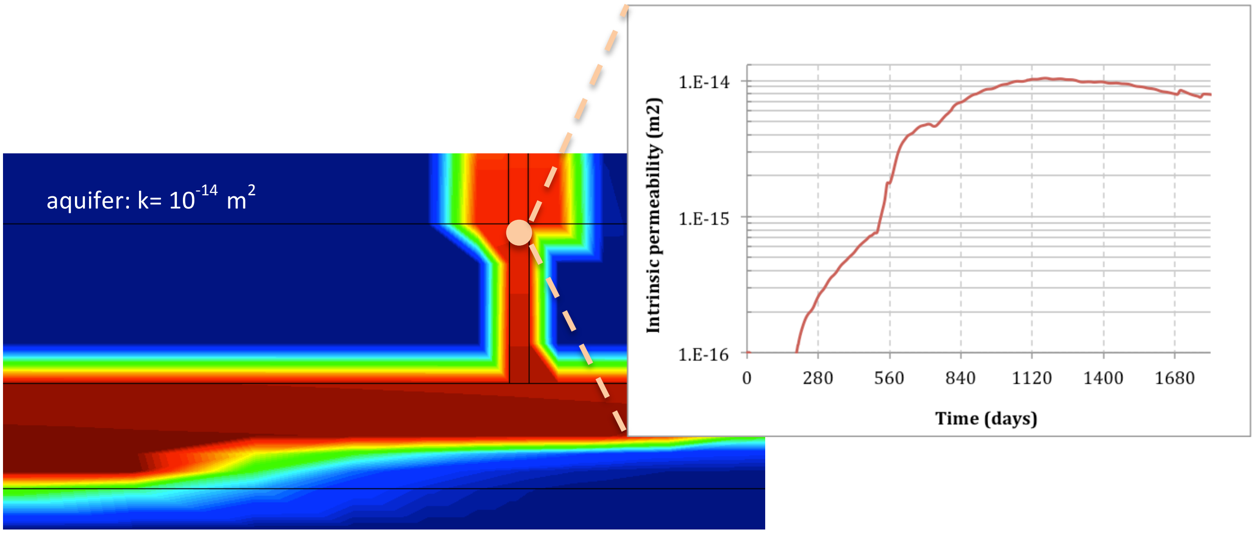

Figure 64: CO_2 plume in the surroundings of the outlet point assuming s=0.15. Note that, in this case, fault permeability reaches the same value as the aquifer and so fluid tends to spread laterally too.

- *Vertical displacement*

The behaviour is similar to that observed in 6.2 (i.e. assuming damaged caprocks). This result highlights how important it is to keep the injected fluid confined within the reservoir to avoid a big increase in vertical displacements. Connection between the reservoir and surrounding strata (either due to caprock damage or because of the existence of a fault zone) causes fluid pressure to increase in a much more extensive area. As a consequence, effective stresses decrease in a much larger zone, and so the deformation of the geological media is much more noticeable than that observed in the undamaged case (almost three times bigger in the reservoir-caprock contact).

- *Total and effective stresses: risk of fault reactivation*

The fact that the injected fluid penetrates the fault zone makes it necessary to verify how stresses along it evolve until the injection well is shut down. In previous examples, the evolution of stresses at the most affected zones (i.e. near the injection point) was already presented and discussed, so now our main interest lies in the fault itself. As mentioned, the existence of a fault zone (although inactive) increases the risk of triggering seismic activity because the hydraulic alterations caused by fluid injection may lead to fault reactivation and subsequent slip.

Figure 64 depicts horizontal total and effective stress variation along the fault at two different time steps (1.5 and 5 years). In this case, since the fault has been assumed to be completely vertical, horizontal stresses are perpendicular to the fault direction, and thus the correspondence between x,y stresses and the normal stress (assuming the existence of a vertical discontinuity plane) can easily be established. It is interesting to note the similarities between the stresses and fluid pressure profiles, which is an indication of the hydro-mechanical coupling caused by the injection of CO_2. As expected, total stress increases and effective stress decreases as a result of fluid injection, being the difference between both increments equal to the increment of fluid (liquid) pressure. Note that the maximum decrease in effective normal stress (-1.2 MPa) is reached at the inlet of the fault in the upper caprock, which becomes the most critical point.

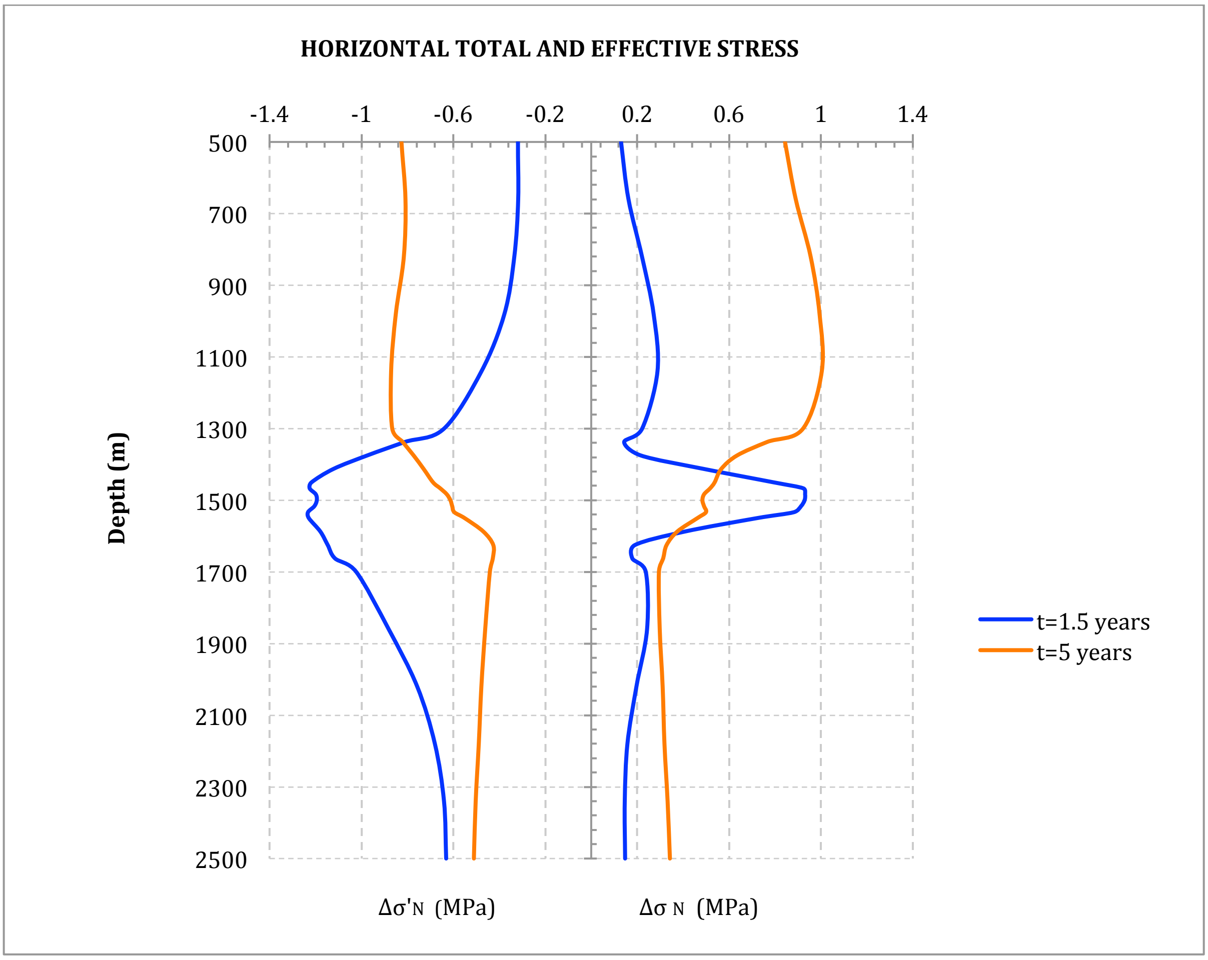

Figure 65: Total and effective horizontal stress increment along the fault. They are equivalent to the normal stresses acting on the fault is we consider it to be a discontinuity plane.

Effective normal stress drops to $\sigma'_N = 8\,\mathrm{MPa}$ in the inlet point after 1.5 years of injection, which represents approximately a decrease of 15 % with respect to the initial stress state. Using the Mohr-Coulomb criterion to compute shear strength of a discontinuity plane (see Appendix A for more information) and assuming a cohesionless fault with a friction angle of $\varphi = 23º$, close to the lower limit for faults which may contain clay minerals or gouge (Wibberley and Shimamoto, 2005), the critical shear stress (τ) for slip occurrence is equal to 3.7 MPa. Since fluid injection barely has any effect on principal directions (which are stil mainly vertical and horizontal), shear stresses are too small to trigger fault slip assuming a vertical discontinuity plane. One has to consider, though, that the assumption of a vertical fault has been done for the sake of simplicity, but a great variety of orientations could exist.

Anyway, the fault has been simulated not as a single plane but as a whole damaged zone which could be reactivated if failure conditions are met at some particular point. Figure 66.c shows how, with the new effective stress state (after 1.5 years of injection) and assuming the aforementioned Mohr-Coulomb strength parameters, shear failure conditions are met at the inlet of the fault. This indicates a high potential for shear slip to occur along fractures with dip angles close to 60 º, thus causing reactivation of already existing fractures or propagation and formation of new ones. In any case, it is straightforward to see that if fluid is allowed to penetrate the fracture zone, a high potential for fault reactivation due to shear failure exists, a situation commonly associated to earthquake occurence.

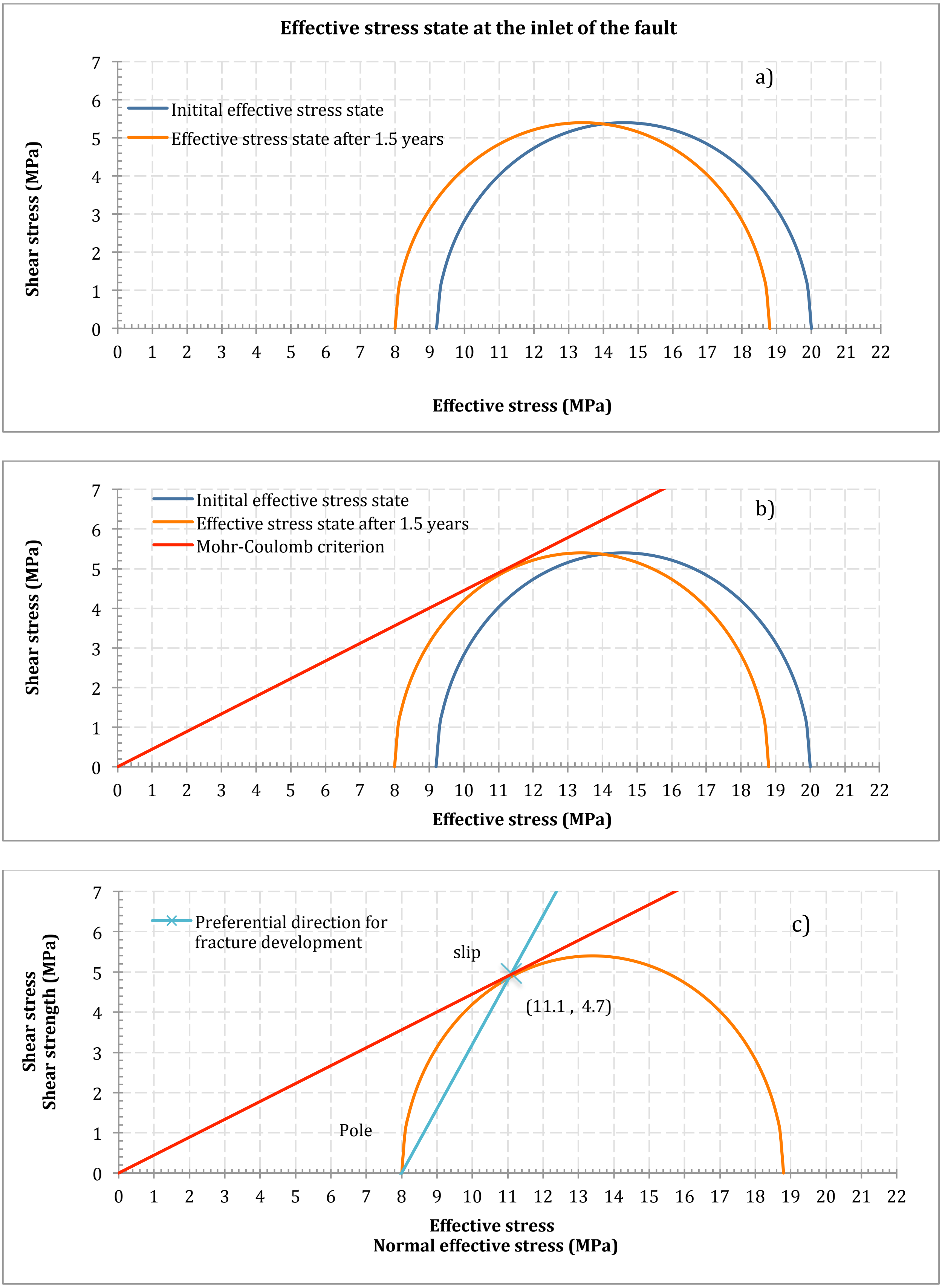

Figure 66: a) Effective stress state at the inlet point: initial and after 1.5 years ; b) Effective stress states and Mohr-Coulomb criterion for fault material with $\varphi = 23º$; c) Mohr circle pole and preferential direction for fracture development.

6.4. Damaged and undamaged injection sites: result comparison

This short section is aimed at summarising the most relevant results which explain the differences between each simulated case. Results are not going to be presented in detail here since a thorough discussion of each scenario has already been made throughout last section.

- *Evolution of CO_2 plume*

Figure 67 compares the position of the CO_2 plume in each scenario after 5 years of injection. In all cases the injected fluid tends to spread laterally but also to migrate to upper strata if the sealing material is not pervious enough or can potentially be damaged by fluid overpressures. While intact caprocks offer perfect sealing, a damaged material (with the same initial properties) can easily become highly-conductive by reactivation of already existing (but closed) fractures. The plume can thus move easily through the initially impervious caprock and reach the upper aquifer. If a vertical damaged feature (for instance a fault) is considered, it becomes a clearly defined preferential path for fluid migration.

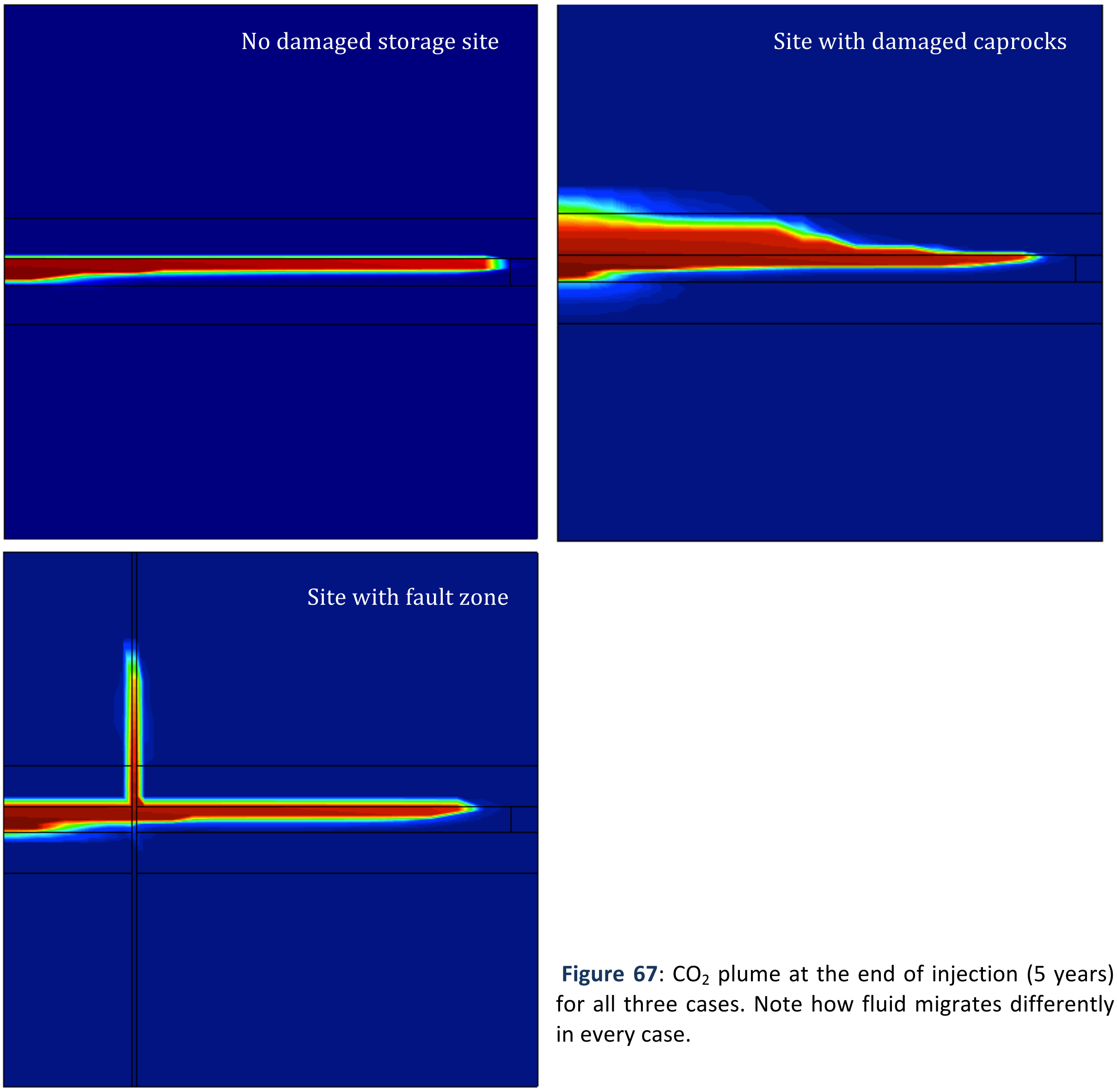

Figure 67: CO_2 plume at the end of injection (5 years) for all three cases. Note how fluid migrates differently in every case.

- Pressure build-up at the injection point

In general, the tendency looks similar in all three scenarios, but a close look at how liquid pressure increases (figure 68) shows that the damaged caprocks scenario is the one which leads to smaller overpressures because the injected fluid is allowed to flow more easily from the beginning. The overpressures for the other two scenarios (intact and fault zone) are very similar until the plume reaches the fault. This is the instant in which permeability at the inlet of the fault in the reservoir increases sharply and fluid is allowed to migrate with more ease, thus causing overpressures to decrease.

- Desaturation of upper aquifer (fluid migration)

Figure 69 shows the degree of saturation along the caprock-upper aquifer contact after three years of injection (approximately, when dessaturation reaches its maximum in all three scenarios). This is an indication of how CO_2 migrates and reaches the upper aquifer. Note how in the undamaged case the injected fluid does not reach this stratum whatsoever, while in the other two cases (damaged storage sites) CO_2 does reach the aquifer and makes the degree of saturation drop until 0.85 (damaged caprocks) or 0.7 (fault).

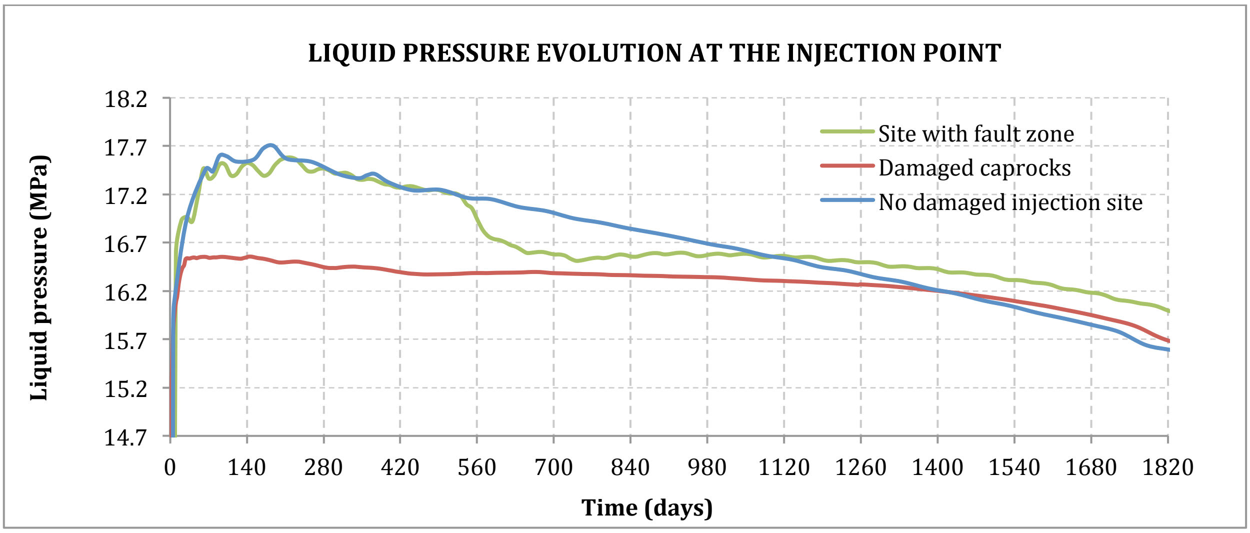

Figure 68: Liquid pressure increment for all three scenarios.

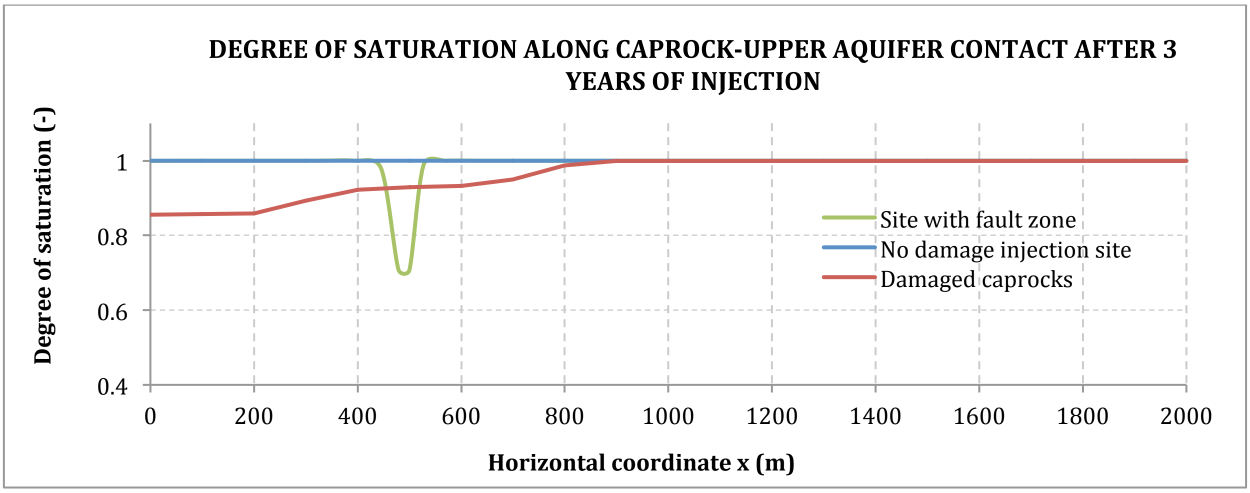

Figure 69: Degree of saturation along the caprock-aquifer contact after 3 years of injection.

- *Vertical displacement and effective stress*

As mentioned in 6.3, damaged caprocks lead to much bigger vertical displacements (figures 70 and 71) because the aperture of highly-conductive paths makes fluid overpressure affect caprocks and upper aquifer too (figure). Thus, vertical effective stresses decrease in a much larger area and so, globally, vertical displacements are bigger. While damaged caprocks lead to a decrease in effective vertical stress within them (see figure 72), the presence of a fault has a much more noticeable effect on the upper aquifer. In this last case, the effect of fluid plume reaching the fault inlet (i.e. t=1.5 years) can be clearly noticed too. Additionally, it is interesting to observe how a slight double-lobe effect as that commented in Chapter 4 appears around the fault.

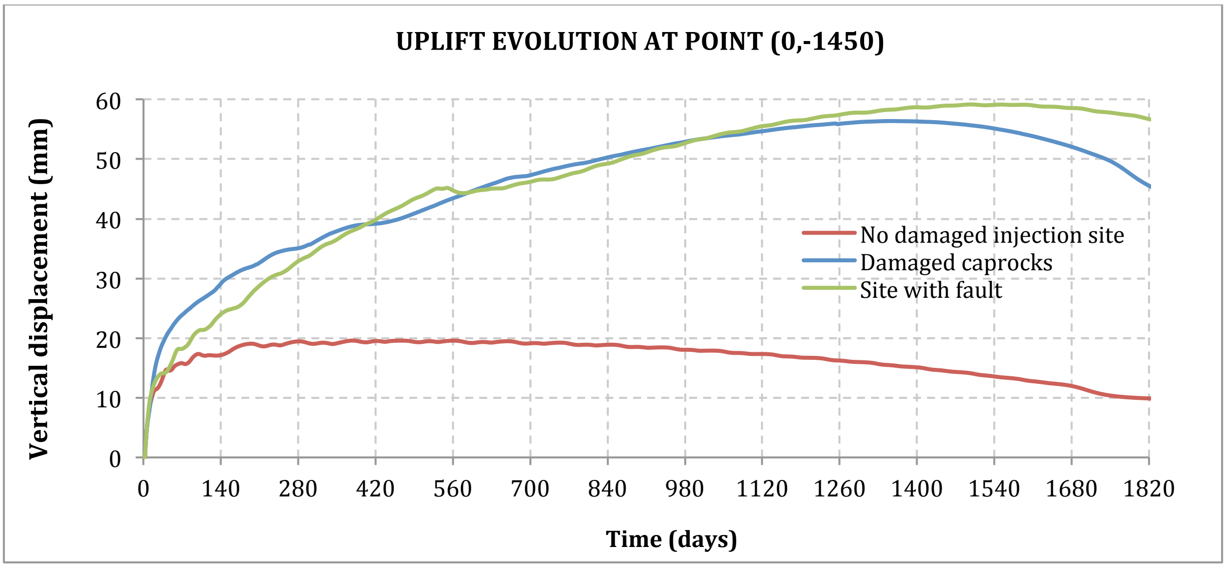

Figure 70: Vertical displacement evolution in the contact between reservoir and upper caprock.

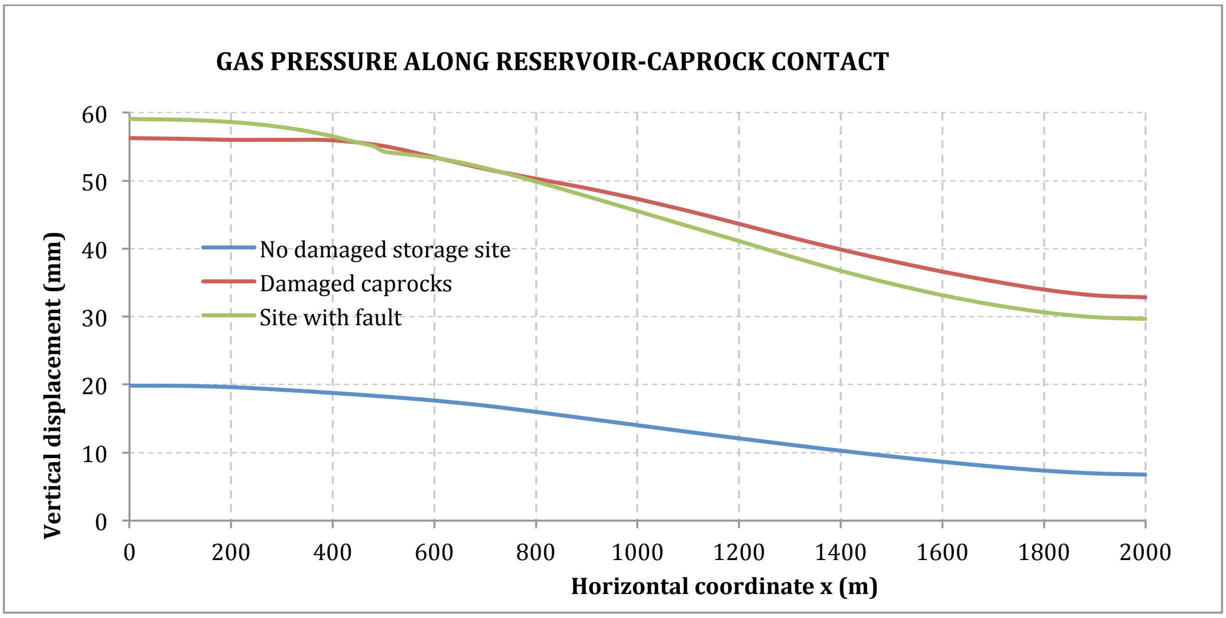

Figure 71: Profile of maximum uplifts along reservoir-caprock contact.

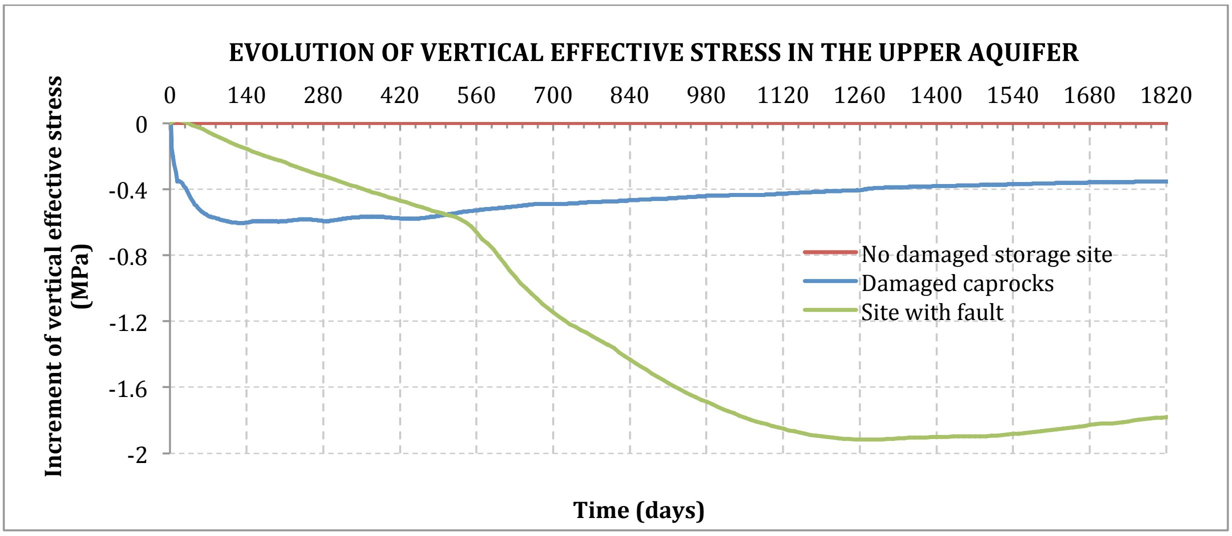

Figure 72: Transient evolution of vertical effective stress at a point located in the upper aquifer (0,-900).

- *Caprock failure and fault reactivation potential*

The potential for shear failure has only been commented in the third scenario to study the possibility of reactivating a pre-existent fault due to fluid overpressure. However, failure conditions can also be met within the damaged caprocks (scenario two). Actually, shear failure is quite likely to happen if the same strength parameters (for instance, zero cohesion and a friction angle of 23º) are assumed. Finally, although caprocks in the first scenario have been assumed not to be damaged the possibility of fracture formation exists. Nevertheless, as seen in figure 50, horizontal effective stress decreases less than the vertical one, hence the deviatoric stress decreases and failure conditions are not met in the reservoir-caprock contact despite a global decrease in effective stress values (compression positive).

6.5. Concluding remarks

By observing the different results obtained from the assumption of damaged and undamaged conditions of a typical carbon storage site, the following points can be concluded:

- A reservoir capped by not-damaged sealing materials offers optimal safety conditions for carbon storage. Under reasonable fluid injection rates, overpressures are not big enough for failure conditions to be met at the reservoir-caprock contact, and so CO_2 is expected to remain confined within the reservoir limits.

- The presence of fractures in the caprocks leads to big permeability changes from the beginning of injection and so fluid migrates upwards. When a fault modelled as a 20-metre thick fracture zone is considered, it becomes a preferential path for fluid migration to such an extent that fluid may have a tendency to keep moving upwards rather than spread laterally. Plume behaviour depends strongly on permeability enhancement.

- Damaged caprocks or the presence of fault zones make fluid overpressure affect wider areas, not only the injection reservoir. Thus, it is important to account for the whole site, since the most critical conditions could be met in upper strata and not necessarily in the reservoir. An already existing fault could easily be reactivated due to shear slip caused by fluid penetration.

CONCLUSIONS

Throughout this work, the topic of Carbon Capture and Storage in geological media has been treated from a global perspective, focusing on the several aspects that such projects involve. The review of information of different nature has allowed the author to present the concept of CCS in its multiple dimensions, starting with the environmental reasons that explain the implementation of such techniques and ending with the presentation of a numerical model to put into perspective their main effects on geological media.

CCS has been pictured as a potential solution to fight against global warming, but special care has been put in pointing out that its implementation requires not only thorough previous analysis but also exhaustive monitorisation during the whole injection process. Public concern always arise when dealing with activities which involve a certain amount of risk for safety and public health. The presence of undetected damaged zones in the storage site, in particular, is a major concern, especially because reactivation of fractures and faults may trigger ground water contamination as well as seismic events. The existence of such potential risks has been considered from the beginning, but also the necessity of providing accurate forecasting as a key tool to prevent unexpected events from happening. In this sense, the importance of numerical models has been emphasised since they are an essential tool to simulate phenomena that, otherwise, would be difficult to predict.

The review of a real case has allowed to put into perspective the intimate relationship that exists between fluid overpressure and surface uplift, as well as the key role that reactivation of fracture zones may play in the whole process. The particular aspects of the In Salah injection project have been explained and simulated in a simplified way using CODE_BRIGHT, in an attemp to understand the initially unexpected formation an uncommon double-lobe uplfit. Several concluding remarks have already been presented in the chapter devoted to the project in question. As a summary of them all, it can be concluded that the opening of a highly-conductive vertical path has allowed the injected fluid to migrate upwards, thus causing the fracture zone to expand laterally as a result of fluid overpressure. This, along with the slight decrease in pressure build-up rate in the surroundings of the fracture zone inlet point, can succesfully explain the unusual deformational behaviour observed on ground surface. The fracture zone height issue has been adressed more cautiously accounting for several simplifications which have been made. Nevertheless, the simulated uplift values match the InSAR detected ones quite accurately during most part of the process. The results suggest that the fracture zone does not reach the upper aquifer.

Finally, the simulation of a more general reservoir-caprock environment, typical storage sites in CCS projects, has been useful to analyse the effect of fluid overpressure on geological formations from a more global perspective. In particular, the potential for fluid migration and fault reactivation has been studied assuming three different scenarios. Fractures have been simulated by embedding joints in some finite elements. While fluid overpressures caused by normal injection rates have not shown to be big enough to damaged intact caprocks, the presence of very small aperture (almost closed) fractures have led to the formation of highly-conductive preferential paths which, in case they exist, may also reactivate faults and hence trigger seismic events.

All in all, this work has allowed the author to present Geological Carbon Storage as a tool which may play a key role in reducing the amount of CO_2 emitted to the atmosphere, but also as a set of techniques which may have a big impact on the surroundings of the storage site. Carbon storage projects may become more popular in the future, but, to achieve public acceptance, developing accurate methods to simulate and, thus, forecast, the potential risks that such underground activities entail is essential.

Future research

The large amount of different aspects that Geological Carbon Storage entail makes it an interesting field of research that can be extrapolated to many other projects which involve the injection of fluids underground. For instance, injection of water for the extraction of geothermal energy or supercritical fluid injetion to enhance oil recovery are examples of situations where overpressures may play a key role. All this processes involve fluid overpressures which need to be studied in detail and, although different, can provide useful information for future projects.

A particularly interesting field of development lies in the implementation of solid approaches which could simulate the potential for host rock damage accurately. The importance of forecasting potential dangers derived from underground injection projects makes it necessary to implement more complex theories in numerical simulators so as to provide consistent and realistic results. In this sense, the aforementioned "strong discontinuities approach" and use of interface elements to simulate rock damage and fracture propagation seems to have a lot of potential for future simulations of CCS projects. For instance, application of this approach to some of the cases that have been presented throughout this work and, in particular, to a real large-scale project such as the In Salah injection project can certainly provide interesting results about caprock sealing capacity.

With time, further field data and the possibility of implementing constitutive models capable of reproducing rock behaviour more accurately, deep underground storage projects are expected to become more understood and, thus, accepted by society.

BIBLIOGRAPHY

Works cited

[1] Alonso, E.E; Zandarín, M.T.; Olivella, S. Joints in unsaturated rocks: Thermo-hydro-mechanical and constitutive behaviour. *Journal of Rock and Geotechnical Engineering*, 2013, issue, p. 200-213.

[2] Ansolobehere, S. [et al.]. *The Future of Coal* [online]: *Options for a Carbon-Constrained World*. Cambridge, MA: MIT, 2007 [Consulted: 2013/09/21]. Available in: <http://mit.edu/coal/>

[3] Australian Government. Department of Environment. *Climate Change* [online]: *Greenhouse effect*. Canberra: Department of the Environment, 2013. Available in: <http://www.climatechange.gov.au/greenhouse-effect>

[4] Cappa, F. Modeling of coupled deformation and permeability evolution during fault reactivation induced by deep underground injection of CO2. *International Journal of Greenhouse Gas Control*, 2011, vol. 5, issue 2, p. 336-346.

[5] Hodrien, C. *Squaring the Circle of Coal* [online]: *Carbon Capture and Storage (CCS)*. Bath: Claverton Group, 2008. [Consulted: 2014/01/04]. Available in: <http://www.claverton-energy.com>

[6] Mathieson, A. [et al.]. In Salah CO2 Storage JIP: CO2 sequestration monitoring and verification technologies applied at Krechba, Algeria. *Energy Procedia*, 2011, vol. 4, p. 3596-3603.

[7] National Research Council. *Advancing the Science of Climate Change* [online]. Washington, DC: The National Academies Press, 2010. [Consulted: 2013/20/10]. Available in: < http://nas-sites.org/americasclimatechoices/>

[8] Olivella, S.; Alonso, E.E. Gas flow through clay barriers. *Géotechnique*, 2008, vol. 58, issue 3, p. 157-176.

[9] Oliver, J. On the discrete constitutive models induced by string discontinuity kinematics and continuum constitutive equations. *International Journal of Solid and Structures*, 2000, vol. 37, p. 7207-7229.

[10] Rinaldi, A.P; Rutqvist, J. Modeling of deep fracture zone opening and transient ground surface uplift at KB-502 CO2 injection well, In Salah, Algeria. *International Journal of Greenhouse Gas Control*, 2013, vol. 12, p. 155-167.

[11] Rinaldi, A.P; Rutqvist, J.; Cappa, F. Geomechanical effects on CO2 leakage through fault zones during large-scale underground injection. *International Journal of Greenhouse Gas Control*, 2014, vol. 20, p. 117-131.

[12] Rutqvist, J.; Birkholzer, J.T.; Tsang, C.-F. Coupled reservoir-geomechanical analysis of the potential for tensile and shear failure associated with CO2 injection in multilayered reservoir-caprock systems. *International Journal of Rock Mechanics and Mining Sciences*, 2007, vol. 45, issue 2, p. 132-143.

[13] Pam, V.T.H. CO2 storage – Simulations for forecasting the behavior of injection CO2 in geological formations. Dissertation for the degree of Philosophiae Doctor (ph.D.), Faculty of Mathematics and Natural Sciences University of Oslo, Department of Geosciences, 2012 [DUO, Digitale utgivelser ved UiO].

[14] Patil, R.H. Impacts of Carbon Dioxide Gas Leaks from Geological Storage Sites on Soil Ecology and Above-Ground Vegetation. A: Ali, M. *Diverstiy of Ecosystems*. Intech, 2012, p. 27-50.

[15] Sheriff, R. E., Geldart, L. P. *Exploration Seismology*. 2nd ed. Cambridge: Cambridge University Press, 1995. p. 351.

[16] Székely, E. *Supercritical Fluid Extraction* [online]. Budapest: Budapest University of Technology and Economics, 2007 [Consulted: 2013/12/05]. Available in: <http://sunny.vemt.bme.hu/sfe/angol/supercritical.html>

[17] The CO2 Capture Project (CCP). *Trapping mechanisms* [online]. CCP, 2008 [Consulted: 2013/10/28]. Available in: < http://www.co2captureproject.org/co2_trapping.html>

[18] The Paleontological Research Institution. *Stratigraphical Traps* [online]. Ithaca, NY: The Paleontological Research Institution [Consulted: 2013/11/10]. Available in: <http://www.priweb.org/ed/pgws/systems/traps/structural/structural.html>

[19] The Paleontological Research Institution. *Structural Traps* [online]. Ithaca, NY: The Paleontological Research Institution [Consulted: 2013/11/10]. Available in: <http://www.priweb.org/ed/pgws/systems/traps/structural/structural.html>

[20] United States Environmental Protection Agency (EPA). *Clean Energy* [online]*: Carbon Dioxide Capture and Sequestration*. Washington, D.C: EPA, 2012 [Consulted: 2013/11/04]. Available in: <http://www.epa.gov/climatechange/ccs/index.html>

[21] United States Environmental Protection Agency (EPA). *The EPA Greenhouse Gas Equivalencies Calculator* [online]. Washington, D.C: EPA, 2012 [Consulted: 2013/11/04]. Available in: < http://www.epa.gov/cleanenergy/energy-resources/calculator.html#results >

[22] University Corporation for Atmospheric Research (UCAR). *The Greenhouse Effect* [online]. Boulder, Colorado: NCAR & UCAR [Consulted: 2013/10/25]. Available in: <http://www.ucar.edu/learn/1_3_1.htm>

[23] UPC. Departament d'Enginyeria del Terreny, Cartogràfica i Geofísica. *CODE_BRIGHT user's guide v. 4* [online]. Barcelona: UPC, ETCG, 2013 [Consulted: 2013/07/20]. Available in: <https://www.etcg.upc.edu/recerca/webs/code_bright>

[24] UPC. Departament d'Enginyeria del Terreny, Cartogràfica i Geofísica. *Short course CODE_BRIGHT documentation* [online]. Barcelona: UPC, ETCG, 2013 [Consulted: 2013/08/05]. Available in: <https://www.etcg.upc.edu/recerca/webs/code_bright>

[25] Villarrasa, V. [et al.]. Effects of CO2 Compressibility on CO2 Storage in Deep Saline Aquifers. *Transport in Porous Media*, 2010, vol. 85, issue 2, p. 619-639.

[26] Vilarrasa, V.; Olivella, S.; Carrera, J. CO2 injection in deep saline sloping aquifers through a vertical well. To: Workshop of CODE-BRIGHT Users. "3rd Workshop of CODE-BRIGHT Users". Barcelona: 2011, p. 1-4.

[27] Yeo, S.-D.; Kiran, E. Formation of polymer particles with supercritical fluids: A review. *The Journal of Supercritical Fluids*, 2005, vol. 34, issue 3, p. 287-308.

Other references

Tsang, C.-F. A Comparative Review of Hydrologic Issues Involved in Geologic Storage of CO2 and Injection Disposal of Liquid Waste. *Environmental Geology*, 2008, vol. 54, issue 8, p. 1723-1737.

Zandarín, M.T.; Alonso, E.E; Olivella, S. A constitutive law for rock joints conisdering the effects of suction and roughness on strength parameters. *International Journal of Rock Mechanics and Mining Sciences* , 2012, vol. 60, p. 333-344.

Zhou, Q. [et al.]. A method for quick assessment of CO2 storage capacity in closed and semi-closed salineformations. *International Journal of Greenhouse Gas Control*, 2008, vol. 2, issue 4, p. 626-639.